TECHNISCHE UNIVERSITÄT MÜNCHEN

Fakultät für Elektrotechnik und Informationstechnik

Lehrstuhl für elektrische Antriebssysteme und Leistungselektronik

Modulation Strategies for Symmetrical Six-Phase Drives

Daniel Glose, M.Sc.

Vollständiger Abdruck der von der Fakultät für Elektrotechnik und Informationstechnik
der Technischen Universität München zur Erlangung des akademischen Grades eines

Doktor-Ingenieurs (Dr.-Ing.)

genehmigten Dissertation.

Vorsitzender:
Univ.-Prof. Dr.-Ing. Ulrich Wagner

Prüfer:
1. Univ-Prof. Dr.-Ing. Ralph Kennel
2. Prof. Dr.-Ing. Edson Bim, Universidade Estadual de Campinas, Brasilien

Die Dissertation wurde am 16.11.2015 bei der Technischen Universität München eingereicht und durch die Fakultät für Elektrotechnik und Informationstechnik am 09.01.2016 angenommen.

Vorwort

Die vorliegende Dissertation entstand im Rahmen meiner Tätigkeit am Lehrstuhl für elektrische Antriebssysteme und Leistungselektronik der technischen Universität München in den Jahren 2011 bis 2015. Dem Inhaber des Lehrstuhls, Prof. Dr.-Ing Ralph Kennel, möchte ich für seine fortwährende Unterstützung danken, sowie Herrn Prof. Dr.-Ing Edson Bim für seine außerordentliche Einsatzbereitschaft und seine Diskussionsfreude. Außerdem danke ich der Deutschen Forschungsgemeinschaft (DFG) für die finanzielle Förderung, ohne die die praktische Umsetzung des Vorhabens nicht möglich gewesen wäre.

Anerkennung gebührt auch meinen Kollegen, die mich während der Zeit tatkräftig unterstützt haben. Auch den von mir betreuten Studenten bin ich dankbar für die immer wieder wertvolle Zusammenarbeit.

München, April 2016 Daniel Glose

Kurzfassung

Für Anwendungen im Niederspannungsbereich bis zu 1000V haben sich dreiphasige Antriebssysteme mit einem Spannungsumrichter als Standard durchgesetzt. Dreisträngige Motoren und Umrichter mit zwei Spannungsebenen sind entsprechend kostengünstig von verschiedenen Herstellern bis zu einer Leistung von etwa 500kW erhältlich. Für Anforderungen oberhalb dieser Spannungs- oder Leistungsgrenze müssen Einzellösungen wie z.B. Mehrlevelumrichter entwickelt werden, deren Kosten überproportional höher liegen.

In der vorliegenden Arbeit wird ein Antriebskonzept untersucht, welches aus zwei in Serie oder parallel verschalteten Umrichtern und einer sechssträngigen elektrischen Maschine besteht. Das Konzept ist aus leicht modifizierten Standardkomponenten aufgebaut und verspricht somit höhere Spannungen/Leistungen bei gleichzeitig günstigen Anschaffungskosten. Die erweiterte Anzahl an Halbleitern bzw. Spannungszuständen lässt vermuten, dass bei geeigneter zeitlicher Schaltabfolge die Stromharmonischen in der Maschine reduziert werden können. Dieser Zusammenhang wird im Folgenden näher beleuchtet.

Die Umrichterausgänge des Antriebssystems können nur zwei diskrete Spannungswerte annehmen. Folglich müssen Zwischenwerte mithilfe eines Vergleichs- oder Rechenverfahrens moduliert werden. Die beiden gängisten Varianten, die Sinus-Dreieck Pulsbreitenmodulation (PWM) und die Raumzeigermodulation (RZM) werden für das sechsphasige System untersucht und Anwendungsstrategien zur Reduktion der Stromharmonischen abgeleitet.

Werden die sechs Phasen zu zwei dreiphasigen Systemen zusammengefasst und jeweils synchron angesteuert, ergibt sich im Vergleich zum dreiphasigen Fall ein zusätzlicher Freiheitsgrad: Der Versatz zwischen den Ansteuersignalen. Es wird gezeigt, dass dieser Versatz einen erheblichen Einfluss auf die Stromharmonischen und einhergehend auf die Verluste sowie Vibrationen der Maschine hat.

Ausgehend von einem vereinfachten Maschinenmodell, bestehend aus zwei Streuinduktivitäten und induzierten Gegenspannungen, wird der optimale Versatz für beide Modulationsverfahren mathematisch hergeleitet. Die Funk-

tionsergebnisse sind abhängig von der Amplitude des Referenzsignals bzw. -vektors, dem Verhältnis der beiden Streuinduktivitäten und zusätzlich, bei Anwendung der RZM, dem Winkel des Referenzvektors.

Im Vergleich zum dreiphasigen Fall erlauben sechsphasige Antriebe eine deutlich höhere Anzahl an unterschiedlichen Schaltsequenzen, also Abfolgen von Spannungsvektoren. In dieser Arbeit werden neben dem versetzten Verfahren kontinuierliche RZM-Sequenzen aufgezeigt und deren optimaler Einsatz in Abhängigkeit des Referenzvektors und Induktivitätsverhältnisses erläutert. Auf Basis einer Optimierung werden anschließend praktikable Strategien abgeleitet, deren Anwendung rechnerisch zu einer Reduktion der Stromharmonischen führt.

Die mathematischen Ergebnisse werden anhand von Simulationen bewertet und mit Experimenten validiert. Dazu stand ein Testaufbau mit einer sechssträngigen symmetrischen Asynchronmaschine und zwei Umrichtern zur Verfügung. Die praktischen Versuche bestätigen die theoretischen Ergebnisse: Insbesondere bei hohen Induktivitätsverhältnissen können die hergeleiteten Strategien die Harmonischen reduzieren und haben damit einen positiven Einfluss auf Effizienz und hörbare Vibrationen des Antriebssystems.

Abstract

For applications in the low voltage range up to 1000V, three-phase power systems with a voltage converter have gained acceptance as a standard topology. Three-phase motors and converters with two voltage levels up to 500kW are available at a reasonable cost from several different manufacturers. However, for requirements above this voltage or power limit, individual solutions such as multi-level inverters must be developed resulting in a disproportionate increase in the cost.

In this paper a drive concept is investigated, consisting of two series or parallel connected inverters and a six-phase electrical machine. Slightly modified standard components are used in construction of the drive, resulting in higher voltage and power while at the same time requiring a lower cost. The somewhat larger number of semiconductors and voltage states suggests that with a suitable time sequence the switching current harmonics in the machine can be reduced. This relationship is discussed in more detail below.

The converter outputs of the drive system can only accept two discrete voltage values. Consequently, intermediate values must be modulated using a comparative or calculation method. The two most common variants, the sine-triangle pulse width modulation (PWM) and the space vector modulation (SVM) are analyzed for the six-phase system and application strategies are derived to reduce the current harmonics.

If the six phases are considered to be two three-phase systems, each driven synchronously, then there is an additional degree of freedom which does not appear in the three-phase case: the offset between the driving signals. It is shown that this displacement has a significant impact on the current harmonics and also on the losses and vibrations of the machine. Based on a simplified machine model, consisting of two leakage inductances and induced reverse voltages, the optimum skew for both modulation schemes is then mathematically derived. The function results are dependent on the amplitude of the reference signal or vector, the ratio of the two leakage inductances, and in addition, when using the SVM, the angle of the reference vector.

In comparison to the three-phase case, six-phase drives actually allow a

significantly higher number of different switching pattern, i.e. sequences of voltage vectors. In this paper, continuous SVM sequences are shown next to the offset process and their optimal use is explained as a function of the reference vector and inductive ratios. Next, several practical strategies are derived using an optimization method. The application of these strategies leads to a reduction of the harmonic current.

The mathematical results are assessed on the basis of simulations and additionally are validated with experiments performed on a test drive. For this purpose a test bench was set up using a symmetrical six-phase induction motor and two inverters. The practical tests successfully confirm the theoretical results: especially at high inductance ratios the derived strategies are able to reduce the harmonics and therefore have a positive impact on efficiency and audible vibrations of the drive system.

Contents

Chapter 1

Introduction

The increasing demand for energy and the limited amount of resources in the world have led to a wide spread awareness of sustainability and efficiency in the last decades. Economists, politicians, and even private consumers are giving the aspect of sustainability more and more importance in their decision making processes to achieve “development that meets the needs of the present without compromising the ability of future generations to meet their own needs” [21].

For developing countries, economic growth, energy consumption and CO_2-emissions are generally positively linked [6]. In order to achieve a worldwide balanced gross domestic product (GDP) per person, further emissions are therefore expected from those nations.

For industrialized countries, however, the aforementioned relation might not be appropriate. Germany, for example, increased its GDP by about 50% compared to 1995, while its primary energy consumption (PEC) was reduced by nearly 10% in the same period. According to Figure 1.1 the carbon dioxide emissions decreased even further, such that they are clearly decoupled from the economic situation.

On the one hand this negative trend might be caused by energy intense industry moving abroad, such as steel or cement. On the other hand, economic technologies are developed and might be more often applied.

According to the increasing EEC rate in Figure 1.1, electricity has been found as a suitable energy source that meets the new requirements. Among common sources, electricity offers the highest grade of exergy, i.e. for a certain state of the art converter, the transformable energy amount can reach the highest values [33]. That is why in many power technology analysis, the maximum reachable work at the output is set in relation to its electricity equivalent [99]. At its highest conversion efficiency, generation and distribution of electricity is simple and dangerous emissions do not appear at the

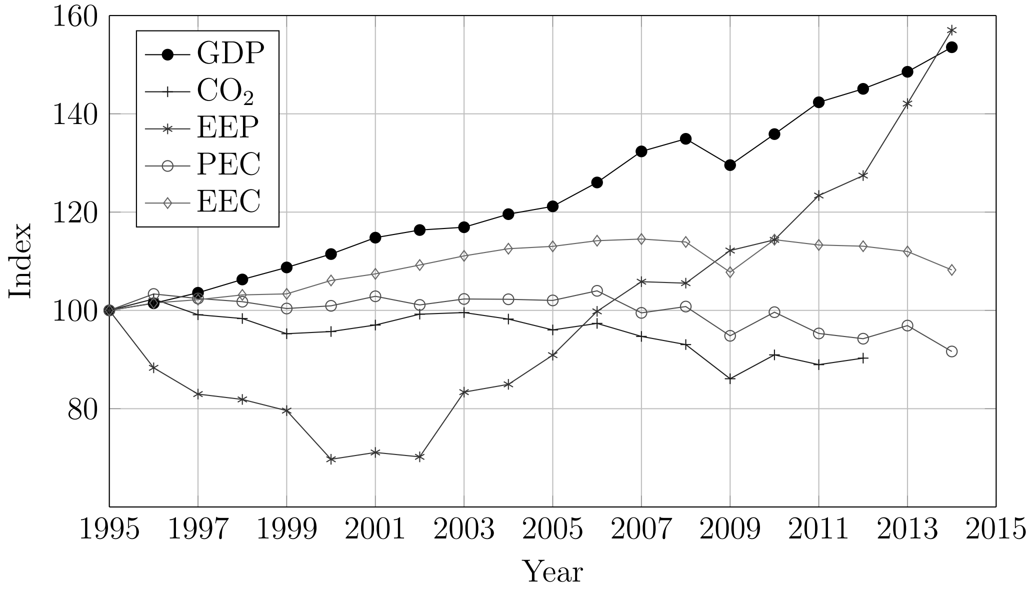

Figure 1.1: Development of Germany's gross domestic product (GDP), carbon dioxide emissions (CO_2), electric energy prices (EEP), primary energy consumption (PEC), and electric energy consumption (EEC) in the last two decades [108, 24].

consumption side.

Electric energy can be converted from renewable sources such as hydro, wind, solar or biomass. In that case, neither generation nor consumption contribute to the CO_2 emissions and the conversion string can be seen as *sustainable*. Although the main electric power plants in Germany are still fed with fossil fuels, the increasing number of renewable sources raised their contribution to the total electricity generation from 4.7% in 1995 to 27.8% in 2014 [5].

The increased cost of fuel and the subsidy for the installation of further sustainable power plant capacities raised the electric energy prices (EEP) noticeably through higher base rates and extra fees (see Figure 1.1). Compared to 2002, the EEP for industry and commerce in 2014 has more than doubled. Consumers consequently pay more attention to energy saving technologies. Despite the increased interest, only "a small fraction of the economical potential of energy efficiency is currently exploited" [9].

With 44% of the total electric energy use, the industry sector is the greatest consumer in Germany, followed by trade and commerce (27%), private households (27%), and transportation (2%) [1]. In industry, nearly 70% of the energy is converted with electric motors for pumping, ventilating, cooling, compression of air, or other applications (compare with Figure 1.2). Hence, the optimization of electric drive trains plays an important role to reduce harmful emissions on the generation side, while also reducing costs on the consumption side.

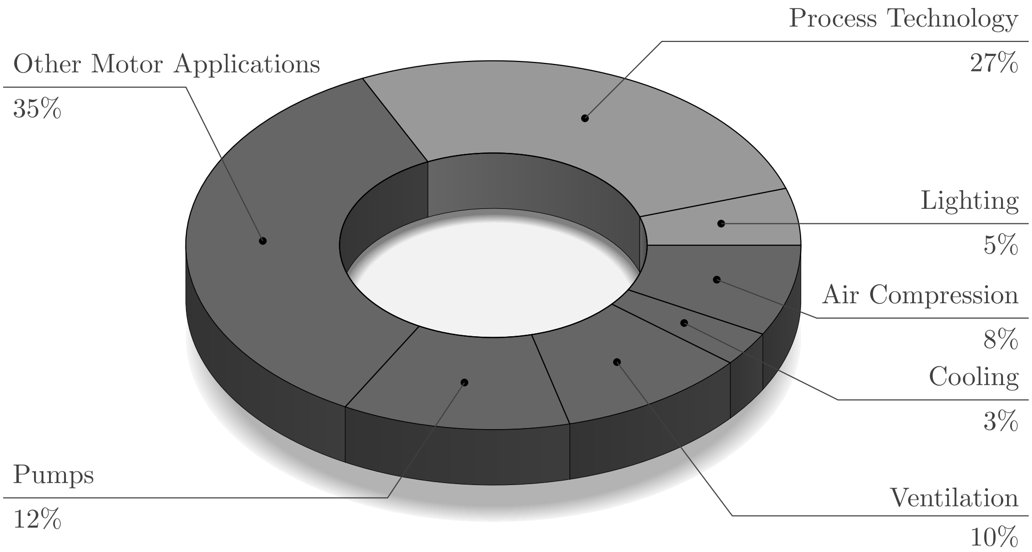

Figure 1.2: Electric energy consumption of German industry and its areas of application. Dark sectors: electric motor applications [37].

The greatest potential for energy saving (around 60%) lies in the mechanical optimization of the drive train according to its application. Pumps for example are in most cases oversized, i.e. their rated power is at least 20% higher than what is needed [23]. Further savings (around 30%) are achievable by replacing directly grid-connected motors with controlled drive systems. Those systems adapt the rotational speed or torque of the motor according to the demand. Only half of all motor applications in industry are controllable and an additional third do not take full advantage of the extra degrees of freedom [105].

The replacement of standard motors with high-efficiency alternatives might have a smaller impact on energy savings. This procedure represents only 10% of the whole feasible potential [96].

An important parameter for higher market penetration of efficient drives is the price, i.e the total cost of ownership (TCO). This factor is calculated over a certain period of time and includes asset cost as well as any other aspect of operation (energy, reparation, service, downtime, etc.). In many cases, the energy cost dominates the TCO with more than 90% [23]. Consequently, nearly 70% of the companies which consistently include the TCO procedure in their investment decisions are using high efficiency drives. Companies without TCO might be frightened by the higher asset costs compared to the standard equipment, which is reflected by the lower penetration rate of only 45% [105].

The asset costs of energy saving drives are mainly determined by the power converters, which are usually realized as voltage source inverters (VSIs). For low voltage applications up to 1kV these inverters are available off the shelf from many suppliers. Their prices vary proportional to their rated output power, as shown in Figure 1.3. This proportionality is demonstrated in the figure through a linear regression with an offset of 233 EUR and a slope of 66 EUR/kW.

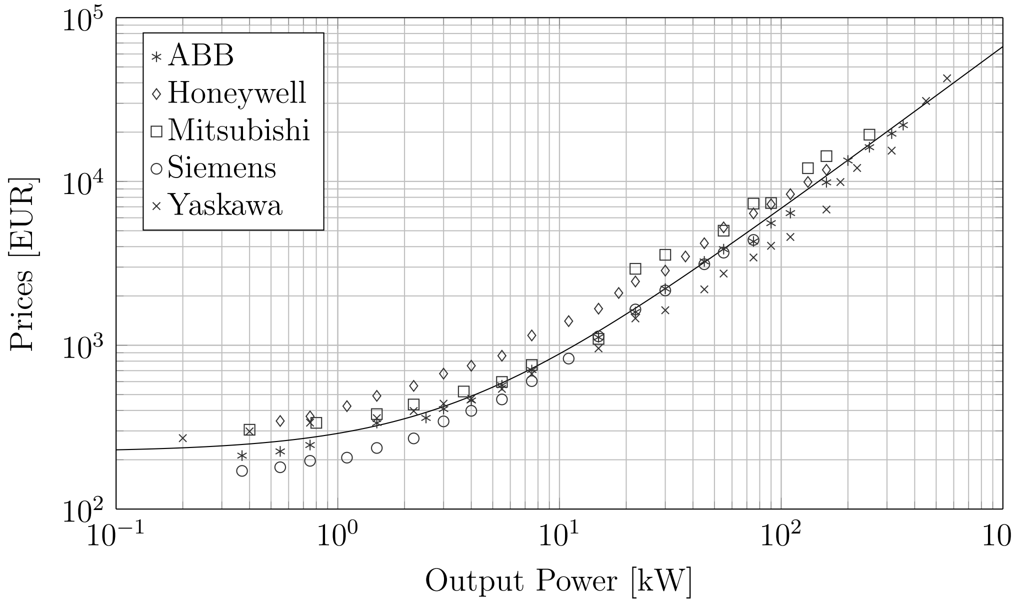

Figure 1.3: Low voltage inverter pricing over output power of several suppliers. Solid curve: approximated relationship through linear regression.

For power converters exceeding the aforementioned power or voltage rating, the linear relationship does not hold true. According to [119], most of the installed medium voltage drives are in the range of 1-4MW with a voltage rating between 3.3 and 6.6kV. In those voltage or power ranges, converters prices are within 100-200 EUR per kW, which is significantly higher compared to their low voltage counterpart.

The increased asset cost for high power converters might be the reason why 97% of those drive types are directly connected to the grid and operated at fixed speed [119]. The retrofit of such systems is thus a huge market and offers significant energy savings. In order to achieve a higher market penetration, the TCO of such drives and especially the asset costs should be decreased further.

Section 2 of this work presents high power topologies which are commonly used for such drives. In addition, several corresponding alternatives are under investigation, i.e. converters in conjunction with an appropriate machine. All system types are analyzed according to several important factors for operation, such as cost to power ratio, fault tolerance, current distortions, and power sharing capabilities. It is shown that multiple three-phase topologies have advantageous characteristics regarding system cost and post fault behavior. In the following, the operation of a drive with six phases is therefore further examined.

In Section 3, a general six-phase machine and inverter are modeled. Two forms of transformation are introduced, each one describes the machine and inverter behavior in two independent planes. Due to the higher number of phases, more degrees of freedom for control are available.

The two three-phase inverters are able to produce $2^6 = 64$ different switching states (compared to $2^3 = 8$ for common drives). The additional states can be exploited for reducing the phase current distortions, which are caused by discrete inverter switching behavior. Section 4 introduces two different analysis techniques to determine those distortions, i.e. the double Fourier integral and the harmonic flux analysis.

Controlling the inverter outputs by modulating the reference voltage waveform with a carrier signal offers the ability to shift the carrier signals in reference to each other. Section 5 shows that there exists an optimal shift value depending on the reference voltage amplitude and the machine parameters.

Another very common method for voltage generation is space vector modulation. Section 6 demonstrates how to apply this method to the six inverter legs. The very high quantity of different possible switching sequences makes the minimization of distortions time consuming and not feasible in real time. Several procedures are shown in this section which greatly reduce complexity but still offer high performance.

The aforementioned operation strategies were applied on a test system and the impact on the overall drive efficiency, torque ripple, and noise were observed. The results of these experiments are shown in Section 7. It could be measured that the optimal operation has a positive influence on the efficiency and significantly reduces the vibration of the machine casing. A summary in Section 8 concludes this work and gives an outlook for future research.

Chapter 2

High Power Topologies

For several high power applications the topologies needed are different from the common three-phase drives. Numerous suggestions can be found in literature capable of exceeding the voltage, current, speed, or torque specifications of common systems. The propositions have in common multiple numbers of switching elements or phases. These structures, in general, allow a certain level of redundancy which can increase reliability. The last argument is of importance for safety-critical applications and might reduce downtime of a system if a failure occur.

In any case, the number of inverter switching states is increased, which also leads to decreased or increased current distortions. Improvement might be achievable but it depends on proper modulation strategy as well as drive topology. The unwanted distortions are responsible for extra losses and, in several applications, they have to be minimized in order to comply with a certain level for electromagnetic compatibility or noise.

In the following section, the most discussed topologies are presented. On the basis of the common three-phase drive structure in Section 2.1, the multilevel and parallel inverter systems are introduced in Sections 2.2 and 2.3. The topologies of open end winding and multiphase drives are explained in Sections 2.4 and 2.5. The discussion in Section 2.6 compares and evaluates the mentioned topologies regarding redundancy, scalability for high power ratings, cost for development and production, and their ability to reduce distortions.

2.1 Common Three Phase Drives

The predominant inverter topology of low-voltage drives consists of three output legs (a, b, c). Each leg can be connected through a half bridge to either the upper $+U_d/2$ or the lower $-U_d/2$ voltage level. A half bridge consists of two switching elements (see Figure 2.1a), such that in total six switches determine the inverter's output voltage. Consequently, there are 2^3 different switching states.

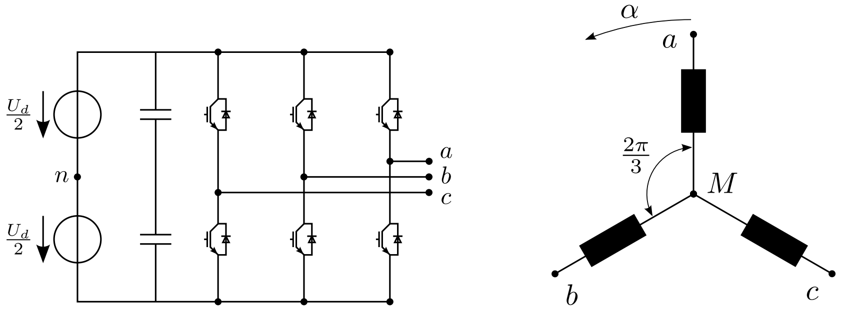

(a) Two level, three-leg inverter. (b) Stator phase structure of a common machine

Figure 2.1: Common AC drive consisting of a three-leg inverter and a three phase machine.

The three legs of the inverter are directly linked to the corresponding connection points on the machine's stator (see Figure 2.1b). Over one electric circumference α the three stator phases are evenly distributed, i.e. consecutive phases are separated by $\frac{2\pi}{3}$. Usually the phases are star- rather than delta-connected in order to avoid any harmonic current of $3k$ the fundamental frequency with $k \in \{1, 3, 5, \ldots\}$. The potential of the isolated star point M is floating, which reduces the complexity of the system, as demonstrated in Section 3.

The inverter and machine of the drive setup are standardized for low voltage applications up to $U_d = 1kV$ and $500kW$ which makes it available off the shelf for low cost (see Figure 1.3). Beyond these voltage or power ratings, different designs and technologies have to be used. On the inverter side, the layout and the electric components are to be adapted. Doing so, the switching elements might experience increased switching losses, which reduces the maximal switching frequency and increases current distortions. On the machine side, the wire insulation might be modified for higher voltages.

If one phase in the machine is not connected to the star point or both switches of one half bridge are open (open fault operation) the machine is still able to generate torque above a certain rotational speed [64]. The torque generation, however, is strongly pulsating and the machine's power rating decreases by at least 1/3 [11]. The minimum speed is dependent on the inertia of the rotor. Below this limit or at standstill, the machine can not be operated and the system fails. As shown in [116], the three-phase drive requires modifications to be fault tolerant, including the addition of auxiliary switches.

2.2 Multilevel Inverter Systems

For controlled AC drives in the megawatt and medium voltage range a family of multilevel inverters has been developed in the last decades [76, 98, 115]. They have in common the division of the DC-voltage into more than two levels and offer a three leg output to connect any common AC machine. Although any number of levels are imaginable, the topology with three output voltages, i.e. $+U_d/2$, 0, $-U_d/2$ (neutral point clamped) is the most promising type (3L-NPC). The structure combines the required medium voltage capability with acceptable complexity and the highest efficiency over all multilevel converters [73].

A simplified circuit diagram of a 3L-NPC is given in Figure 2.2. The four transistors of each half bridge are capable of switching either the upper or lower DC-Bus voltage to the output by simultaneously switching the upper or lower two semiconductors. The capacitive voltage divider adds the zero level to the output voltage waveform if the mid semiconductors are switched on while the outer ones are switched off.

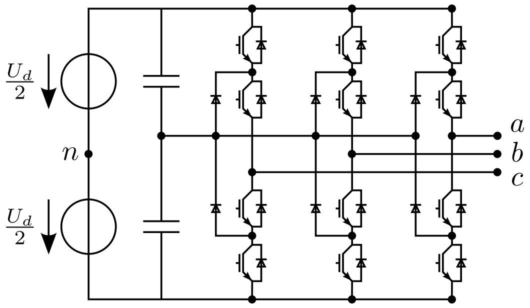

Figure 2.2: Circuit diagram of a three-level neutral point clamped inverter.

Due to the increased number of output levels, the current distortions can be reduced significantly if a proper modulation strategy is applied [20, 49, 114]. The topology offers a simple power circuit, low component count and a straight forward protection [3]. Several manufacturers, such as ABB, Siemens, Alstom, and GE are making the 3L-NPC commercially available. The topology becomes a competitive alternative for a large variety of high power applications.

Anyhow, the 3L-NPC is a standalone product and cannot be assembled modularly from the common two level setup of Section 2.1. This argument makes the power to cost ratio somewhat higher than for the two-level topology. Regarding reliability, the inverter has a higher number of power semiconductors connected in series, and consequently the possibility of a failure is much higher than for the two-level case [80].

In [82] a strategy for coping with a short circuit failure of a switching device is proposed which does not call for changes in hardware. The fault tolerant strategy is achieved due to redundant voltage vectors. Under faulty condition, however, the switches have to withstand the total DC-Bus voltage. An open circuit fault can only be managed with extra equipment, such as pairs of thyristors [81, 94], leading to increased system cost.

2.3 Parallel Inverter Systems

The outputs of standard three-leg and two level inverters can be paralleled as shown in Figure 2.3. In order to share current among multiple inverters and prevent short circuits, a coupling inductance magnetically links several outputs. The coupled phases a, b, c are directly connected to a common three phase machine. With a proper designed inductance coil [100], the outputs of the converter exhibit voltage waveforms similar to multilevel inverters and thus, the machine's current distortion factor is relatively low.

With such a drive setup, high power ratings of up to 2000kW and high dynamic performance is achieved in [106, 109, 111]. As shown in [16, 36], sequentially switching of the IGBT devices might lead to zero current at the switching instant (soft switching) and consequently reduced power losses. Latter advantage makes the setup the preferable choice for high dynamic hardware in the loop test rigs [15]. The advantage, however, is achieved through an over-sized inverter and increased cost.

The necessary coils add volume, weight, and cost and make the drive system less attractive for certain applications, such as propulsion. In addition, the coils change the system characteristic in a negative manner, i.e. through an extra resistance and inductance. A series connection of several inverters (cascaded structure) is possible through isolated DC sources [86]. Such a topology demands additional transformers if only one AC source is available, which increases the aforementioned disadvantages.

The setup of Figure 2.3 enables the current flow from a half bridge to the machine, but also from one half bridge to another [87]. Such unwanted circulating common mode currents have to be reduced or eliminated, which adds complexity to the controller [27, 31]. Due to the parallel structure of the inverters, the setup is tolerant of an open fault of a single switching device [43].

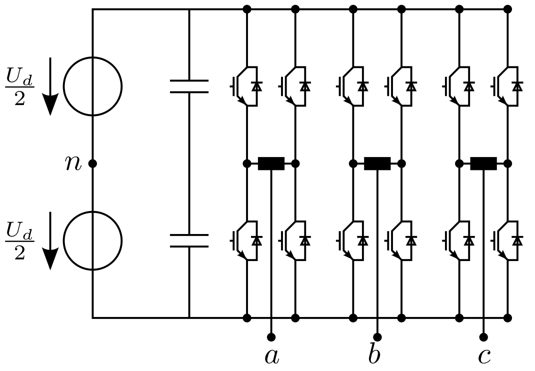

Figure 2.3: Circuit diagram of a parallel inverter system.

2.4 Open End Winding Drives

The three phases of a common machine are on one side either star or delta connected and on the other side linked to the inverter. As shown in Figure 2.4, the open end winding structure exhibits two common inverters each connected to one side of the phases [65].

The setup doubles the amplitude of a voltage waveform compared to the three phase counterpart. In order to avoid exciting any third order harmonic currents, the maximal value is limited to $\frac{3}{\sqrt{3}} = 1.73$ times the common waveform amplitude [101]. In order to achieve the same behavior, the windings of a three-phase machine might have to be adjusted to the aforementioned ratio. Both the lower inverter utilization and the machine redesign lead to slightly increased cost, compared to the common case.

The number of applicable switching states is increased, which offers a significant reduction in current distortion, as shown in [74, 121]. But comparing the inverter power dissipation, the arrangement suffers from higher conduction and switching losses of around 15% [85]. The parallel arrangement of switching devices, however, leads to an open fault tolerant converter.

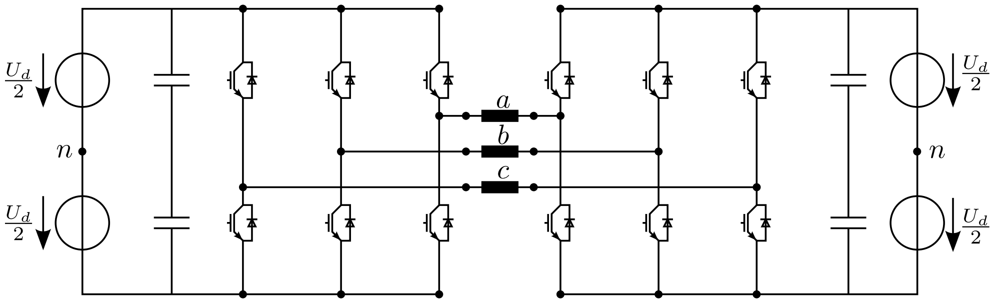

Figure 2.4: Circuit diagram of an open end winding drive system.

These characteristics make the drive setup an interesting alternative for propulsion purposes such as electric vehicles, where voltage division among inverters is not an important issue. Since common-mode or zero currents are able to flow between the two inverters, the controller has to deal with this issue, which might lead to even less DC-bus voltage utilization and greater complexity.

2.5 Multiphase Drives

Multiphase drives are topologies exhibiting more than three machine phases and corresponding inverter legs [61, 78, 95]. Such systems have experienced a significant growth since the end of the last century. With the additional phases, more degrees of freedom for control and machine design appear. In addition, the inverter and machine parts are redundant making the drive setup fault tolerant [79].

Nearly any number of phases for multiphase machines is conceivable, but only odd phase numbers (5, 7, 11, 13, ...) and multiples of three (6, 9, ...) are advantageous regarding the control or intrinsic elimination of spacial harmonics [68, 69]. Particularly the six-phase machine has gained a lot of attention, since it can be combined modularly from standard equipment and therefore at low cost. In that case, two standard inverters of Figure 2.1a are either connected in parallel at the same DC-link to share current or they are connected in series to divide the DC-voltage [78].

There are different winding arrangements feasible for six-phase machines, which mainly differ in the displacement angle between the two three phase sets (see Figure 2.5). The symmetrical machine types of Figure 2.5a and 2.5b exhibit six different magnetic axes, identical to the common three phase counterpart. The symmetric structure is achieved with a displacement angle of $\gamma = n\frac{\pi}{3}$, where $n \in \mathbb{N}$. The asymmetric type of Figure 2.5c exhibits any other value of displacement which results in 12 different magnetic axes.

For the case $\gamma = \frac{\pi}{6}$ the axes are evenly distributed around the circumference. Originally applied to current source inverters or voltage source inverters operated in six-step mode, this specific machine type significantly reduces machine vibration, noise, and heating of the rotor [92, 39]. Although the stator phase currents show fifth and seventh order time harmonics, these components do not contribute to the air gap flux and therefore sixth order torque harmonics are eliminated.

As mentioned in [44] such a drive setup offers 48 different voltage vectors and increases the largest circular trajectory to $U_d \cos(\pi/12)$ which is more than the three-phase counterpart is able to produce ($U_d \cos(\pi/6)$). This advantage, however, is achieved with higher phase current harmonics, which do not contribute to the dq-frame [83] but appear in an additional predefined subspace. Such space vector decomposition was first developed in [120] and is the basis for modern modulation and control techniques for the asymmetric machine type [7, 14, 88].

In [47, 48] it could be shown that the ratio of stray inductance counting for both subspaces has a significant influence on the performance of the modulation strategy. Since the inductance value for the additional subspace is relatively low, the phase current distortions are higher compared to the common three-phase drive.

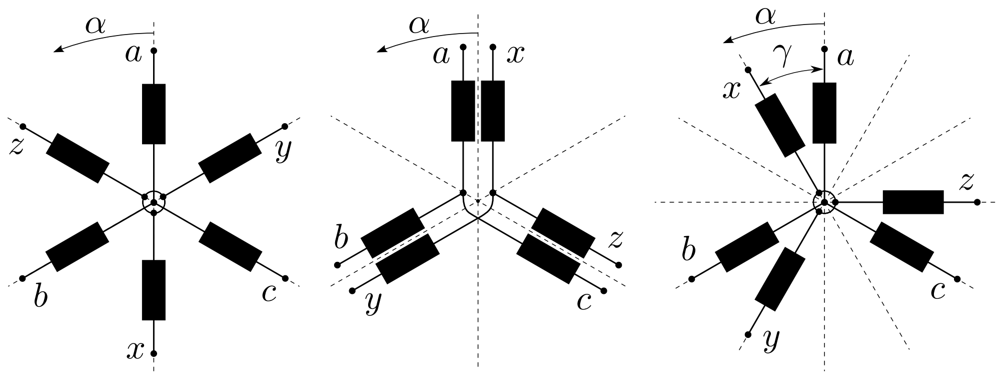

(a) Symmetrical six-phase machine with a displacement of $\gamma = \pi$.

(b) Symmetrical six-phase machine with no displacement.

(c) Asymmetrical six-phase machine with an arbitrary displacement ($0 < \gamma < \pi/3$).

Figure 2.5: Possible phase arrangements of the machine and classification based on the angle between the two three-phase sets.

Symmetrical six phase machines with a displacement of $\gamma = 0$ were first directly connected to the grid [4] in order to achieve a better post fault characteristic. In the late 80's, this machine type was proposed to increase power capabilities of a drive setup with two inverters [63, 62]. Since the machine behavior of both three-phase sets is equal, both inverters are able to operate independently. Although an increased number of voltage vectors can be defined for the dq-subspace, modulation schemes different from those which are known from common drives are not applicable since the strong magnetic coupling between the sets would cause high phase currents if different voltages were applied on two parallel phases.

With an angle of $\gamma = \pi/6$, the symmetric machine design provides the lowest magnetic coupling between the two sets and consequently offers more possibilities for modulation. In the following sections it is shown that a significant reduction in phase current distortion is achievable, resulting in a distortion factor which lies between the common drive of Section 2.1 and a three-level setup of Section 2.2.

An additional advantage for the symmetric machine type is elaborated in [26, 90]. With a proper winding layout and $\gamma = \pi/6$, the number of magnetic poles can be changed during operation. This characteristic was exploited for efficiency improvement in electric cars.

2.6 Comparison

Each of the aforementioned high power topologies offers advantages and disadvantages and consequently, a proper configuration for a specific application has to be chosen wisely. Table 2.1 gives a short overview of the different setups and characterizes them for comparison.

	CPR		OFT		THD	PSC		ZCC
	IN	MA	IN	MA		I	U	
Multilevel	> 1	1	X	X	< 1	X	√	X
Parallel Inverter	> 1	1	√	X	< 1	√	X	√
Open End Winding	> 1	1	√	X	< 1	√	X	√
Multiphase asym.	1	> 1	√	√	> 1	√	√	X
Multiphase sym.	1	1	√	√	≤ 1	√	√	X

Table 2.1: Comparison of high power topologies by the cost to power ratio (CPR) of inverter (IN) and machine (MA), the open fault tolerance (OFT), the total harmonic distortions (THD), the power sharing capability (PSC) in current (I) or voltage (U), and the necessary of zero current control (ZCC).

The cost to power ratio (CPR) assumes a proportionality between the rated system power and its price. Taking the common three-phase drive as the reference with a CPR value of one at a certain power level, an exchange with a multilevel inverter would have an increased CPR value for the inverter. The inverter CPR of the parallel inverter drive suffers from the necessary coupling transformer and the open end winding inverter needs to be rated above the output power specifications.

Since the multilevel, parallel inverter, and open end winding drives incorporate the same common three phase machine, their machine CPR is equal to one. Consequently, their fault tolerance towards an open machine phase (OFT) is none but, except the multilevel structure, they can handle an open switch fault of the inverter. The phase current distortions (THD) of the three systems can be significantly reduced compared to the common drive setup.

The power sharing capability (PSC) can be achieved either with a voltage (U) or current (I) division among several inverter switches. The multilevel divides the voltage along the devices, whereas with the parallel inverter and the open end winding structure only current sharing is applicable. For the latter two systems, a zero current control (ZCC) might be necessary in order to avoid unwanted circulating currents.

Multiphase drives are the only topologies that provide inverter and machine OFT as well as PSC through current or voltage division. In addition, zero currents do not have to be controlled as long as the machine neutral points are not connected. Their unity inverter CPR reflects the ability to implement common inverters without any hardware modifications.

For the asymmetrical machine design the winding structure has to be rearranged, which slightly increases its CPR. This machine type will also introduce higher current harmonics than the common machine.

The symmetrical multiphase machine design is thus a competitive alternative for high power drives. It combines good fault tolerance with voltage and current sharing capabilities at reasonable cost. On the basis of a six-phase drive it is shown in the following sections that a significant improvement in THD is also achievable.

Chapter 3

Modelling of the Six-Phase Drive

The electromagnetic characteristics of the six-phase drive will be examined in detail in this chapter. Section 3.1 describes how the six phases may be decomposed into two subspaces, and the resultant simplified machine equations are used in Section 3.2 to investigate machine behavior at high and low frequencies. In Section 3.3 the 64 possible voltage vectors will be decomposed into two subspaces using the previously mentioned methods. Finally, Section 3.4 is a brief description of the experimental equipment used to test the model.

3.1 Decomposition and Transformation

Any set of machine states can be represented in new component states with equal number, by means of a linear transformation. For a system with the six phases a,b,c,x,y, and z this relationship is expressed in a general form as:

$$\begin{bmatrix} X_a \\ X_b \\ X_c \\ X_x \\ X_y \\ X_z \end{bmatrix} = \underbrace{\begin{bmatrix} C_{11} & C_{12} & C_{13} & C_{14} & C_{15} & C_{16} \\ C_{21} & C_{22} & C_{23} & C_{24} & C_{25} & C_{26} \\ C_{31} & C_{32} & C_{33} & C_{34} & C_{35} & C_{36} \\ C_{41} & C_{42} & C_{43} & C_{44} & C_{45} & C_{46} \\ C_{51} & C_{52} & C_{53} & C_{54} & C_{55} & C_{56} \\ C_{61} & C_{62} & C_{63} & C_{64} & C_{65} & C_{66} \end{bmatrix}}_{\mathbf{C}} \begin{bmatrix} X_1 \\ X_2 \\ X_3 \\ X_4 \\ X_5 \\ X_6 \end{bmatrix} \tag{3.1}$$

where $X_1 \dots X_6$ are the new and decomposed component states.

The elements $(C_{11} \cdots C_{66})$ of the general transformation matrix $\mathbf{C}$ can be chosen arbitrarily, considering non-singularity [89]. Usually, those entries are chosen in such a way that they give a meaningful insight into the physical processes of the system. This is achieved with a decomposition of the states in orthogonal spaces and a simplification of the corresponding model.

In the following subsections, the Clarke transformation (commonly used for three-phase drives) will be modified for six phases, which reduces the number of dimensions from six to four. Next, a decomposition matrix $\mathbf{T_{pp}}$ is found, mapping the states onto two new planes such that the odd and even order harmonics are separated into the first and second subspace respectively.

3.1.1 Double Clarke-Transformation

For balanced power systems such as three-phase drives, where two phases are symmetrical with respect to the third, Clarke [28] shows how the system states may be projected onto a stationary $\alpha, \beta, 0$ reference frame. The so called Clarke transformation is widely applied and its matrix is defined as:

$$\mathbf{T'_C} = \frac{2}{3}\begin{bmatrix} \cos(0) & \cos(\frac{2\pi}{3}) & \cos(\frac{4\pi}{3}) \\ \sin(0) & \sin(\frac{2\pi}{3}) & \sin(\frac{4\pi}{3}) \\ \frac{1}{2} & \frac{1}{2} & \frac{1}{2} \end{bmatrix} = \frac{2}{3}\begin{bmatrix} 1 & -\frac{1}{2} & -\frac{1}{2} \\ 0 & \frac{\sqrt{3}}{2} & -\frac{\sqrt{3}}{2} \\ \frac{1}{2} & \frac{1}{2} & \frac{1}{2} \end{bmatrix} \tag{3.2}$$

The factor $\frac{2}{3}$ guarantees that the original and transformed components (e.g. voltage or current) have equal amplitudes.

The upper two rows of $\mathbf{T'_C}$ span out the orthogonal α, β-space and its entries are derived from the spatial distribution of the machine phases around the circumference. The third row of $\mathbf{T'_C}$ defines the zero-dimension, which can be neglected if the three-phase set is star-connected. Such a simplified setup offers two degrees of freedom, expressed in orthogonal α, β components. The corresponding transformation matrix is:

$$\mathbf{T_C} = \frac{2}{3}\begin{bmatrix} 1 & -\frac{1}{2} & -\frac{1}{2} \\ 0 & \frac{\sqrt{3}}{2} & -\frac{\sqrt{3}}{2} \end{bmatrix} \tag{3.3}$$

There are a number of alternative decomposition methods proposed by Kimbark [67], Concordia [29] and Hsiao [59, 60]. However, these transformations will not be investigated further in this work

Recall that a six-phase drive may be approached as two sets of three phases. Phases a,b,c belong to Set I and x,y,z to Set II. Therefore the Clarke transformation may be applied twice, resulting in a space defined by $(\alpha_I, \alpha_{II}, \beta_I, \beta_{II})$. The relationship to $\mathbf{T_{C2}}$ is thus:

$$\begin{bmatrix} X_{\alpha_I} \\ X_{\beta_I} \\ X_{\alpha_{II}} \\ X_{\beta_{II}} \end{bmatrix} = \underbrace{\begin{bmatrix} \mathbf{T_C} & \mathbf{0} \\ \mathbf{0} & \mathbf{T_C} \end{bmatrix}}_{=\mathbf{T_{C2}}} \begin{bmatrix} X_a \\ X_b \\ X_c \\ X_x \\ X_y \\ X_z \end{bmatrix} \quad \text{or} \quad \begin{bmatrix} X_a \\ X_b \\ X_c \\ X_x \\ X_y \\ X_z \end{bmatrix} = \mathbf{T_{C2}^{-1}} \begin{bmatrix} X_{\alpha_I} \\ X_{\beta_I} \\ X_{\alpha_{II}} \\ X_{\beta_{II}} \end{bmatrix} \tag{3.4}$$

where $\mathbf{T_{C2}^{-1}}$ is the pseudo inverse of $\mathbf{T_{C2}}$.

In both three phase sets, the zero-axis component is equal to zero as previously explained. Therefore the double Clarke matrix transforms the six dimensional system into a four dimensional one as seen in equation (3.4). This method has the benefit of reducing system complexity and is the basis of the interleaved switching approach as explained in Chapters 5 and 6. However, the states I and II are not decoupled. Decomposition is necessary to achieve decoupling, which provides further insight into the system as well as physical meaning.

3.1.2 Space Decomposition

In order to produce a decoupled state representation an additional transformation matrix $\mathbf{T_{pp}}$ must be found such that:

$$\begin{bmatrix} X_{\alpha_1} \\ X_{\beta_1} \\ X_{\alpha_2} \\ X_{\beta_2} \end{bmatrix} = \mathbf{T_{pp}} \begin{bmatrix} X_a \\ X_b \\ X_c \\ X_x \\ X_y \\ X_z \end{bmatrix} \quad \text{or} \quad \begin{bmatrix} X_a \\ X_b \\ X_c \\ X_x \\ X_y \\ X_z \end{bmatrix} = \mathbf{T_{pp}^{-1}} \begin{bmatrix} X_{\alpha_1} \\ X_{\beta_1} \\ X_{\alpha_2} \\ X_{\beta_2} \end{bmatrix} \tag{3.5}$$

Where subspace 1 is defined by the (α_1, β_1) plane and subspace 2 by the (α_2, β_2) plane. Additionally, using the definition of the double Clarke matrix from equation (3.4) the decomposed subspaces can also be represented as follows:

$$\begin{bmatrix} X_{\alpha_1} \\ X_{\beta_1} \\ X_{\alpha_2} \\ X_{\beta_2} \end{bmatrix} = \mathbf{T_{pp}} \cdot \mathbf{T_{C2}^{-1}} \begin{bmatrix} X_{\alpha_I} \\ X_{\beta_I} \\ X_{\alpha_{II}} \\ X_{\beta_{II}} \end{bmatrix} \tag{3.6}$$

Subspaces 1 and 2 achieve the desired decoupling of even and odd order harmonics, as will be shown later in this section.

But first, $\mathbf{T_{pp}}$ must be deduced from a general state representation. The machine's behavior can generally be described as an interaction between the magnetic fields produced by rotor and stator phase currents. This characteristic is expressed in a phase-to-phase influence matrix $\mathbf{S_p}$, where the dependencies are decomposed into stator fixed α and β components. For the symmetrical six-phase drive of Figure 2.5a, this 6×6 matrix is:

$$\mathbf{S_p} = \begin{bmatrix} \cos(\alpha_a) & \cos(\alpha_z) & \cos(\alpha_b) & \cos(\alpha_x) & \cos(\alpha_c) & \cos(\alpha_y) \\ \cos(\alpha_y) & \cos(\alpha_a) & \cos(\alpha_z) & \cos(\alpha_b) & \cos(\alpha_x) & \cos(\alpha_c) \\ \vdots & & & & & \vdots \\ \cos(\alpha_z) & \cos(\alpha_b) & \cos(\alpha_x) & \cos(\alpha_c) & \cos(\alpha_y) & \cos(\alpha_a) \end{bmatrix} \tag{3.7}$$

Where $\mathbf{S_p}$ is arranged by the geometric phase sequence around the air gap, and its entries are defined by the angles of the six phases $\alpha_g = [\alpha_a \; \alpha_b \; \alpha_c \; \alpha_x \; \alpha_y \; \alpha_z] = [0, \; 2\pi/3, \; 4\pi/3, \; \pi, \; 5\pi/3, \; \pi/3]$.

Due to the symmetric phase geometry, the $\mathbf{S_p}$ matrix is both symmetric and *circulant* [117], meaning every row is the same as the row above shifted to the right by one element. Circulant matrices have favorable properties for diagonalization: every circulant matrix of size $n \times n$ has the same eigenvectors independent of the actual elements in the matrix [34].

For every real, symmetric, circulant matrix of size 6×6, the real eigenvectors are the columns of the following matrix $\mathbf{S_6} \in R^{6\times 6}$ [45]

$$\mathbf{S_6} = \begin{bmatrix} \cos(0) & \cos(2\pi\frac{0\cdot 1}{6}) & \sin(2\pi\frac{0\cdot 1}{6}) & \cos(2\pi\frac{0\cdot 2}{6}) & \sin(2\pi\frac{0\cdot 2}{6}) & \cos(2\pi\frac{0\cdot 3}{6}) \\ \cos(0) & \cos(2\pi\frac{1\cdot 1}{6}) & \sin(2\pi\frac{1\cdot 1}{6}) & \cos(2\pi\frac{1\cdot 2}{6}) & \sin(2\pi\frac{1\cdot 2}{6}) & \cos(2\pi\frac{1\cdot 3}{6}) \\ \vdots & & & & & \vdots \\ \cos(0) & \cos(2\pi\frac{5\cdot 1}{6}) & \sin(2\pi\frac{5\cdot 1}{6}) & \cos(2\pi\frac{5\cdot 2}{6}) & \sin(2\pi\frac{5\cdot 2}{6}) & \cos(2\pi\frac{5\cdot 3}{6}) \end{bmatrix} \tag{3.8}$$

Thus a full set of $n = 6$ linear independent eigenvectors are achieved. Now that the eigenvectors are known, the diagonalization of $\mathbf{S_p}$ can be easily calculated with the relationship [110]

$$\mathbf{D_6} = diag\,(d_1, \cdots, d_6) = \mathbf{S_6}^{-1} \cdot \mathbf{S_p} \cdot \mathbf{S_6}$$

This type of decomposition is known in the literature as "Generalized Two-Phase Real Component Transformation" [117]. In [120] a modification of this transformation technique for asymmetrical six-phase drives is given as "Vector Space Decomposition".

A few modifications of $\mathbf{S_6}$ are necessary to finally achieve the single decomposition matrix $\mathbf{T_{pp}}$ [77]:

- Zero order content of $\mathbf{S_6}$ is left out since corresponding currents can not flow in the double-star configuration.
- The rows of $\mathbf{S_6}$ are rearranged so that the phase order a,b,c,x,y,z is achieved.
- $\mathbf{S_6}$ is scaled with $\frac{2}{6} = \frac{1}{3}$ to be current invariant.

Applying these conditions results in

$$\begin{aligned}
\mathbf{T_{pp}} &= \frac{1}{3}\begin{bmatrix}
\cos(2\pi\frac{0\cdot1}{6}) & \sin(2\pi\frac{0\cdot1}{6}) & \cos(2\pi\frac{0\cdot2}{6}) & \sin(2\pi\frac{0\cdot2}{6}) \\
\cos(2\pi\frac{2\cdot1}{6}) & \sin(2\pi\frac{2\cdot1}{6}) & \cos(2\pi\frac{2\cdot2}{6}) & \sin(2\pi\frac{2\cdot2}{6}) \\
\cos(2\pi\frac{4\cdot1}{6}) & \sin(2\pi\frac{4\cdot1}{6}) & \cos(2\pi\frac{4\cdot2}{6}) & \sin(2\pi\frac{4\cdot2}{6}) \\
\cos(2\pi\frac{3\cdot1}{6}) & \sin(2\pi\frac{3\cdot1}{6}) & \cos(2\pi\frac{3\cdot2}{6}) & \sin(2\pi\frac{3\cdot2}{6}) \\
\cos(2\pi\frac{5\cdot1}{6}) & \sin(2\pi\frac{5\cdot1}{6}) & \cos(2\pi\frac{5\cdot2}{6}) & \sin(2\pi\frac{5\cdot2}{6}) \\
\cos(2\pi\frac{1\cdot1}{6}) & \sin(2\pi\frac{1\cdot1}{6}) & \cos(2\pi\frac{1\cdot2}{6}) & \sin(2\pi\frac{1\cdot2}{6})
\end{bmatrix}^T \\
&= \frac{1}{3}\begin{bmatrix}
1 & -\frac{1}{2} & -\frac{1}{2} & -1 & \frac{1}{2} & \frac{1}{2} \\
0 & \frac{\sqrt{3}}{2} & -\frac{\sqrt{3}}{2} & 0 & -\frac{\sqrt{3}}{2} & \frac{\sqrt{3}}{2} \\
1 & -\frac{1}{2} & -\frac{1}{2} & 1 & -\frac{1}{2} & -\frac{1}{2} \\
0 & -\frac{\sqrt{3}}{2} & \frac{\sqrt{3}}{2} & 0 & -\frac{\sqrt{3}}{2} & \frac{\sqrt{3}}{2}
\end{bmatrix} \qquad (3.9)
\end{aligned}$$

In addition, the pseudo-inverted decomposition matrix $\mathbf{T_{pp}^{-1}}$ is calculated from $\mathbf{T_{pp}}$ as:

$$\mathbf{T_{pp}^{-1}} = \frac{1}{2}\begin{bmatrix}
2 & 0 & 2 & 0 & 1 & 1 \\
-1 & \sqrt{3} & -1 & -\sqrt{3} & 1 & 1 \\
-1 & -\sqrt{3} & -1 & \sqrt{3} & 1 & 1 \\
-2 & 0 & 2 & 0 & 1 & -1
\end{bmatrix} \qquad (3.10)$$

The following example can illustrate the physical meaning of the subspaces. Using current as the state variable, let the phases of Figure 2.5a conduct $I_a(t), \ldots, I_z(t)$, represented as two sinusoidal waveforms of first and second order, i.e.:

$$\begin{aligned}
I_a(t) &= \hat{I}_1\cos(\omega_1 t + \varphi_1 + \alpha_a) + \hat{I}_2\cos(\omega_2 t + \varphi_2 + 2\alpha_a) \\
I_b(t) &= \hat{I}_1\cos(\omega_1 t + \varphi_1 + \alpha_b) + \hat{I}_2\cos(\omega_2 t + \varphi_2 + 2\alpha_b) \\
&\ \vdots \\
I_z(t) &= \underbrace{\hat{I}_1\cos(\omega_1 t + \varphi_1 + \alpha_z)}_{\text{First order}} + \underbrace{\hat{I}_2\cos(\omega_2 t + \varphi_2 + 2\alpha_z)}_{\text{Second order}},
\end{aligned}$$

With amplitudes $\hat{I}_1, \hat{I}_2$, angular frequencies $\omega_2 = 2\omega_1$ and phase offset angles φ_1, φ_2.

Multiplying the phase currents by $\mathbf{T}_{pp}$ results in:

$$\begin{bmatrix} I_{\alpha_1} \\ I_{\beta_1} \\ I_{\alpha_2} \\ I_{\beta_2} \end{bmatrix} = \mathbf{T_{pp}} \begin{bmatrix} I_a(t) \\ I_b(t) \\ \vdots \\ I_z(t) \end{bmatrix} = \begin{bmatrix} \hat{I}_1 \cos(\omega_1 t + \varphi_1) \\ \hat{I}_1 \sin(\omega_1 t + \varphi_1) \\ \hat{I}_2 \cos(\omega_2 t + \varphi_2) \\ \hat{I}_2 \sin(\omega_2 t + \varphi_2) \end{bmatrix} \tag{3.11}$$

As seen in equation (3.11) the first order current is projected onto the $\alpha_1\beta_1$-plane, whereas the second order harmonic lies in the $\alpha_2\beta_2$-subspace. In general it can be shown that any machine state with an odd harmonic number is mapped onto the first plane, whereas the even order harmonic content is mapped onto the second plane.

Now that the elements of $\mathbf{T_{pp}}$ are known, further meaning of the decomposed subspaces can be achieved by substituting the values of $\mathbf{T_{pp}}$ and $\mathbf{T_{C2}^{-1}}$ into equation (3.6):

$$\begin{bmatrix} X_{\alpha_1} \\ X_{\beta_1} \\ X_{\alpha_2} \\ X_{\beta_2} \end{bmatrix} = \underbrace{\frac{1}{2} \begin{bmatrix} 1 & 0 & -1 & 0 \\ 0 & 1 & 0 & -1 \\ 1 & 0 & 1 & 0 \\ 0 & -1 & 0 & -1 \end{bmatrix}}_{=\mathbf{T_{pp}} \cdot \mathbf{T_{C2}^{-1}}} \begin{bmatrix} X_{\alpha_I} \\ X_{\beta_I} \\ X_{\alpha_{II}} \\ X_{\beta_{II}} \end{bmatrix} \tag{3.12}$$

From equation (3.12) it can be seen that the components of subspace 1 are achieved by a subtraction of the components of sets I and II. In contrast, the components of subspace 2 are a sum or negative sum of sets I and II. Therefore, if the excitation in I and II is equal, i.e. $X_{\alpha_I} = X_{\alpha_{II}}$ and $X_{\beta_I} = X_{\beta_{II}}$, the machine will be operated in the subspace 2 only. This mode is known as *parallel operation* [40]. Meanwhile, if the I and II components are negated, i.e. $X_{\alpha_I} = -X_{\alpha_{II}}$ and $X_{\beta_I} = -X_{\beta_{II}}$ operation will be in subspace 1, known as *antiparallel operation.*

3.2 Machine Model

For further evaluation of the modulation strategies, a proper machine model for current ripple estimation is necessary. The model should be simple enough to carry out analytical or numerical simulations quickly and to understand the observed effects. Nevertheless the model should be accurate enough to achieve a realistic behavior. In the following sections, general mathematical equations for the machine model are derived and its low- and high-frequency behavior is elaborated.

3.2.1 Mathematical Equations

Dynamical models of common three-phase machines including electrical and mechanical effects are known in the literature for a wide range of applications [50, 97, 107]. The models can be extended to multiphase machines applying the decomposition approach from section 3.1.2 as shown in [30, 35]. The decomposition technique leads to two independent α, β models for the symmetrical six-phase machine. Magnetically, these two machine models are decoupled but mechanically, they are working on the same shaft and hence their torques add up.

The applied phase voltages on the stator side $\mathbf{U}_s^p$ are divided into two parts [103]: the first one is the resistive voltage drop caused by stator current $\mathbf{I}_s^p$ and stator resistance R_s. The second part belongs to the change in stator flux $\boldsymbol{\Psi}_s^p$. The voltages can thus be expressed as:

$$\mathbf{U}_s^p(t) = R_s \mathbf{I}_s^p(t) + \frac{\mathrm{d}\boldsymbol{\Psi}_s^p(t)}{\mathrm{d}t} \tag{3.13}$$

$\boldsymbol{\Psi}_s^p(t)$ can be separated into a mutual flux of stator $\boldsymbol{\Psi}_{s,m}^p$ and rotor $\boldsymbol{\Psi}_{r,m}^p$ as shown in Figure 3.2 and a leakage stator flux $\boldsymbol{\Psi}_{s,\sigma}^p$. Assuming a ratio of one between stator and rotor winding it can be written:

$$\boldsymbol{\Psi}_s^p = \boldsymbol{\Psi}_{s,\sigma}^p + \boldsymbol{\Psi}_{s,m}^p + \boldsymbol{\Psi}_{r,m}^p = \underbrace{\mathbf{L}_{s,\sigma}^p \mathbf{I}_s^p}_{\text{Stator Leakage Flux}} + \underbrace{\mathbf{L}_m^p \left(\mathbf{I}_s^p + \mathbf{I}_r^p\right)}_{\text{Mutual Flux}} \tag{3.14}$$

Considering constant inductance amplitudes, i.e. neglecting saturation or hysteresis effects, the stator voltage equation (3.13) turns with (3.14) to:

$$\mathbf{U}_s^p(t) = R_s \mathbf{I}_s^p(t) + \mathbf{L}_{s,\sigma}^p \frac{\mathrm{d}\mathbf{I}_s^p}{\mathrm{d}t} + \mathbf{L}_m^p \frac{\mathrm{d}\left(\mathbf{I}_s^p + \mathbf{I}_r^p\right)}{\mathrm{d}t} \tag{3.15}$$

Similarly, the rotor voltage equation in phase coordinates is defined as follows:

$$\mathbf{U}_r^p(t) = \mathbf{E}^p(t) = R_r \mathbf{I}_r^p(t) + \mathbf{L}_{r,\sigma}^p \frac{\mathrm{d}\mathbf{I}_r^p}{\mathrm{d}t} + \mathbf{L}_m^p \frac{\mathrm{d}\left(\mathbf{I}_s^p + \mathbf{I}_r^p\right)}{\mathrm{d}t} \tag{3.16}$$

where $\mathbf{E}^p = \mathbf{L}_m^p \left(\mathbf{I}_s^p + \mathbf{I}_r^p\right) \omega_r$ is the electromotive force (EMF) caused by the angular velocity ω_r of the rotor with respect to the stator coils.

The machine equation in phase coordinates (3.15) and (3.16) can be expressed in a decomposed form applying the decomposition technique of section 3.1.2. Replacing $\mathbf{U}_s^p$ and $\mathbf{I}_s^p$ of the stator voltage equation with their decomposed counterpart $\mathbf{U}_s^s = \mathbf{T}_{pp}\mathbf{U}_s^p$ and $\mathbf{I}_s^s = \mathbf{T}_{pp}\mathbf{I}_s^p$ results in:

$$\begin{aligned}
&\mathbf{T}_{pp}^{-1}\mathbf{U}_s^s(t) = R_s \mathbf{T}_{pp}^{-1}\mathbf{I}_s^s(t) + \mathbf{L}_{s,\sigma}^p \frac{\mathrm{d}\mathbf{T}_{pp}^{-1}\mathbf{I}_s^s}{\mathrm{d}t} + \mathbf{L}_m^p \frac{\mathrm{d}\left(\mathbf{T}_{pp}^{-1}\left(\mathbf{I}_s^s + \mathbf{I}_r^s\right)\right)}{\mathrm{d}t} \\
\overset{\mathbf{T}_{pp}^{-1}=\text{const.}}{=}\; &\mathbf{T}_{pp}^{-1}\mathbf{U}_s^s(t) = R_s \mathbf{T}_{pp}^{-1}\mathbf{I}_s^s(t) + \mathbf{L}_{s,\sigma}^p \mathbf{T}_{pp}^{-1} \frac{\mathrm{d}\mathbf{I}_s^s}{\mathrm{d}t} + \mathbf{L}_m^p \mathbf{T}_{pp}^{-1} \frac{\mathrm{d}\left(\mathbf{I}_s^s + \mathbf{I}_r^s\right)}{\mathrm{d}t}
\end{aligned}$$

Multiplying $\mathbf{T}_{pp}$ from the left leads to:

$$\underbrace{\mathbf{T}_{pp}\mathbf{T}_{pp}^{-1}}_{=\mathbf{I}_4}\mathbf{U}_s^s(t) = \underbrace{\mathbf{T}_{pp}R_s\mathbf{T}_{pp}^{-1}}_{R_s}\mathbf{I}_s^s(t) + \underbrace{\mathbf{T}_{pp}\mathbf{L}_{s,\sigma}^p\mathbf{T}_{pp}^{-1}}_{\mathbf{L}_{s,\sigma}^s}\frac{\mathrm{d}\mathbf{I}_s^s}{\mathrm{d}t} + \underbrace{\mathbf{T}_{pp}\mathbf{L}_m^p\mathbf{T}_{pp}^{-1}}_{\mathbf{L}_m^s}\frac{\mathrm{d}\left(\mathbf{I}_s^s + \mathbf{I}_r^s\right)}{\mathrm{d}t}$$

$$\mathbf{U}_s^s(t) = R_s\mathbf{I}_s^s(t) + \mathbf{L}_{s,\sigma}^s\frac{\mathrm{d}\mathbf{I}_s^s}{\mathrm{d}t} + \mathbf{L}_m^s\frac{\mathrm{d}\left(\mathbf{I}_s^s + \mathbf{I}_r^s\right)}{\mathrm{d}t} \tag{3.17}$$

Applying the same steps to the rotor voltage equation (3.16) produces:

$$\mathbf{U}_r^s(t) = \mathbf{E}^s(t) = R_r\mathbf{I}_r^s(t) + \mathbf{L}_{r,\sigma}^s\frac{\mathrm{d}\mathbf{I}_r^s}{\mathrm{d}t} + \mathbf{L}_m^s\frac{\mathrm{d}\left(\mathbf{I}_r^s + \mathbf{I}_s^s\right)}{\mathrm{d}t} \tag{3.18}$$

The machine torque M is calculated analogously to the three-phase type [102] with the mutual flux $\mathbf{\Psi}_m^s$ and the stator current vector $\mathbf{I}_s^s$:

$$M = 3 \cdot \left(\mathbf{Z}_p \cdot \mathbf{\Psi}_m^s\right)^T \cdot \mathbf{I}_s^s \tag{3.19}$$

where $\mathbf{Z}_p$ represents the number of pole pairs for each subspace, i.e. $\mathbf{Z}_p = [1\ 1\ 2\ 2]$ for the machine type shown in Figure 3.2.

As demonstrated here, the electrical and mechanical behavior of the six-phase machine can be expressed as a set of decoupled ordinary differential equations. It is shown later that the inductance matrices $\mathbf{L}_m^s$, $\mathbf{L}_{s,\sigma}^s$, and $\mathbf{L}_{r,\sigma}^s$ and its inverted matrices are all diagonal. This offers the advantage of being less complex than a model in phase coordinates and therefore offers faster computation.

3.2.2 Low and high frequency behavior

The machine model can be further simplified if only low or high frequency behaviour is of interest. For the relatively low fundamental frequencies (usually up to 100Hz) and under idealized no load condition, i.e. the machine produces no torque, equal stator and rotor voltages can be assumed: $\mathbf{E}^s(t) = \mathbf{U}_s^s(t)$, which leads to $\mathbf{I}_r^s(t) = \mathbf{0}$. Consequently, equation (3.17) simplifies to:

$$\mathbf{U}_s^s(t) = R_s\mathbf{I}_s^s(t) + \left(\mathbf{L}_{s,\sigma}^s + \mathbf{L}_m^s\right)\frac{\mathrm{d}\mathbf{I_s^s}}{\mathrm{d}t} \tag{3.20}$$

For the relatively high switching frequencies (usually higher than 1kHz) and under idealized no load condition, the average stator voltage is still equal to the average rotor voltage for a short period of time, i.e. $\bar{\mathbf{E}}^s = \bar{\mathbf{U}}_s^s$. Adding a high frequency voltage to the average stator voltage, such that $\mathbf{U}_s^s(t) = \bar{\mathbf{U}}_s^s + \Delta\mathbf{U}_s^s(t)$, leads to the desired equations based on (3.17) and

(3.18). Assuming $\mathbf{L}_m^s >> \mathbf{L}_{s,\sigma}^s$ for every entry, as is common for induction machines, results in:

$$\Delta \mathbf{U}_s^s(t) = \mathbf{U}_s^s(t) - \bar{\mathbf{E}}^s \approx (R_s + R_r)\,\mathbf{I}_s^s(t) + \underbrace{\left(\mathbf{L}_{s,\sigma}^s + \mathbf{L}_{r,\sigma}^s\right)}_{=\mathbf{L}_\sigma^s} \frac{\mathrm{d}\mathbf{I}_\mathbf{s}^\mathbf{s}}{\mathrm{d}t} \tag{3.21}$$

where $\mathbf{L}_\sigma^s$ is the high frequency inductance matrix with entries explained in Section 3.2.4.

For machines with low mutual coupling between stator and rotor, such as synchronous machines, $\mathbf{L}_m^s \approx 0$ can be assumed and the behavior is approximated to be:

$$\Delta \mathbf{U}_s^s(t) = \mathbf{U}_s^s(t) - \bar{\mathbf{E}}^s \approx R_s \mathbf{I}_s^s(t) + \underbrace{\mathbf{L}_{s,\sigma}^s}_{=\mathbf{L}_\sigma^s} \frac{\mathrm{d}\mathbf{I}_\mathbf{s}^\mathbf{s}}{\mathrm{d}t} \tag{3.22}$$

As shown here, the machine is expressed in simplified R-L subcircuits for both, the low and high frequency case. For the two cases, the resistive voltage drop is usually small compared to the inductive voltage drop and therefore often neglected [53]. An analytical way of estimating the mutual inductance is shown in the following section 3.2.3 whereas the stator leakage parameter is discussed in section 3.2.4.

3.2.3 Mutual Inductance

An analytical way of calculating the mutual inductance matrix $\mathbf{L}_m^p$ was derived in [77] based on the stator winding distribution of the machine in Figure 3.2. The results of this work are summarized here considering the following machine properties:

- The $n = 6$ identical stator phases are connected in a double-star configuration with open neutral points and an angular displacement of $\gamma = \pi$, as shown in Figure 2.5a.

- The stator coils are slotted with $q = 4$ coils per phase, according figure 3.2, resulting in a total of $2q \cdot n = 48$ slots.

- The behaviour of stator and rotor iron is magnetic linear.

- There is no magnetic field strength in iron parts, i.e. iron permeability $\mu_{Fe} \to \infty$

- The stator and rotor surface is smooth, i.e. constant air gap width δ which is small compared to rotor and stator diameters. The slotting is considered in the analytical calculations by virtual extensions of the air gap [91].

The mutual inductance matrix $\mathbf{L}_m^p$ represents the magnetic coupling between the six stator phases and is therefore of order 6×6. It is considered that a magnetic coupling between two arbitrary phases g and h is established only if the flux path crosses the air gap two times and is closed via the iron parts of stator and rotor, as shown in Figure 3.2a and 3.2b. Each element of $\mathbf{L}_m^p$ is determined by two magneto motive force (MMF) functions $\Theta_{\delta,g}(\alpha)$ and $\Theta_{\delta,h}(\alpha)$ as well as their currents I_g and I_h. For the two arbitrary phases each entry is calculated with [117]:

$$L_{gh} = \frac{\mu_0 r_1 l}{\delta} \int_0^{2\pi} \frac{\Theta_{\delta,g}(\alpha)}{I_g} \frac{\Theta_{\delta,h}(\alpha)}{I_h} \mathrm{d}\alpha \tag{3.23}$$

where μ_0 is the magnetic permeability of vacuum, r_1 the inner stator radius, δ the air gap width, and l is the axial length of the stator.

In general, the MMF function in space is defined as the line integral over the magnetic field strength $\mathbf{H}$ along a path P (Ampère's law):

$$\Theta = \oint_P \mathbf{H} \cdot \mathrm{d}s = I \tag{3.24}$$

where I is the electric current enclosed by path P.

Laying P along the inner stator circumference gives then an expression for the individual MMF functions for each phase starting from angle α_0 and ending at α. As seen from Figure 3.2, the current density is not continuous. It is rather determined by discrete slots and an integral number of conductors per slot. Equation (3.24) can then be written as [91]:

$$\oint_P \mathbf{H} d\mathbf{s} = \left(\Theta_{\delta,g}(\alpha) - \Theta_{\delta,g}(\alpha_0)\right) = \sum_{\alpha_0}^{\alpha} I \tag{3.25}$$

The MMF value of the starting point $\Theta_{\delta,g}(\alpha_0)$ is to be estimated using Gauss's law of magnetism. Since there exist no source or sink in a magnetic circuit, the average value of $\Theta_{\delta,g}(\alpha)$ must be zero.

Applying equation (3.25) to phase a of machine geometry depicted in figure 3.2 results in the MMF function $\Theta_{\delta,a}(\alpha)$ as shown in Figure 3.1a. The function $\Theta_{\delta,a}(\alpha)$ is piecewise constant with a step height of Θ_s at the

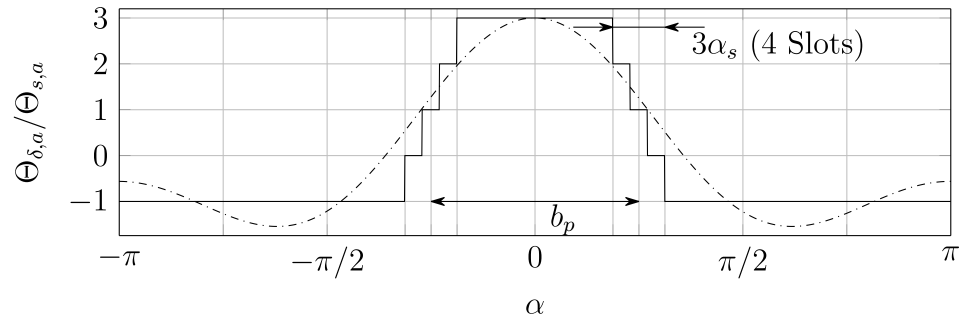

(a) MMF function $\Theta_{\delta,a}(\alpha)$ of stator phase a (black line) and Fourier series approximation with $k \in \{1,2\}$ (dashed-dotted line).

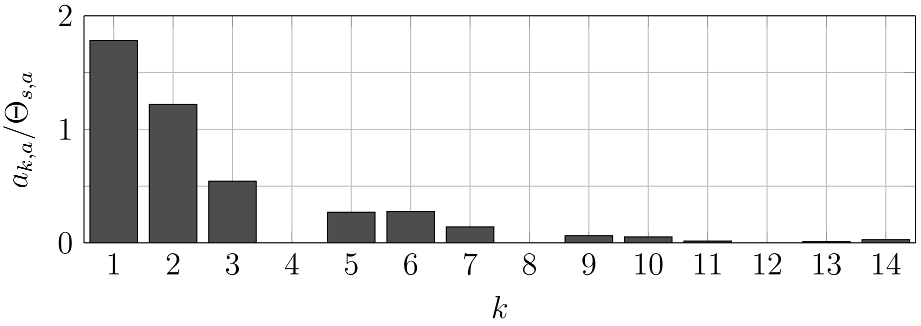

(b) Fourier Coefficients of MMF $\Theta_{\delta,a}$

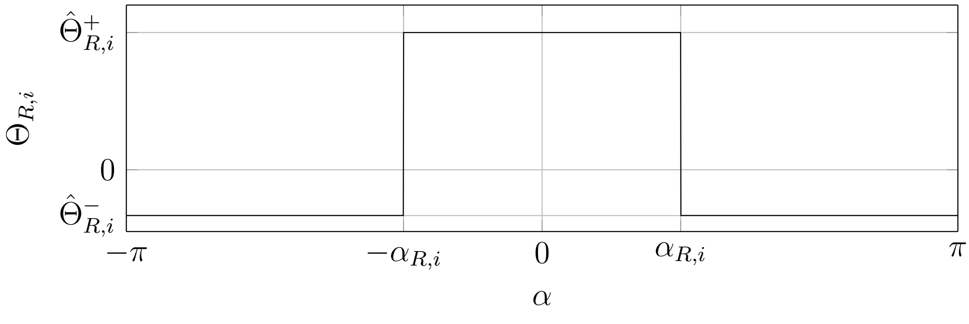

(c) Elementary rectangular MMF function $\Theta_{R,i}(\alpha)$.

Figure 3.1: Approximated and elementary MMF functions of the stator winding distribution [77].

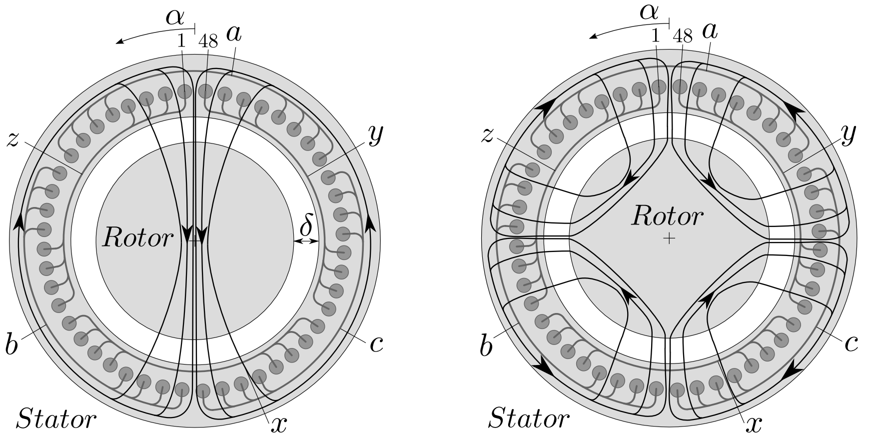

(a) Antiparallel operation mode, i.e. flux $\Psi_a = -\Psi_x$.

(b) Parallel operation mode, i.e. flux $\Psi_a = \Psi_x$.

Figure 3.2: Winding distribution of stator phases a, ... z and mutual flux paths of the six-phase machine corresponding to the modes of operation [40].

position of every slot that contains a coil of the proper phase a. The sum of all currents in a slot is:

$$\Theta_{s,a} = N_s \cdot I_a,$$

where N_s is the number of conductors in the slot, each carrying current I_a. The angular distance between two adjacent slots is calculated with in total 48 slots over 2π:

$$\alpha_s = \frac{2\pi}{48} rad \equiv 7.5^\circ$$

The mean angle of the coils of one phase b_p (see Figure 3.1a) has a strong influence on space harmonics of the MMF function. For the present machine b_p is defined as:

$$b_p = \frac{\pi}{2} rad \equiv 90^\circ$$

The discrete characteristic of $\Theta_{\delta,a}(\alpha)$ leads to high MMF harmonics which are analyzed in the following by decomposing $\Theta_{\delta,a}(\alpha)$ into elementary rectangular functions $\Theta_{R,i}(\alpha)$ as seen in figure 3.1c. Their relationship is:

$$\Theta_{\delta,a}(\alpha) = \sum_{i=1}^{4} \Theta_{R,i}(\alpha). \qquad (3.26)$$

The elementary function $\Theta_{R,i}(\alpha)$ is defined by different parameters $\hat{\Theta}_{R,i}^{-}$ $\hat{\Theta}_{R,i}^{+}$ and $\alpha_{R,i}$ for every $i \in \{1,2,3,4\}$ (see Figure 3.1c). The mean value of every $\Theta_{R,i}(\alpha)$ must be zero, which is fulfilled with the following expression:

$$\hat{\Theta}_{R,i}^{-} = -\hat{\Theta}_{R,i}^{+} \frac{\alpha_{R,i}}{\pi - \alpha_{R,i}}.$$

Furthermore, the step height $\hat{\Theta}_{R,i}^{+}$ of the elementary function can be expressed through the step height of the approximated MMF function $\Theta_{s,a}$ with:

$$\hat{\Theta}_{R,i}^{+} = \Theta_{s,a} \frac{\pi - \alpha_{R,i}}{\pi}.$$

According to the machine geometry as shown in figure 3.1a the angles $\alpha_{R,i}$ are:

$$\alpha_{R,i} = \begin{cases} \frac{b_p - 3\alpha_s}{2}, & i = 1 \\ \frac{b_p - \alpha_s}{2}, & i = 2 \\ \frac{b_p + \alpha_s}{2}, & i = 3 \\ \frac{b_p + 3\alpha_s}{2}, & i = 4 \end{cases}$$

Together with the aforementioned parameters the MMF functions $\Theta_{\delta,a}(\alpha)$ and $\Theta_{R,i}(\alpha)$ can be represented in a Fourier series $(\mathcal{F}f)(\alpha)$ of $f(\alpha)$. Since both functions are symmetric, i.e. $\Theta_{\delta,a}(\alpha) = \Theta_{\delta,a}(-\alpha)$ and $\Theta_{R,i}(\alpha) = \Theta_{R,i}(-\alpha)$ and the mean value must be zero, the coefficients of the Fourier series must be:

$$\begin{aligned} \Theta_{R,i}(\alpha) &= \sum_{k=1}^{\infty} a_{k,i} \cos(k\alpha), \text{with} && (3.27) \\ a_{k,i} &= \frac{1}{\pi} \int_{-\pi}^{\pi} \Theta_{R,i}(\alpha) \cos(k\alpha) \, \mathrm{d}\alpha \\ &= \frac{2}{k\pi} \Theta_{s,a} \sin(k\alpha_{R,i}) \text{ and} \\ \Theta_{\delta,a}(\alpha) &= \sum_{i=1}^{4} \Theta_{R,i}(\alpha) = \sum_{k=1}^{\infty} a_{k,a} \cos(k\alpha), \text{with} && (3.28) \\ a_{k,a} &= \sum_{i=1}^{4} a_{k,i} = \frac{4}{k\pi} \Theta_{s,a} \sin\left(\frac{k}{2} b_p\right) \left(\cos\left(\frac{k}{2} 3\alpha_s\right) + \sin\left(\frac{k}{2} \alpha_s\right)\right). \end{aligned}$$

Recalling equation (3.23), the coupling inductance between two arbitrary phases g and h can then be expressed as a Fourier series with the offset angles

α_g and α_h

$$\begin{aligned} L_{gh} &= \frac{\mu_0 r_1 l}{\delta} \int_0^{2\pi} \left(\sum_{k=1}^{\infty} \frac{a_{k,g}}{I_g} \cos\left(k\alpha - k\alpha_g\right) \right) \left(\sum_{k=1}^{\infty} \frac{a_{k,h}}{I_h} \cos\left(k\alpha - k\alpha_h\right) \right) \mathrm{d}\alpha \\ &= \frac{\mu_0 r_1 l \pi}{\delta} \sum_{k=1}^{\infty} \frac{a_{k,g} a_{k,h}}{I_g I_h} \cos\left(k\left(\alpha_g - \alpha_h\right)\right) \end{aligned}$$

All stator coils exhibit the same distribution, i.e. $a_{k,a} = a_{k,g} = a_{k,h}$:

$$L_{gh} = \frac{16 \mu_0 r_1 l N_s^2}{\pi \delta} \sum_{k=1}^{\infty} \frac{1}{k^2} \sin\left(\frac{k}{2} b_p\right)^2 \left(\cos \frac{3k}{2}\alpha_s + \cos \frac{k}{2}\alpha_s\right)^2 \cos\left(k\left(\alpha_g - \alpha_h\right)\right) \tag{3.29}$$

The self inductance L_{ss} is achieved by setting $g = h$:

$$\begin{aligned} L_{ss} &= \frac{\mu_0 r_1 l \pi}{\delta} \sum_{k=1}^{\infty} \frac{a_{k,a}^2}{I_a^2} \\ &= \frac{16 \mu_0 r_1 l N_s^2}{\pi \delta} \sum_{k=1}^{\infty} \frac{1}{k^2} \sin\left(\frac{k}{2} b_p\right)^2 \left(\cos \frac{3k}{2}\alpha_s + \cos \frac{k}{2}\alpha_s\right)^2 \end{aligned}$$

The resulting mutual inductance matrix in phase coordinates is then estimated with every stator phase combination. Here, it is expected that the mutual magnetic field is well approximated with $k \in \{1, 2\}$ as shown in Figure 3.1a. This assumption leads to:

$$\mathbf{L}_m^p = L_{ss} \begin{bmatrix} 1.000 & -0.500 & -0.500 & -0.319 & 0.181 & 0.181 \\ -0.500 & 1.000 & -0.500 & 0.181 & -0.319 & 0.181 \\ -0.500 & -0.500 & 1.000 & 0.181 & 0.181 & -0.319 \\ -0.319 & 0.181 & 0.181 & 1.000 & -0.500 & -0.500 \\ 0.181 & -0.319 & 0.181 & -0.500 & 1.000 & -0.500 \\ 0.181 & 0.181 & -0.319 & -0.500 & -0.500 & 1.000 \end{bmatrix} \tag{3.30}$$

In a decomposed form, the mutual inductance matrix $\mathbf{L}_m^s$ is:

$$\mathbf{L}_m^s = \mathbf{T}_{pp} \cdot \mathbf{L}_m^p \cdot \mathbf{T}_{pp}^{-1} = L_{ss} \begin{bmatrix} 2.00 & 0 & 0 & 0 \\ 0 & 2.00 & 0 & 0 \\ 0 & 0 & 1.00 & 0 \\ 0 & 0 & 0 & 1.00 \end{bmatrix} \tag{3.31}$$

As seen from equation (3.31) the diagonal inductance matrix shows equal values for the α and β-components of both subspaces, i.e. L_{m_1} for the first and L_{m_2} for the second subspace. This result can be explained by the equally distributed phases around the stator circumference. Furthermore, it is estimated that $L_{m_1} > L_{m_2}$, which reflects the relation between the first and second Fourier coefficient of the MMF function in figure 3.1b.

Comparing the the estimated results of equation (3.31) with the machine parameters of Table 3.1 (without transformer), the calculated ratio $\frac{L_{m_1}}{L_{m_2}} = 2$ corresponds very well to the measured one $\frac{L_{m_1}}{L_{m_2}} = \frac{220}{115} \approx 1.9$. As it is shown in the following sections, the ratio plays a important role for determining the overall current distortions.

3.2.4 Leakage Inductance

The leakage inductance represents the magnetic non-coupling of the stator and rotor. Therefore the flux path will cross through the rotor but not the stator, or vice-versa. This is why the total leakage is dependent on the rotor ($L_{r,\sigma}$) and stator ($L_{s,\sigma}$) contributions.

As seen from equations (3.21) and (3.22) the leakage inductance has a significant influence on the machine's high frequency behavior. In the literature it is stated that the stator and rotor coil exhibit "a relatively small but nontrivial resistance"[52] and therefore the voltage-current characteristic is usually modeled as a lossy inductance [53].

For a three-phase machine, this high-frequency leakage inductance L_σ is expressed as [52]:

$$L_\sigma = L_{s,\sigma} + \frac{L_m L_{r,\sigma}}{L_m + L_{r,\sigma}} \tag{3.32}$$

For induction machines L_m is usually much greater than $L_{s,\sigma}$ or $L_{r,\sigma}$, which achieves: $L_\sigma \approx L_{s,\sigma} + L_{r,\sigma}$. For the case of a very low mutual coupling between stator and rotor ($L_m \approx 0$), such as for synchronous machines, it can be approximated: $L_\sigma \approx L_{s,\sigma}$.

An analytical method to estimate its value for a variety of machines and with sufficient accuracy is not known yet. Applying the same simplifications of section 3.2.3 for calculating the mutual inductance would lead to a significant difference compared to measured results. This is due to the fact that the flux does not necessarily flow within the air gap around the circumference but also between the individual slots.

In the literature there are a variety of numerical methods known for calculating leakage inductances, incorporating winding distribution and geometric machine properties such as stator and rotor slotting. The methods can be divided into reluctance networks [118], Finite Difference (FD) [75], and Finite Element (FE) [8].

Assuming linear behavior, a magnetic circuit can be expressed analogously to an electric (reluctance) circuit with a source and a resistance. A machine can be divided into several such circuits resulting in a so called "reluctance network". In contrast, the FD and FE method divide the area or volume of interest into discrete sub-areas or sub-volumes (elements) of a certain size and form. The bounding conditions of each element are then calculated by a differential equation.

The FD and FE methods usually lead to a system with a higher number of equations and therefore a higher calculation effort but precise results and a higher resolution. The reluctance network has fewer calculation steps and is therefore well suited for a rough estimation of the electromagnetic behavior and can be used for optimization of the machine design. An optimized design, however, is not in the scope of this thesis. The interested reader is referred to [93, 113].

Here, the given machine design of Figure 3.2 is further analyzed with respect to its stator and rotor leakage inductance. According to the transformation theory of section 3.1, the machine behavior can be expressed in a decomposed form. Assuming equal structures in the α, β-directions, there must be two different values of the high-frequency leakage inductance for both subspaces: L_{σ_1} and L_{σ_2}. Therefore $\mathbf{L}_\sigma^s$ is defined as:

$$\mathbf{L}_\sigma^s = \begin{bmatrix} L_{\sigma_1} & 0 & 0 & 0 \\ 0 & L_{\sigma_1} & 0 & 0 \\ 0 & 0 & L_{\sigma_2} & 0 \\ 0 & 0 & 0 & L_{\sigma_2} \end{bmatrix} \tag{3.33}$$

The consideration of a simple inductance model is validated by experiments. The machine was fed with a rectangular voltage waveform and a phase current was measured, as depicted in Figure 3.4. An excitation in the first subspace is achieved here according to (3.12) with: $U_a(t) = -U_x(t)$, $U_b(t) = -U_y(t)$, and $U_c(t) = -U_z(t)$ for any t. In contrast, the same voltage waveform in the second subspace is reached with $U_a(t) = U_x(t)$, $U_b(t) = U_y(t)$, and $U_c(t) = U_z(t)$. The same relation can be stated for the current in both subspaces, such that analyzing the voltage and current waveform of a single phase is sufficient.

Over one period, the voltage signal is expressed as a Fourier series consisting of a fundamental sinus wave with frequency f_s, amplitude $\hat{U}$, and a sum of several harmonics. The resulting current waveform is also expressed as a Fourier series with the fundamental wave at frequency f_s and amplitude $\hat{I}$ but shifted with φ towards the fundamental voltage wave. Both fundamental waves are:

$$\begin{aligned} U\left(f_s,t\right) &= \hat{U}\left(f_s\right)\sin\left(f_s 2\pi t\right) \\ I\left(f_s,t\right) &= \hat{I}\left(f_s\right)\sin\left(f_s 2\pi t + \varphi\left(f_s\right)\right) \end{aligned} \tag{3.34}$$

The current response of the system depending on f_s can then be expressed with the ratio (magnitude) of the amplitudes $\hat{U}, \hat{I}$ and the phase angle φ. Analog to Bode's control theory [12], the magnitude M given by the decibel gain expression with the base-10 logarithm is:

$$M\left(f_s\right) = 20\log_{10}\left(\frac{\hat{I}}{\hat{U}}\right) \tag{3.35}$$

The magnitude and phase angle values over the frequency range $f_s \in [1kHz, 16kHz]$ based on experimental results are depicted in Figure 3.3. Since the voltage waveform can be applied in either one of the two subspaces, there are two magnitude curves M_1 and M_2 as well as two phase angle curves φ_1 and φ_2. Additionally, the experimental setup offers an optional transformer which links inverter and machine as shown in Section 3.4. Thus the behavior can be examined for both subspaces, with or without the transformer.

As seen in the figure, when a transformer is omitted the magnitude and phase angle of both subspaces are nearly equal over the frequency range. Plotted over the logarithm of frequency the $M_1(f_s)$ and $M_2(f_s)$ can be approximated as a straight line with a gradient of -20dB per decade. The phase angles lie in the range of $-80 < \varphi < -60$ degrees, such that the system behavior extracted from magnitude and angle can be seen as strongly inductive in both subspaces with the values $L_{\sigma_1} = L_{\sigma_2}$.

Meanwhile, the transformer changes the behavior with particularly interesting effects at high frequencies, as depicted in Figure 3.3. The magnitude M_{2t} and phase angle φ_{2t} in the second subspace are nearly equal to those without a transformer. The first subspace, however, shows a much greater damping of M_{1t}. Furthermore, the phase angle φ_{1t} shows the behavior to be inductive for 1kHz $< fs <$ 4kHz and resistive for 4kHz $< fs <$ 6kHz. For even higher frequencies, the response is capacitive.

In contrast to the idealized inductive behavior, the real system shows increasing resistive effects in the range of 1-6kHz. This might be caused by hysteresis effects and eddy-currents within the stator and rotor metal plates. At even higher frequencies, the increasingly capacitive behavior might be caused by the wires and windings within the machine. As mentioned in [13] the conductors of each stator winding have a small parasitic capacity towards

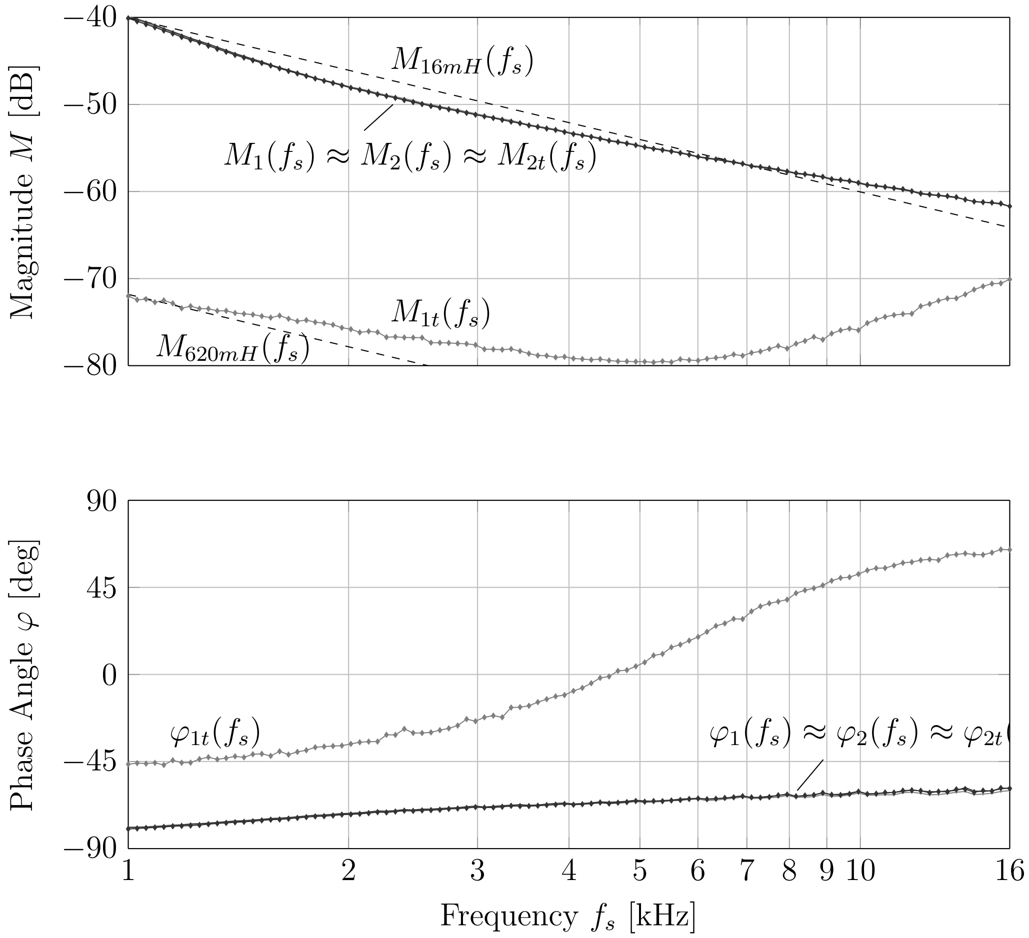

Figure 3.3: High frequency voltage-current characteristics of the present six-phase machine. Experimentally gathered results of magnitude and phase angle of both decomposed subspaces with $(M_{1t}, M_{2t}, \varphi_{1t}, \varphi_{2t})$ and without transformer$(M_1, M_2, \varphi_1, \varphi 2)$. Dashed line: magnitude characteristics of inductances $L = 16mH$ and $L = 620mH$ respectively.

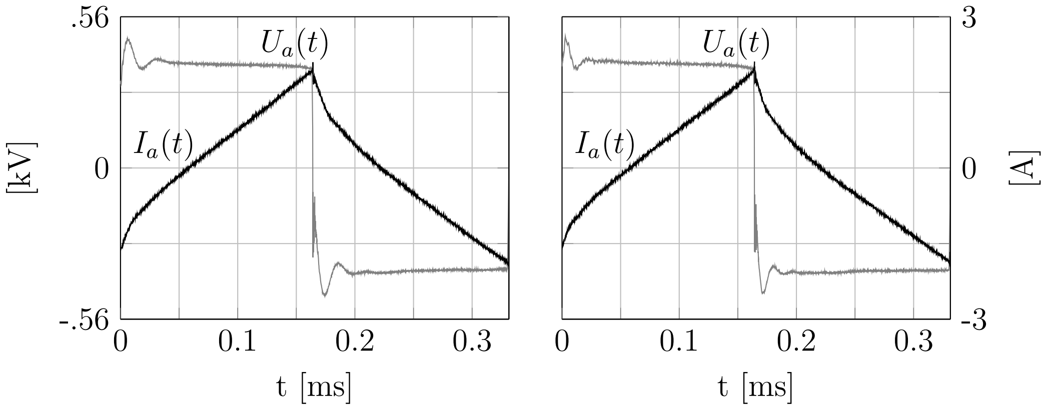

(a) Excitation in first subspace.

(b) Excitation in second subspace.

Figure 3.4: Voltage current characteristic of phase a during a switching period at $f_s = 3kHz$.

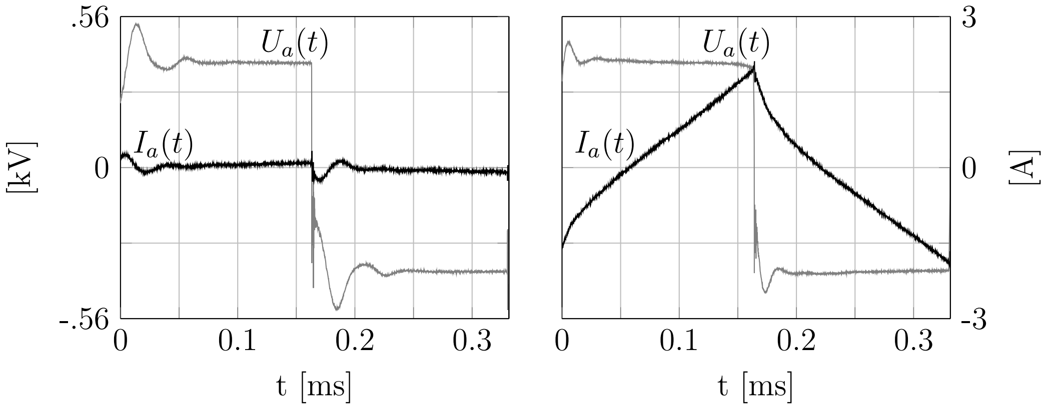

(a) Excitation in first subspace.

(b) Excitation in second subspace.

Figure 3.5: Voltage current characteristic of phase a during a switching period at $f_s = 3kHz$ with additional transformer.

ground and towards the nearby winding. The effect becomes visible when high frequencies are of interest, as seen in the current response.

In Figure 3.4 the current of phase a is shown on a timescale. The phase current of the two subspaces responds almost identically to excitation, which corresponds to Figure 3.3. As stated before, the system behavior shows slightly capacitive effects which are visible in Figures 3.4a and 3.4b after a sudden change in phase voltage. The capacitive behavior can be neglected here, but it becomes more important if a short time period or high switching frequencies are under scope (compare with Figure 3.3).

The stronger capacitive effect is also visible on a time basis in Figure 3.5a. As seen there, a sudden change in phase voltage results in an oscillation around the zero value. Furthermore, the inductance value is much higher, such that the current slope is significantly reduced. The current response in subspace two, however, does not show any relevant difference compared to the one without transformer (compare Figure 3.5b with 3.4b).

For further studies the system response for the case with transformer is assumed as strictly inductive in both subspaces with the inductances $L_{\sigma_1} >> L_{\sigma_2}$. As it will be shown, the assumption reduces complexity but still the model reaches sufficient accuracy compared to reality.

For further calculations, it is advantageous using a leakage induction ratio factor κ rather than the absolute values. The factor refers the inductance of the first subspace to the one of the second subspace:

$$\kappa = \frac{L_{\sigma_1}}{L_{\sigma_2}} \tag{3.36}$$

For the case without transformer a ratio of $\kappa \approx 1$ can be approximated, whereas with transformer $\kappa >> 1$ is achieved (see Table 3.1).

3.2.5 Equivalent Circuits and Machine Parameters

Section 3.1.1 to 3.2.4 lead to a machine model for the low- and high-frequency electrical behaviour. The model can be expressed with mathematical formulas and visualized in T-equivalent circuits [102]. The circuits include the mutual and leakage inductances as well as the stator and rotor resistances as parameters.

Since here, the high-frequency behaviour is of interest, the T-circuits for each decomposed dimension of the six-phase machine can be reduced to a simple leakage inductance. The current is driven by the voltage $\Delta U = U - E$, where U is the voltage applied and E is the induced voltage, also known as electromotive force (EMF). The one-dimensional models are valid for the corresponding alpha and beta dimension, but can be extended with

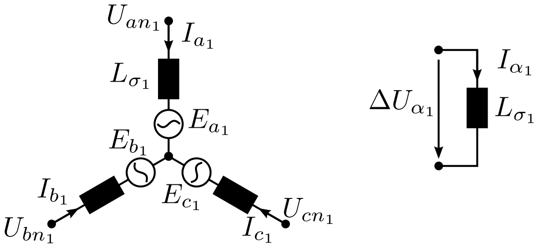

Figure 3.6: Equivalent circuit (EC) of the first subspace. The EC of the second subspace is identical but its parameter values are denotes with a subscripted 2.

the inverse Clarke transformation of section 3.1.1 to a three-phase circuit. Figure 3.6 shows both circuit types for the first subspace, which will be used in the following chapters.

Parameter	With transf.	Without transf.
R_s	733 mΩ	733 mΩ
R_r	368 mΩ	368 mΩ
L_{m_1}	830 mH	220 mH
L_{m_2}	115 mH	115 mH
L_{σ_1}	620 mH	16 mH
L_{σ_2}	16 mH	16 mH

Table 3.1: Model parameters of the six-phase machine with and without transformer

The machine parameters that will be used for simulations are summarized in Table 3.1. All parameters are gathered from experimental data. The inductances and the rotor resistance values are achieved with a no load test (see section 3.2.2) and a high frequency excitation test (see section 3.2.4). The stator resistance is calculated through a simple stator DC-voltage and -current division.

3.3 Inverter Model

The six-phase drive setup is controlled by the means of two identical three-leg inverters, each leg connected to the corresponding machine phase as shown in Figure 3.7. The two-level voltage source inverters (VSIs) could be connected either in series, sharing the DC-link voltage, or in parallel, sharing the DC-link current. The analyzing techniques and results of this work are independent of the type of interconnection. Anyway, only equal and constant DC-link voltages U_d for the VSIs are assumed.

The inverter modules exhibit in total six half-bridges, each consisting of two switches. The purpose of the bridges is to establish a connection between either the upper $(+\frac{U_d}{2})$ or the lower $(-\frac{U_d}{2})$ DC-voltage and the inverters outputs. The switches are considered as idealized, i.e. there is no voltage drop during on-time and no leakage current during off-time. In order to avoid short circuit, one switch of a half-bridge is open and one is closed at all times, i.e. S_1 is open and S_4 is closed or vice versa. A change of the output voltage occurs immediately, i.e. there is no time delay or minimum pulse width.

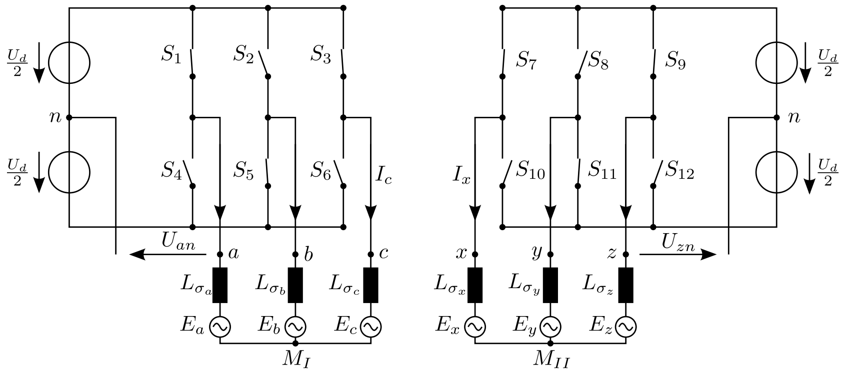

Figure 3.7: Two three-leg, two-level VSIs and high-frequency model of a six-phase machine

3.3.1 Inverter Leg and Phase Voltages

The inverter output voltages U_{gn} of inverter legs $g \in \{a, b, c, x, y, z\}$ are defined towards the inverter neutral point n. A switch function s_g is defined as:

$$s_g = \begin{cases} 1, & \text{Upper switch } S_g \text{ of leg } g \text{ is closed, i.e. } U_g = +\frac{U_d}{2} \\ 0, & \text{Lower switch } S_g \text{ of leg } g \text{ is closed, i.e. } U_g = -\frac{U_d}{2} \end{cases} \tag{3.37}$$

The inverter leg voltages U_{gn} are then expressed with:

$$\underbrace{[U_{an}\ U_{bn}\ U_{cn}\ U_{xn}\ U_{yn}\ U_{zn}]^T}_{U_{gn}} = U_d \cdot \underbrace{\left([s_a\ s_b\ s_c\ s_x\ s_y\ s_z]^T - \frac{1}{2} \cdot \mathbf{1}_{6\times1}\right)}_{s} \tag{3.38}$$

where $s = [s_a \cdots s_z]^T$ represents the vector of switch positions and $\mathbf{1}_{6\times1}$ is a identity vector with six rows.

The line-to-line voltages between two legs of the same inverter, e.g. legs a, b, c are defined as:

$$\begin{bmatrix} U_{ab} \\ U_{bc} \\ U_{ca} \end{bmatrix} = \begin{bmatrix} 1 & -1 & 0 \\ 0 & 1 & -1 \\ -1 & 0 & 1 \end{bmatrix} \cdot \begin{bmatrix} U_{an} \\ U_{bn} \\ U_{cn} \end{bmatrix} \tag{3.39}$$

The machine's phase voltages $U_a \dots U_z$ are measured between the connection points $a \dots z$ and the star point of the corresponding three-phase set M_I or M_{II} (see Figure 3.7). Assuming equal machine characteristics for all phases (symmetrical load) it can be stated that:

$$U_a + U_b + U_c = U_x + U_y + U_z = 0.$$

A relation between inverter leg and machine phase voltages of set I can then be found with

$$\begin{aligned} \begin{bmatrix} U_a \\ U_b \\ U_c \end{bmatrix} &= \begin{bmatrix} 1 & -1 & 0 \\ 0 & 1 & -1 \\ 1 & 1 & 1 \end{bmatrix}^{-1} \cdot \begin{bmatrix} U_{ab} \\ U_{bc} \\ 0 \end{bmatrix} \\ &= \begin{bmatrix} \frac{2}{3} & -\frac{1}{3} & -\frac{1}{3} \\ -\frac{1}{3} & \frac{2}{3} & -\frac{1}{3} \\ -\frac{1}{3} & -\frac{1}{3} & \frac{2}{3} \end{bmatrix} \cdot \begin{bmatrix} U_{an} \\ U_{bn} \\ U_{cn} \end{bmatrix} \end{aligned} \tag{3.40}$$

Equation (3.40) can easily be adapted to set II by changing the phase indices a, b, c to x, y, z.

3.3.2 Voltage Vectors and Modulation Index

Focusing on a three-phase set with the phases a, b, c there exist $2^3 = 8$ different switching states for the VSI. Applying the Clarke transformation of equation (3.3) maps the resulting leg voltages onto an $\alpha\beta$-plane:

$$\begin{bmatrix} U_{\alpha_I} \\ U_{\beta_I} \end{bmatrix} = \mathbf{T_C} \cdot \begin{bmatrix} U_{an} \\ U_{bn} \\ U_{cn} \end{bmatrix} \tag{3.41}$$

The transformation of the leg voltages results in six active voltage vectors with an amplitude of $\hat{U} = \frac{2}{3} U_d$ and two zero voltage vectors. As shown in Figure 3.8 the active vectors form a hexagon in the $\alpha\beta$-plane. Switching the active vectors one ofter another, i.e. with the switching states $100, 110, 010, 011, 001, 101$, the connected load is operated in the so called *six-step mode* [53]. This type of operation causes a fundamental waveform with the maximum voltage amplitude $\hat{U}_{SS}$ achievable for this configuration. Its fundamental value can be calculated by representing the waveform function as a Fourier series (see equation (3.27)). For symmetry reasons, it is sufficient to define the six-step waveform $U_{SS}(\omega_0 t)$ of one dimension within $0 \leq \omega_0 t \leq \frac{\pi}{2}$, i.e.:

$$U_{SS}(\omega_0 t) = \begin{cases} \frac{2}{3}U_d, & \text{for } 0 \leq \omega_0 t \leq \frac{\pi}{6} \\ \frac{1}{3}U_d, & \text{for } \frac{\pi}{6} < \omega_0 t \leq \frac{\pi}{2} \end{cases} \tag{3.42}$$

The fundamental waveform amplitude is then computed with a constant angular speed, i.e. $\omega_0 = const.$:

$$\begin{aligned} \hat{U}_{SS} &= \frac{4}{\pi}\omega_0 \int_0^{\pi/2} U_{SS}(\omega_0 t)\cos(\omega_0 t)dt \\ &= \frac{4}{\pi}U_d\omega_0 \left(\int_0^{\pi/6} \frac{2}{3}\cos(\omega_0 t)dt + \int_{\pi/6}^{\pi/2} \frac{1}{3}\cos(\omega_0 t)dt \right) = \frac{2}{\pi}U_d \end{aligned} \tag{3.43}$$

In the following considerations, the concept of modulation index M is particularly useful. This value represents the ratio of the inverter leg voltage amplitude $\hat{U}$ to the maximum fundamental magnitude $\hat{U}_{SS}$:

$$M = \frac{\hat{U}}{\hat{U}_{SS}} \tag{3.44}$$

The modulation index of the active voltage vectors is then $M = \frac{\pi}{3}$, as depicted in Figure 3.8. The fundamental wave of the six-step operation, consequently, is a unity circle in this diagram.

Applying a sine-triangle pulse width modulation (PWM) technique as shown in section 5, one achieves the maximum leg voltage amplitude of $\hat{U}_g = \frac{U_d}{2}$. Without adding any harmonics on the reference voltage waveform, a modulation index of $M \leq \frac{\pi}{4}$ can be covered with this scheme. In section 6, space vector modulation (SVM) methods are elaborated, which are capable of covering a greater circular area within the hexagon. The maximum modulation index achievable with those schemes is $M = \sqrt{\frac{\pi}{3}^2 - \frac{\pi}{6}^2} = \frac{\pi}{2\sqrt{3}} \approx 0.91$.

The operation of the inverter between $\frac{\pi}{2\sqrt{3}} < M < \frac{\pi}{3}$, named *overmodulation range*, and is not addressed in this work. The reader is referred to [53] for further information about this topic.

Changing the point of view to the six-phase system level yields $2^6 = 64$ different inverter switching states. The corresponding leg voltages can be mapped similar to the three-phase case onto two decoupled planes. The

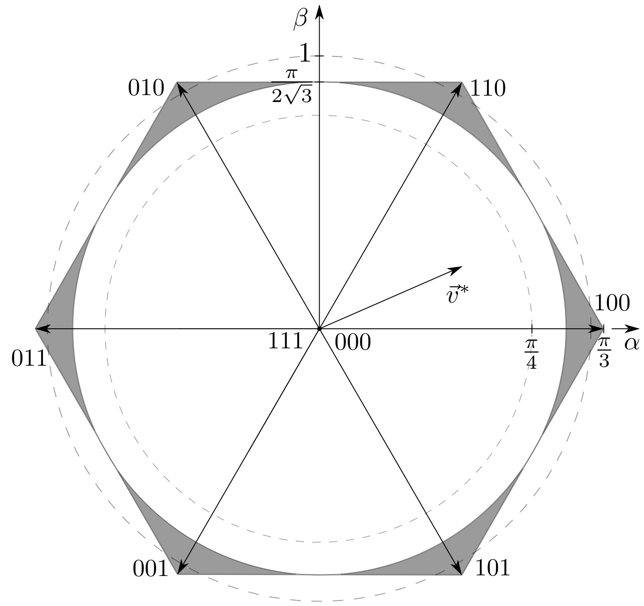

Figure 3.8: Normalized voltage space vectors and corresponding switching states on the α, β plane of a three phase set. Outer dashed circle exhibits a radius of one, inner dashed circle limits the modulateable area of the sine-triangle PWM. White circular area within the hexagon is covered by SVM.

normalized voltage vectors $v_{\alpha_1}, v_{\beta_1}, v_{\alpha_2}, v_{\beta_2}$ are achieved with matrix $\mathbf{T}_{pp}$ of equation (3.5) and $\hat{U}_{SS}$ of equation (3.43):

$$\begin{bmatrix} v_{\alpha_1} \\ v_{\beta_1} \\ v_{\alpha_2} \\ v_{\beta_2} \end{bmatrix} = \frac{1}{\hat{U}_{SS}} \cdot \mathbf{T_{pp}} \cdot \begin{bmatrix} U_{an} & U_{bn} & U_{cn} & U_{xn} & U_{yn} & U_{zn} \end{bmatrix}^T \tag{3.45}$$

Projecting the leg voltages as vectors onto both predefined subspaces reveals three possible magnitudes in addition to the zero vector (see Figure 3.9). These are classified as long, medium, and small sized with the magnitudes $\frac{\pi}{3}$, $\frac{\pi}{2\sqrt{3}}$, and $\frac{\pi}{6}$ respectively. In both the (α_1, β_1) and (α_2, β_2) subspaces, the long and medium vector projections form a regular hexagon, which exhibit the same shape as for the three-phase case (compare with Figure 3.8). The small vectors span out additional hexagons on both planes with the half sized length.

Each switching state depicted in Figure 3.9a and 3.9b produces a vector in both subspaces. A certain long vector in a subspace can only be achieved with one combination, which produces a zero vector in the other subspace. Medium sized vectors however can be generated with two different states, which itself causes small sized vectors in the other subspace. Small sized vectors provoke again small or medium sized vectors on the other plane.

3.4 Experimental Setup

The test bench setup seen in Figure 3.10 was used to validate the previously discussed models. Experimental tests were carried out with a 15kW, six-phase induction machine. The 400V AC grid voltage is converted to a DC voltage by a diode rectifier, and two three-phase inverters are connected in parallel to the DC bus.

Recall that the six-phase machine can be split into two sets of three phases. The six inverter legs (a, b, c, x, y, and z) may be connected directly to the six-phase machine, or via the three-phase transformer, as mentioned in section 3.2.4. The transformer has three coils on both the primary and secondary side. Inverter legs a, b, and c are connected to the first terminal of each of the three primary coils, and machine phases a', b', and c' are are linked with the respective coil on the secondary side. Similarly, legs x, y, and z on the primary side are coupled with machine phases x', y', and z' on the secondary side. This linkage leads to $\kappa >> 1$ due to the strong coupling between phases a' and x', b' and y', as well as c' and z'.

A separate drive unit with an electric load machine and inverter was used to control the mechanical part, ensuring constant speed and no-load conditions for the duration of the test. The load inverter is connected directly to the DC-Link (not shown in the figure).

Current sensors measure the phase currents $I_a, \ldots, I_z$ at the inverters output and the DC-link current I_d. An additional voltage measurement at the DC-Link enables to estimate the input power of the six-phase drive. A torque transducer between the machines is capable of measuring the output power with torque T and rotational speed N of the drive.

A vibration sensor is mounted onto the casing of the six-phase machine, metering the radial acceleration a. The six-phase drive is controlled with a real-time system of dSPACE with the components listed in Table 3.2. The system comprises amongst others a processor card for calculation purposes and a programmable digital IO-card for the generation of switching signals. The measurement signals were recorded with an oscilloscope of LeCroy capable of dealing with high frequencies while offering a high vertical resolution. With an additional personal computer, the real-time system and the oscilloscope were programmed and triggered for automated test runs. In figures A.1 and A.2 photos of the test bench are given.

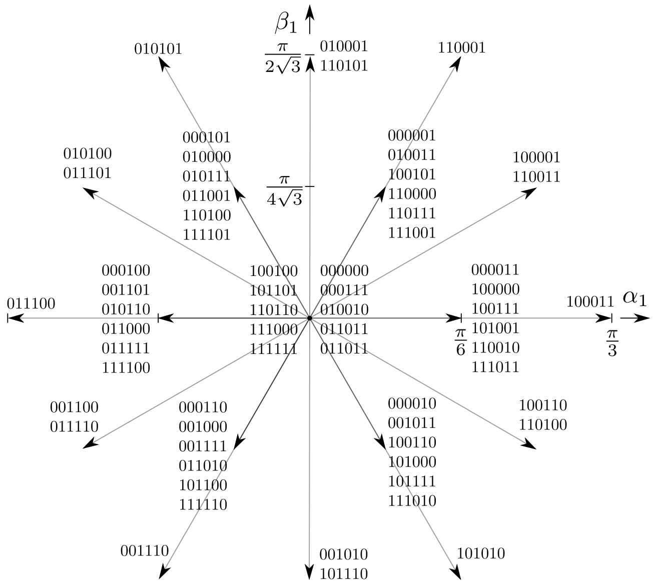

(a) First subspace.

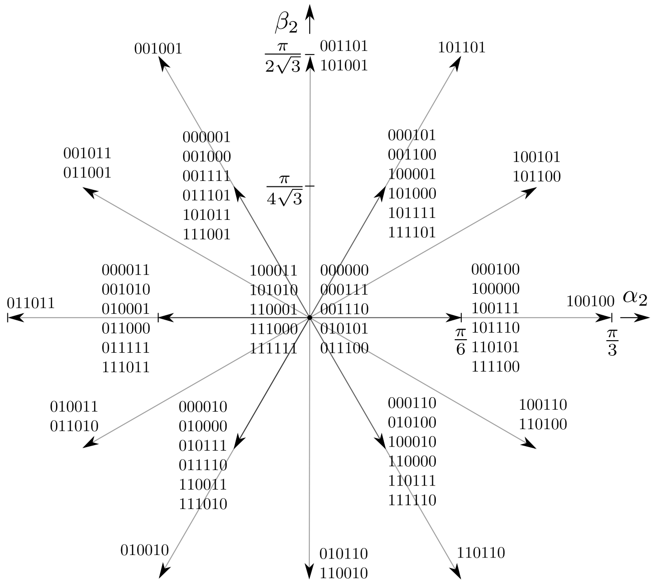

(b) Second subspace.

Figure 3.9: Voltage space vectors and switching states.

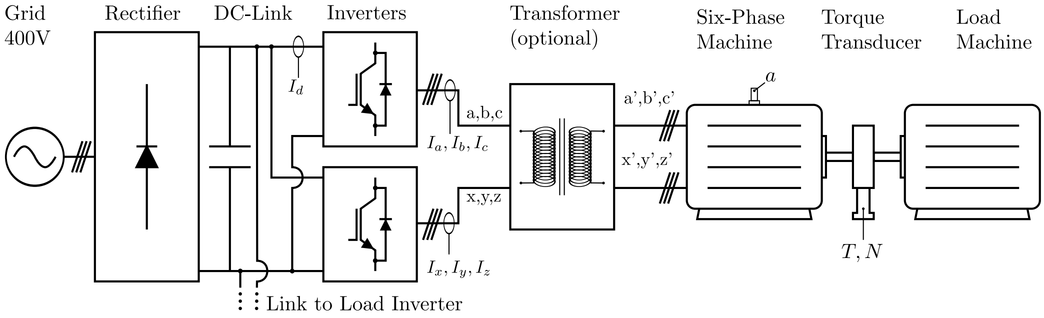

Figure 3.10: Experimental setup featuring a diode-rectifier, two three-leg inverters, and an optional transformer alongside a six-phase induction machine.

	Components	Specifications
Real-Time System	Processor Card DS1005	1Ghz
	A/D Board DS2004	16bit, 800nS
	DIO Board DS5101	25nS
	Encoder Board DS3002	32bit, 750kHz
Oscilloscope	LeCroy HDO6054	12Bit, 500Mhz
	Current Probe	30A rms, 50Mhz
	Differential Voltage Probe	1.4kV, 100Mhz

Table 3.2: Experimental Equipment and Specifications

Chapter 4

Analyzing Techniques for Pulsewidth Modulation

Voltage source inverters (VSIs) are widely applied in DC-AC energy converters, such as drive systems or uninterruptible power supplies (UPS). The output voltage of such a VSI contains a low-frequency fundamental wave, which is controllable by means of a modulator in magnitude, frequency and phase. The modulator sets the on-to-off ratios (duty cycles) for semiconductors working exclusively in switched mode. The objective is to achieve the same value of volt-seconds as the reference voltage waveform for a short period of time. The so excited current waveform of an inductive load contains not only the desired fundamental wave but also additional and unwanted high-frequency harmonics, as shown in Figure 4.1.

Current harmonics are responsible for extra copper losses, torque harmonics and acoustic noise. It is clear that these negative side effects could be reduced by setting the switching frequency f_s preferably high. But f_s is limited by the power losses of the semiconductors and its temperature resistance. The resistance is part of the converter design process and is not further addressed here. The power losses, however, are of interest as they are determined by the pattern of switching pulses.

The converter power losses can be divided into two parts: the relatively low conduction losses at on- or off-state and the losses caused by transition between two switching states (switching losses). Since the maximum value of f_s is mainly limited by the switching losses, a proper pulse pattern has to be applied in order to reduce current distortions on the load side.

The modulation strategy therefore plays an important role for improving the overall efficiency of a given drive system. It also effects vibrations and dynamic performance as will be shown later on.

Modulation techniques can be distinguished into fixed-frequency and variable-

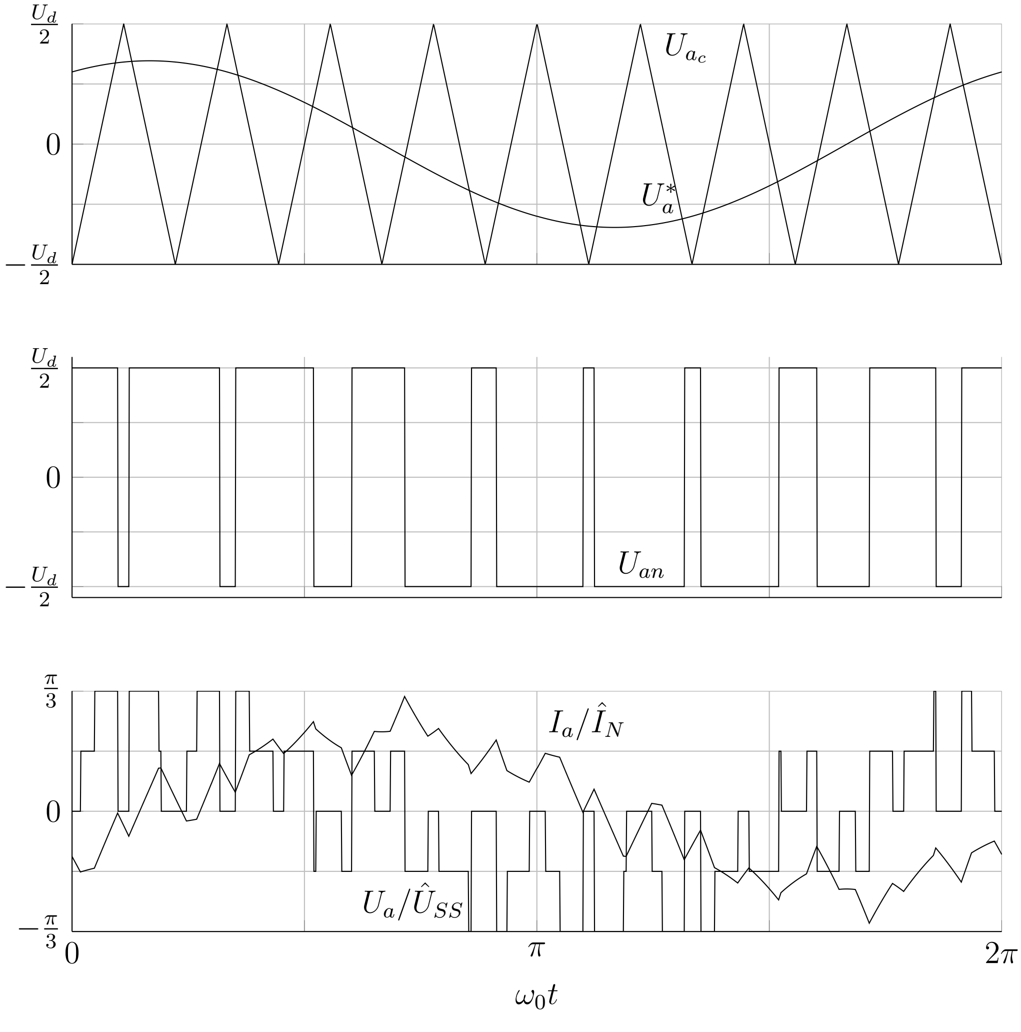

Figure 4.1: Waveforms of a triangle modulated sinusoidal phase voltage over one fundamental cycle. Top: triangle carrier signal U_{a_c} and reference voltage waveform U_a^* of phase a. Middle: phase leg voltage U_{an}. Bottom: phase voltage $U_a/\hat{U}_{SS}$ and current waveform $I_a/\hat{I}_N$ (per unit) of an inductive three-phase load.

frequency patterns. The latter type includes synchronous optimal modulation with optimal pulse pattern [22, 38, 55], the optimal subcycle method [54] and predictive control [57, 66]. Due to the variable frequency, theses schemes require an adaptive controller and on- or offline optimization, which increases complexity and computational intensity. Their application is therefore rare, mainly in the field of medium voltage drives [56].

Common modulation schemes are of fixed-frequency type, including carrier-based and direct digital techniques. Carrier-based pulse width modulation (PWM) techniques compare a carrier signal with a sinusoidal reference wave, as depicted in Figure 4.1. At the intersection a switching occurs, such that the desired inverter output waveform employs the “per-carrier cycle volt-second balance” principle [52]. Usually, a triangle carrier waveform is applied, offering a well-defined harmonic spectrum and simple implementation.

Direct digital techniques, such as space vector modulation (SVM), precalculate the on- and off-times of the switches, such that the volt-second balance for each switching cycle is achieved. Recalling the space vectors of the first sector in Figure 3.8, there are four vectors available for modulation: the zero vectors (000) and (111) as well as the active vectors (100) and (110). For three-phase loads with an isolated neutral point there is an extra degree of freedom for control: any sequence of zero voltage vectors can be injected to the output waveform since the potential of the star point can be freely varied.

The literature is rich in optimized SVM and PWM techniques addressing the proper on-time ratio of zero voltage states depending on the modulation index and angle of the reference vector [112, 46, 18]. Setting the ratio to one or zero, excludes a zero vector from the sequence. Those so called *discontinuous* schemes reduce the number of switches per cycle, such that the switching frequency can be increased. Those schemes stay in contrast to *continuous* schemes which include both zero vectors [71].

The following sections analyze the impact of the presented modulation techniques on the distortion of the converter output current. The double Fourier integral analysis of section 4.1 incorporates for calculation the method of sampling and also the pulse ratio. This analyzing technique is extensive and in the following only applied to PWM. It is preferably used for low switching frequencies.

For high pulse ratios further simplifications can be assumed, which reduce the complexity greatly and lead to the harmonic flux analysis as showed in section 4.2. This method of analysis is suitable for any type of modulation method, including SVM.

4.1 Double Fourier Integral Analysis

The widely known “Double Fourier Integral Analysis” is an analytical method for estimating the harmonic components of a pulsewidth modulated waveform. It was introduced with Bowes and Bird [17], who adapted the approach of Bennet [10] and Black [58], which was originally developed for communication systems.

The following short overview of the analyzing technique was mainly abstracted from [52]. For further studies, the interested reader may be referred to this book, which extensively elaborates pulsewidth modulation techniques for state of the art power converters.

The analysis process assumes two different time-dependent variables

$$\begin{aligned} x(t) &= \omega_c t + \Theta_c \text{ and} \\ y(t) &= \omega_0 t + \Theta_0, \end{aligned}$$

where ω_c and ω_0 are the angular frequencies ($\omega_0 < \omega_c$). Θ_c and Θ_0 are the arbitrary phase offset angles for the carrier and fundamental waveform respectively.

The variables represents the high and low frequency harmonic content of the output waveform. Each of the variables can be seen as independently periodic towards its period, i.e. $T_c = 2\pi/\omega_c$ for $x(t)$ and $T_0 = 2\pi/\omega_0$ for $y(t)$.

The output of each inverter leg can then be expressed as a function dependent on the cyclically varied $x(t)$ and $y(t)$, i.e. $f(t) = [x(t), y(t)]$. In Figure 4.2, the output voltage is depicted in a unit cell as a contour region depending on $x(t)$ and $y(t)$ with two different voltage levels: 0 and U_d. The shape of the topological form is defined by the reference waveform in y-direction and by the carrier waveform in x-direction. Both axes are scaled in radians, reflecting the carrier and fundamental reference frequencies and span from $-\pi$ to $+\pi$.

The output function $f(t) = [x(t), y(t)]$ is then an infinite periodic signal in both directions towards one or multiples of such interconnected unit cells, as shown in Figure 4.3. From the Fourier Series theory [72] any time varying periodic function $f(t)$ can be written as a sum of harmonic components:

$$\begin{aligned} f(t) &= \frac{a_0}{2} + \sum_{m=1}^{\infty} [a_m \cos(m\omega t) + b_m \sin(m\omega t)], \text{ where} \qquad (4.1) \\ a_m &= \frac{1}{\pi} \int_{-\pi}^{\pi} f(t)\ \cos(m\omega t)\ d\omega t \\ b_m &= \frac{1}{\pi} \int_{-\pi}^{\pi} f(t)\ \sin(m\omega t)\ d\omega t, \text{ with } m = 0, 1, \ldots, \infty \end{aligned}$$

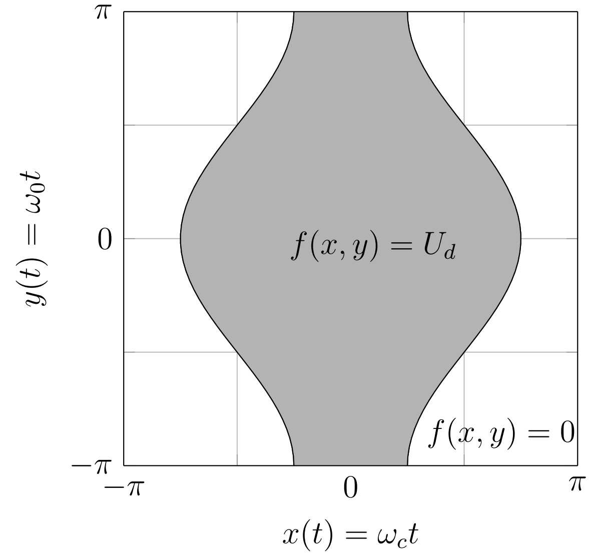

Figure 4.2: Unit cell for triangular carrier modulation and sinusoidal reference waveform.

For the two-dimensional case with the variables x and y, a similar construct can be achieved [52]:

$$\begin{aligned} f(x,y) = {} & \frac{A_{00}}{2} + \sum_{n=1}^{\infty} \left[A_{0n}\cos(ny) + B_{0n}\sin(ny) \right] && (4.2) \\ & + \sum_{m=1}^{\infty} \left[A_{m0}\cos(mx) + B_{m0}\sin(mx) \right] \\ & + \sum_{m=1}^{\infty} \underbrace{\sum_{n=-\infty}^{\infty}}_{n\neq 0} \left[A_{mn}\cos(mx+ny) + B_{mn}\sin(mx+ny) \right], \text{where} \end{aligned}$$

$$A_{mn} = \frac{1}{2\pi^2} \int_{-\pi}^{\pi} \int_{-\pi}^{\pi} f(x,y)\ \cos(mx+ny)\ dx\ dy \qquad (4.3)$$

$$B_{mn} = \frac{1}{2\pi^2} \int_{-\pi}^{\pi} \int_{-\pi}^{\pi} f(x,y)\ \sin(mx+ny)\ dx\ dy \qquad (4.4)$$

or in a time-varying form by substituting $x = \omega_c t + \Theta_c$ and $y = \omega_0 t + \Theta_0$:

$$\begin{aligned} f(x,y) = & \underbrace{\frac{A_{00}}{2}}_{\text{DC-Offset}} \\ & + \sum_{n=1}^{\infty} \underbrace{[A_{0n}\cos(n[\omega_0 t + \Theta_0]) + B_{0n}\sin(n[\omega_0 t + \Theta_0])]}_{\text{Fundamental Component \& Baseband Harmonics}} \\ & + \sum_{m=1}^{\infty} \underbrace{[A_{m0}\cos(m[\omega_c t + \Theta_c]) + B_{m0}\sin(m[\omega_c t + \Theta_c])]}_{\text{Carrier Harmonics}} \\ & + \sum_{m=1}^{\infty} \underbrace{\sum_{n=-\infty}^{\infty}}_{n\neq 0} \underbrace{\begin{bmatrix} A_{mn}\cos(m[\omega_c t + \Theta_c] + n[\omega_0 t + \Theta_0]) \\ +B_{mn}\sin(m[\omega_c t + \Theta_c] + n[\omega_0 t + \Theta_0]) \end{bmatrix}}_{\text{Sideband Harmonics}} \end{aligned} \tag{4.5}$$

with the carrier index variable $m \in [0, 1, \ldots, \infty]$ and $n \in [-\infty, \ldots, \infty]$ as the baseband index variable.

The frequency of a certain harmonic component ω_h is calculated with both index variables in the form $\omega_h = m\ \omega_c + n\ \omega_0$. The magnitudes at this harmonic frequency are thus a sum of all harmonic magnitudes fulfilling the equation for ω_h.

For the special cases $m = 0$ (where n exhibits arbitrary values) and $n = 0$ (where m exhibits arbitrary values) the summation groups of equation (4.5) are named as fundamental, baseband, and carrier harmonics. The fundamental component is achieved for $n = 1$, which reflects the desired output. Its value should be as high as possible. The baseband harmonics represent undesired low-frequency voltages around the fundamental component. Their magnitudes should be minimized or even eliminated by choosing a proper modulation scheme.

In contrast, the carrier harmonics in contrast appear at a relatively high frequency level (a multiple of the carrier signal). Sideband harmonics exist as an ensemble of sums and differences of the modulating carrier waveform and the fundamental signal with its associated baseband harmonics. Their magnitudes are centered in groups around the carrier harmonic frequencies.

The A_{mn} and B_{mn} coefficients of equation (4.5) represent the magnitudes of the harmonics. Their values must be estimated for a certain modulation method and any combination of m and n. The solution for the coefficients can be gained either from equations (4.3) and (4.4) or in a compact and complex form:

$$A_{mn} + jB_{mn} = \frac{1}{2\pi^2} \int_{-\pi}^{\pi} \int_{-\pi}^{\pi} f(x,y)\ e^{j(mx+ny)}\ dx\ dy \tag{4.6}$$

4.1.1 Sampling Techniques for Carrier Based Modulation

Carrier-based modulation is widely used for electric power converters. In such a strategy, the reference signal is compared with a carrier waveform. The two signals may have any shape, although it is important for the carrier to have a higher frequency than the reference. This work focuses on the commonly used sinusoidal reference (in order to imitate an AC voltage) and triangular carrier.

The purpose of any modulation technique is to produce the same volt-seconds of output as the desired reference value within a specified time frame. In the carrier-based method, the result is accomplished by switching between between inverter states whenever the carrier signal crosses the sinusoidal signal, with some variation in sampling which will be discussed. There are two switches per inverter leg, and depending on the switching state each leg may be connected to the higher ($+U_d/2$) or lower ($-U_d/2$) DC bus voltage level as seen in Figure 3.7. For simplicity reasons, the derivation of the distortion function assumes output voltages of 0 and $+U_d$, which represents the output voltages measured against the lower DC-Bus level.

In order to determine the switching state, the fundamental waveform must be sampled and compared to the carrier. This work examines three possible methods of sampling. The first, "natural sampling" (NS) compares the carrier and fundamental waveforms continuously within one interval. In contrast, the "symmetrical regular sampling" (SS) and "asymmetrical regular sampling" (AS) techniques sample and hold the fundamental wave value once (for SS) or twice (for AS) within a carrier cycle (see Figure 5.1). These sample and hold techniques are therefore more suitable to digital control systems [52].

In order to achieve a value for the harmonic amplitudes with equation (4.6) the inverter output waveform of Figure 4.3 must be further analyzed. The continuous slope crossing the unit cells defines the naturally modulated switch on and off angles. As seen there, $f(x, y)$ changes from 0 to U_d at:

$$x = 2\pi k - \left(\frac{\pi}{2} + \frac{\pi\hat{U}}{U_d}\cos(y)\right) \text{ and vice versa at} \tag{4.7}$$

$$x = 2\pi k + \left(\frac{\pi}{2} + \frac{\pi\hat{U}}{U_d}\cos(y)\right) \text{ with } k = 0, 1, 2, \ldots, \infty \text{ and} \tag{4.8}$$

where $\hat{U}$ is the amplitude of the fundamental wave.

Focusing on the first unit cell, i.e. $k = 0$ and including the modulation

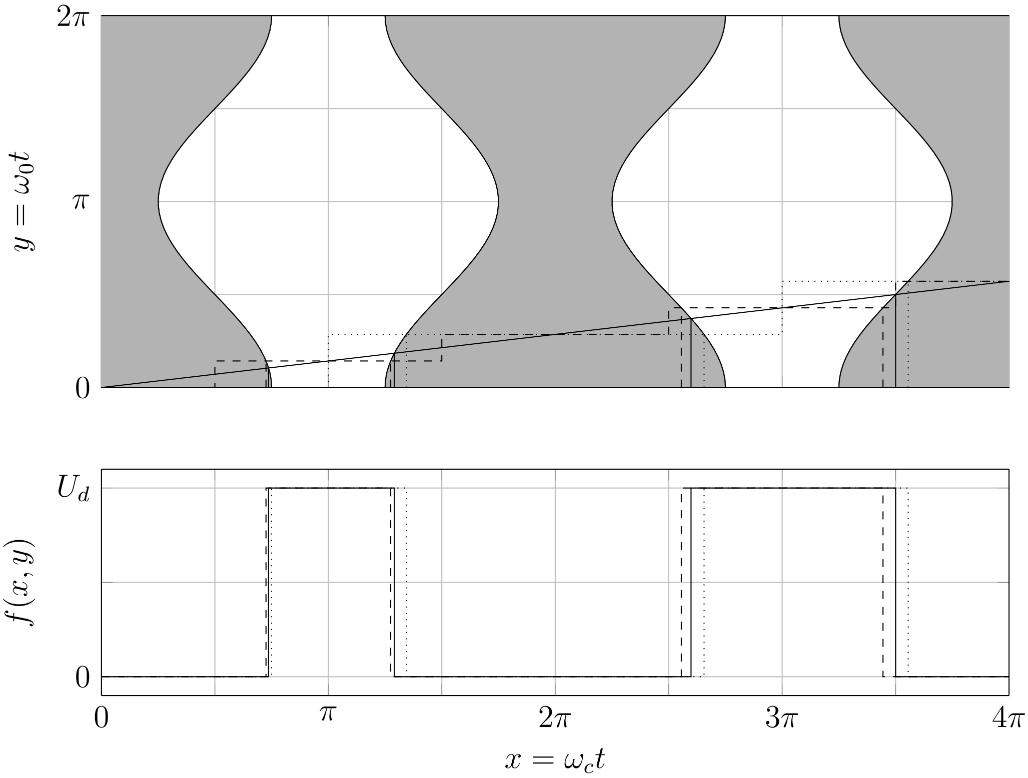

Figure 4.3: Triangular sampling of a sinusoidal reference waveform (top) and half-bridge output voltage measured against negative DC-Bus voltage (bottom). Continuous natural sampling (solid line), symmetrical regular sampling (dotted line), and asymmetrical regular sampling (dashed line) techniques.

index M of equation (3.44) simplifies both formulas to:

$$x = -\frac{\pi}{2} - 2\ M\cos(y) \tag{4.9}$$

$$x = +\frac{\pi}{2} + 2\ M\cos(y) \tag{4.10}$$

With the integration limits (4.9) and (4.10), the harmonic magnitudes of equation (4.6) can be calculated for any m and n by solving:

$$A_{mn} + jB_{mn} = \frac{1}{2\pi^2}\int_{-\pi}^{\pi}\int_{-\frac{\pi}{2}-2M\cos(y)}^{\frac{\pi}{2}+2M\cos(y)} U_d\ e^{j(mx+ny)}\ dx\ dy \tag{4.11}$$

After some calculations as done in [52] and a normalization with the six-step voltage $\hat{U}_{SS}$ from equation (3.43) the following statement can be achieved:

$$a_{mn} = \frac{A_{mn}}{\hat{U}_{SS}} = \frac{1}{m}J_n\left(2\ m\ M\right)\sin\left(\left[m+n\right]\frac{\pi}{2}\right) \tag{4.12}$$

where J_n is the n-th order Bessel function of the first kind. B_{mn} is computed to be zero for every modulation technique analyzed here.

Equation (4.12) expresses the normalized magnitudes for any combination of n and m. On its basis sideband harmonic amplitudes as well as carrier harmonics (with $n = 0$), fundamental, and baseband harmonics (with $m = 0$) are achieved.

As seen from (4.12) the magnitudes are weighted with the factor $1/m$. This weighting leads to reduced harmonic components as the carrier harmonic increases. The $\sin([m+n]\pi/2)$-term is zero for any even combination of $n+m$ and in this case, excludes the harmonic from the spectrum, as shown in Figure 4.4.

For the symmetrical sampling method, y of equation (4.11) must be substituted with the variable $y' = y - (\omega_0/\omega_c)x$, which defines the staircase function of the SS-trajectory with the continuous NS-trajectory along the cell units in Figure 4.3. It changes the formula to:

$$A_{mn} = \frac{1}{2\pi^2}\int_{-\pi}^{\pi}\int_{-\frac{\pi}{2}-2M\cos(y')}^{\frac{\pi}{2}+2M\cos(y')} U_d\ e^{j\left(\left[m+n\frac{\omega_0}{\omega_c}\right]x+ny'\right)}\ dx\ dy' \tag{4.13}$$

And after some calculation steps:

$$a_{mn} = \frac{A_{mn}}{\hat{U}_{SS}} = \frac{1}{m+\frac{n}{p}}J_n\left(2\ M\left[m+\frac{n}{p}\right]\right)\sin\left(\left[m+\frac{n}{p}+n\right]\frac{\pi}{2}\right) \tag{4.14}$$

where $p = \omega_c/\omega_0$ is the pulse ratio.

With the SS-technique the $\sin([m+n]\pi/2)$-term of equation (4.12) changes to $\sin([m + n/p + n]\pi/2)$. This characteristic does not lead to a elimination of components with an even $m + n$-combination for $p < \infty$. As shown in Figure 4.4 the components exist, but with a reduced magnitude.

The asymmetrical sampling technique needs to separate the integration term across the x-axis into two parts. The right part uses the staircase variable $y'_r = y - (\omega_0/\omega_c)[x + (\pi/2)]$, whereas for the left part it is $y'_l = y - (\omega_0/\omega_c)[x - (\pi/2)]$.

According to this approach, equation (4.11) then splits off and with the substitution of y it becomes:

$$\begin{aligned} A_{mn} = & \frac{1}{2\pi^2}\int_{-\pi}^{\pi}\int_{-\frac{\pi}{2}-2M\cos(y'_r)}^{0} U_d\ e^{j\left(mx+n\left[y'_r+\frac{\omega_0}{\omega_c}\left(x+\frac{\pi}{2}\right)\right]\right)}\ dx\ dy'_r \\ & + \frac{1}{2\pi^2}\int_{-\pi}^{\pi}\int_{0}^{\frac{\pi}{2}+2M\cos(y'_l)} U_d\ e^{j\left(mx+n\left[y'_l+\frac{\omega_0}{\omega_c}\left(x-\frac{\pi}{2}\right)\right]\right)}\ dx\ dy'_l \end{aligned} \tag{4.15}$$

And after some calculations:

$$a_{mn} = \frac{A_{mn}}{\hat{U}_{SS}} = \frac{1}{m+\frac{n}{p}} J_n\left(2\ M\left[m + \frac{n}{p}\right]\right)\sin\left([m+n]\frac{\pi}{2}\right) \tag{4.16}$$

In the following, the harmonic components of some characteristic combinations of m and n are analyzed. First, setting $m = n = 0$ into equations (4.12), (4.14), and (4.16) achieves the same offset value, i.e.:

$$a_{00} = \frac{\pi}{2} \tag{4.17}$$

The DC-offset voltage can be computed by setting $A_{00} = a_{00} \cdot \hat{U}_{SS} = U_d$ into (4.5), i.e.:

$$U_{DC} = \frac{U_d}{2} \tag{4.18}$$

Note that $f(x, y)$ was referred to the negative DC-Bus voltage level. Setting the neutral point n of the inverter as the reference magnitude (see Figure 3.7), the offset would be zero.

Second, the fundamental component and baseband harmonics are achieved by choosing $m = 0$. For the natural sampling technique, equation (4.12) simplifies with this assumption to:

$$a_{0n} = M \tag{4.19}$$

As seen from (4.19) the NS-technique offers a single low-frequency component, which turns out to be the fundamental magnitude M. Baseband harmonics do not exist for this scheme.

For the symmetrical sampling, setting $m = 0$ in (4.14) leads to:

$$a_{0n} = \frac{p}{n} J_n\left(\frac{2n}{p}M\right) \sin\left(\left[\frac{n}{p} + n\right]\frac{\pi}{2}\right) \tag{4.20}$$

Thus, for the SS-technique baseband harmonics exist and lead to unwanted distortions in the low frequency-range. In addition for $n = 1$, the fundamental amplitude is $a_{01} < M$ which implies less DC-voltage exploitation compared to the NS-technique.

For the asymmetrical sampling, baseband harmonics exist as well. With $m = 0$ equation (4.16) becomes:

$$a_{0n} = \frac{p}{n} J_n\left(\frac{2n}{p}M\right) \sin\left(n\frac{\pi}{2}\right) \tag{4.21}$$

As seen from the equation, baseband harmonics exist but only for odd values of n. The fundamental component is also lower than the modulation index. The difference, however, is much smaller than for the NS-scheme.

Figure 4.4 shows the normalized components of a modulated waveform for the three sampling techniques. As seen there, the NS scheme does not produce any baseband harmonics at low frequencies, wheres both other techniques do. Since the $\sin([m + n/p + n]\pi/2)$-term of equation (4.14) is not necessarily zero for even combination of $m + n$ and finite pulse ratios, there exist odd sideband harmonics around the odd carrier multiples and even sideband harmonics around the even carrier multiples.

For the single-phase case the three sampling techniques lead to nearly equal distortion values (WTHD), which changes significantly if more phases are under consideration (see Section 5.1).

4.1.2 Two-Level Pulse Width-Modulated Waveform

The voltage waveforms of a single two-level VSI leg can be expressed on the basis of the normalized amplitudes for the fundamental component and baseband harmonics a_{0n} and for the carrier as well as sideband harmonics a_{mn}. Since the output waveform is refered to the inverter's neutral point n, the DC-offset value is zero and a_{00} can be neglected.

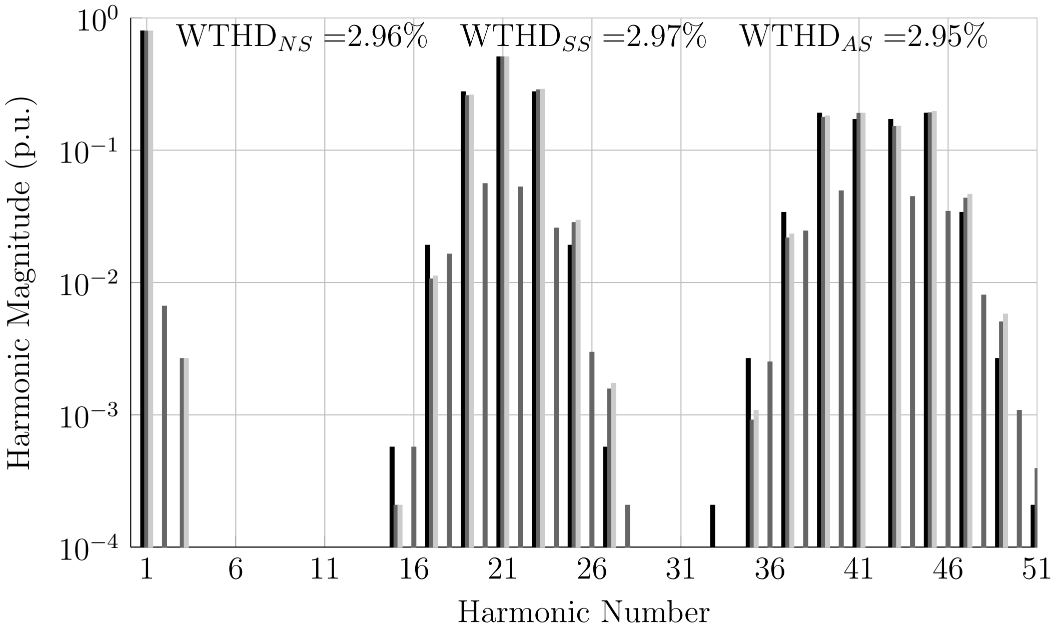

Figure 4.4: Harmonic spectrum of one inverter leg voltage waveform with natural (black), symmetrical (anthracite-gray), and asymmetrical (gray) sampled reference ($M = 0.78$, $p = 21$)

In general, the waveform is [52]

$$\begin{aligned} u(t) = &\sum_{n=1}^{\infty} \underbrace{a_{0n}\ \cos\left(n\left[\omega_0 t + \Theta_0\right]\right)}_{\text{Fundamental Component \& Baseband Harmonics}} \\ &+ \sum_{m=1}^{\infty}\sum_{n=-\infty}^{\infty} \underbrace{a_{mn}\ \cos\left(m\left[\omega_c t + \Theta_c\right] + n\left[\omega_0 t + \Theta_0\right]\right)}_{\text{Carrier \& Sideband Harmonics}} \end{aligned} \tag{4.22}$$

Where the parameters ω_0 and Θ_0 represent the frequency and phase offset angle of the fundamental waveform, while ω_c and Θ_c are the frequency and phase offset angle of the carrier waveform. Note that (4.23) is separated into a fundamental and non-fundamental component. The non-fundamental component represents the distortion due to unwanted carrier and sideband harmonics. This term is expressed as a double summation over the carrier- and baseband index variables (m and n).

With the results of Section 4.1.1 the output voltage equation for the NS technique therefore becomes

$$\begin{aligned} u(t) &= M\cos(\omega_0 t + \Theta_0) \\ &\quad + \sum_{m=1}^{\infty} \sum_{n=-\infty}^{\infty} \frac{1}{m} J_n\left(2mM\right) \sin\left(\left[m+n\right]\frac{\pi}{2}\right) \\ &\quad \times \cos\left(m\left[\omega_c t + \Theta_c\right] + n\left[\omega_0 t + \Theta_0\right]\right) \end{aligned} \tag{4.23}$$

With the pulse ratio $p = \omega_c/\omega_0$, the output of an inverter leg using the SS method can be expressed in a similar form, but in contrast this version includes baseband harmonics as derived in Section 4.1.1:

$$\begin{aligned} u(t) &= \sum_{n=1}^{\infty} \frac{p}{n} J_n\left(2M\frac{n}{p}\right) \sin\left(\left[\frac{n}{p}+n\right]\frac{\pi}{2}\right) \cos(n\left[\omega_0 t + \Theta_0\right]) \\ &\quad + \sum_{m=1}^{\infty} \sum_{n=-\infty}^{\infty} \frac{1}{m+\frac{n}{p}} J_n\left(2\ M\left[m+\frac{n}{p}\right]\right) \sin\left(\left[m+\frac{n}{p}+n\right]\frac{\pi}{2}\right) \\ &\quad \times \cos\left(m\left[\omega_c t + \Theta_c\right] + n\left[\omega_0 t + \Theta_0\right]\right) \end{aligned} \tag{4.24}$$

Finally, the inverter leg output voltage of the AS fundamental waveform can be expressed as follows:

$$\begin{aligned} u(t) &= \sum_{n=1}^{\infty} \frac{p}{n} J_n\left(2M\frac{n}{p}\right) \sin\left(n\frac{\pi}{2}\right) \cos(n\left[\omega_0 t + \Theta_0\right]) \\ &\quad + \sum_{m=1}^{\infty} \sum_{n=-\infty}^{\infty} \frac{1}{m+\frac{n}{p}} J_n\left(2M\left[m+\frac{n}{p}\right]\right) \sin\left(\left[m+n\right]\frac{\pi}{2}\right) \\ &\quad \times \cos\left(m\left[\omega_c t + \Theta_c\right] + n\left[\omega_0 t + \Theta_0\right]\right) \end{aligned} \tag{4.25}$$

Note that the waveforms here are normalized with the maximum fundamental phase voltage in six-step mode (see equation (3.43)). In order to achieve absolute values a multiplication with $\hat{U}_{SS}$ is necessary, i.e. $U(t) = \hat{U}_{SS} \cdot u(t)$.

4.1.3 Weighted Total Harmonic Distortion

The weighted total harmonic distortion factor (WTHD) represents the ohmic losses caused by modulation for a load modeled as predominantly inductive, with a very small but nontrivial resistance. The WTHD factor is defined as the root mean square, or rms, value of all harmonic voltage amplitudes U_f normalized with their frequency f and fundamental amplitude at $M = 1$ [84]. Because there is no DC component and negative frequencies can be neglected, the WTHD is defined as follows:

$$\mathrm{WTHD} = \sqrt{\sum_{f=2}^{\infty} \left(\frac{U_f}{f}\right)^2} \quad \text{with } f = m \cdot p + n \tag{4.26}$$

As seen in equation (4.26), a certain voltage amplitude U_f at frequency f can be obtained for various combinations of the carrier and baseband index variables m and n. Therefore, when searching for an exact solution of U_f, the voltage amplitudes and phase angles of these combinations must be considered. For a pulse ratio $p > 5$, however, U_f is predominantly determined by one combination in particular. This leads to an estimation of U_f as the square sum of all voltage amplitudes $\hat{U}(m, n)$, which satisfies the condition for f explained earlier. The WTHD factor can therefore be approximated as:

$$\mathrm{WTHD} \approx \sqrt{\sum_{m=0}^{\infty} \sum_{n=-\infty}^{\infty} \left(\frac{\hat{U}(m,n)}{mp+n}\right)^2} \quad \text{with } m \cdot p + n > 1 \tag{4.27}$$

4.2 Harmonic Flux Analysis

As demonstrated in section 4.1, the baseband or subcarrier harmonics reduce with increasing pulse ratios. For values of ($p > 20$) they can even be neglected [53]. Since modern switching devices such as MOSFETs and IGBTs in general meet this criterion, the distortion of the current waveform is mainly determined by harmonics with frequencies ($f \geq p$).

The harmonic flux analysis is based on the assumption that the extra copper losses due to high frequency harmonics can be determined first by an estimation of the distortions during a switching cycle (microscopic view). Second, a macroscopic investigation is necessary to sum up the individual results properly and achieve an overall distortion value over one fundamental cycle.

With the vector space approach of [2, 70] an intuitive analyzing tool is given and explained here for the common three-phase case. As will be shown in Section 6, it is easy to extend for the symmetrical six-phase drive.

4.2.1 Voltage Equations

The basis of the analytic approach is the first sector of the hexagon in Figure 3.8. The sector is formed by the voltage space vectors $\vec{v}_0$, $\vec{v}_1$, $\vec{v}_2$, and $\vec{v}_7$ with the switching states (000), (110), (100), and (111) respectively. In order to produce the same volt-seconds as the reference vector $\vec{v}^*$ over the sampling time T_s, the aforementioned vectors must be applied with on times t_0, t_1, t_2, and t_7 such that

$$\sum_k \vec{v}_k t_k = \vec{v}^* T_s, \text{ with } k \in \{0, 1, 2, 7\} \tag{4.28}$$

The switching sequence over one sampling period is selected as 0-1-2-7-7-2-1-0 for the first sector. Since the sequence is symmetric and the on-times for the first half-cycle are assumed equal to the second one, only one half period needs to be evaluated. Introducing the duty cycle $d_k = 2t_k/T_s$ as the relative on-time of the k-th inverter output vector v_k over one half-cycle, the following relation holds:

$$\sum_k \vec{v}_k d_k = \vec{v}^*, \text{ where } 0 \leq d_k \leq 1 \text{ and } \sum_k d_k = 1 \tag{4.29}$$

The duty cycles of the different voltage vectors d_1, d_2, and $d_0 + d_7$ have to fulfill the following linear equation to meet the requirements of (4.29):

$$\begin{bmatrix} \frac{\pi}{6} & \frac{\pi}{3} & 0 \\ \frac{\pi}{2\sqrt{3}} & 0 & 0 \\ 1 & 1 & 1 \end{bmatrix} \begin{bmatrix} d_1 \\ d_2 \\ d_0 + d_7 \end{bmatrix} = \begin{bmatrix} M\cos(\Theta) \\ M\sin(\Theta) \\ 1 \end{bmatrix} \tag{4.30}$$

As seen from equation (4.30) there is one degree of freedom for optimization: the ratio d_7/d_0 can be freely chosen. There exist a variety of different modulation schemes taking advantage of this characteristic by injecting a proper zero-sequence to reduce current distortions [18, 46, 112].

4.2.2 Harmonic Flux Trajectories

The current distortion during a switching cycle is expressed with the time integral of the harmonic voltage vectors $\vec{v}_h$. The resulting harmonic flux vector $\vec{\lambda}_h$ consists of fictitious per unit machine states, which are defined as:

$$\vec{\lambda}_h = \int_0^1 \vec{v}_h \; dd = \int_0^1 \vec{v}_k - \vec{v}^* \; dd \tag{4.31}$$

With $p > 20$ the reference voltage vector $\vec{v}^*$ can be assumed as constant during a switching cycle. This assumption leads to a linear trajectory of $\vec{\lambda}_h(d)$ in the $\alpha\beta$-space with zero as the initial and final value. As depicted in Figure 4.5, the trajectory forms a triangle within the first half-cycle and the

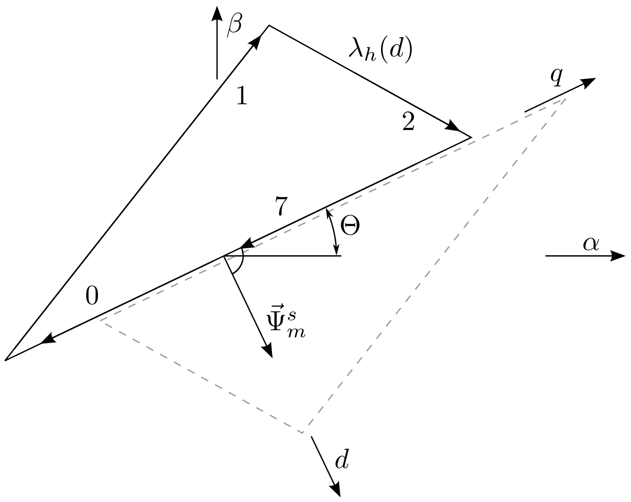

Figure 4.5: Harmonic flux trajectory $\vec{\lambda}_h(d)$ during first half-cycle (solid line) with switching sequence 0-1-2-7 and in symmetry the second half cycle (dashed line) with sequence 7-2-1-0. The flux oriented dq-coordinate system is rotated by the angle Θ in reference to the the stator fixed $\alpha\beta$-system.

same shape, point symmetrical towards origin, within the second half-cycle.

For any combination of M and Θ there exist a unique trajectory of $\vec{\lambda}_h$. But due to the sixfold symmetry of the inverter hexagon only one segment has to be analyzed. For the first sector, $\vec{\lambda}_h(d)$ can be expressed in closed form analytically [51]:

$$\vec{\lambda}_h(d) = \begin{cases} \begin{bmatrix} -d \cdot M\cos(\Theta) \\ -d \cdot M\sin(\Theta) \end{bmatrix} & \text{for: } 0 \le d < d_0 \\[2ex] \begin{bmatrix} -d \cdot M\cos(\Theta) + \frac{\pi}{6}(d - d_0) \\ -d \cdot M\sin(\Theta) + \frac{\pi}{2\sqrt{3}}(d - d_0) \end{bmatrix} & \text{for: } d_0 \le d < d_0 + d_1 \\[2ex] \begin{bmatrix} -d \cdot M\cos(\Theta) + \frac{\pi}{6}(2d - d_1 - 2d_0) \\ -d \cdot M\sin(\Theta) + \frac{\pi}{2\sqrt{3}}d_1 \end{bmatrix} & \text{for: } d_0 + d_1 \le d < 1 - d_7 \\[2ex] \begin{bmatrix} -d \cdot M\cos(\Theta) + \frac{\pi}{6}(d_1 + 2d_2) \\ -d \cdot M\sin(\Theta) + \frac{\pi}{2\sqrt{3}}d_1 \end{bmatrix} & \text{for: } 1 - d_7 \le d \le 1 \end{cases} \tag{4.32}$$

For different angular positions and modulation indices the trajectories of

$\vec{\lambda}_h(d)$ are depicted in Figure 4.6 for the first half of a carrier cycle. The standard SVM and the sinus-triangle PWM are considered there. The first method sets $d_7/d_0 = 1$, while the second uses: $d_7 = \frac{1}{2} - \frac{2M}{\pi}\cos(\Theta)$.

As seen in the figure, for $\Theta = 0$ and $\Theta = \frac{\pi}{3}$ the harmonic flux draws a line in the $\alpha\beta$-space, which corresponds to the fact that at the beginning or the end of a sector only one active vector is needed. The second one is set to zero. Comparing both modulation methods, the length of the lines are equal for a certain modulation index. For higher values however, the $\vec{\lambda}_h(d)$-trajectory of the PWM scheme is shifted away from zero, whereas the trajectory of the SVM scheme is centered towards origin. This fact leads to a greater distortion content of the PWM method for the angles mentioned above. For Θ-values becoming closer to $\pi/6$, the triangle-shaped trajectories of both schemes converge in size and position leading to equal distortions.

4.2.3 Harmonic Flux Distortion

For a better comparison, the energy or distortion content of the harmonic flux trajectory is expressed in a number, the root-mean-square (rms)-value [51]:

$$\lambda_{rms}^2\left(M,\Theta\right) = \int_0^1 \vec{\lambda}_h^T \cdot \vec{\lambda}_h \; dd \tag{4.33}$$

According to equation (4.33) the λ_{rms}^2-value depends on the distance from the harmonic flux trajectory to the origin. Consequently for $\Theta = 0$ and $\Theta = \pi/3$ the differences are significant as shwon in Figure 4.7a. For $\Theta = \pi/6$, however, the rms-values of both schemes are equal. The figure indicates the SVM method has lower harmonic distortion than the PWM method, and the difference is more pronounced for higher M values.

Figure 4.7a clearly illustrates the strong space dependency of the per-carrier cycle rms harmonic distortion characteristics of the two methods. A performance gain can be achieved by modulating the carrier frequency . By increasing the frequency at high-rms harmonic flux intervals and reducing it at low rms flux intervals, the overall distortion can be reduced [56].

The most important performance criterion of a modulator is the per fundamental cycle rms value λ_{frms}^2. Due to the sixfold symmetry, only one 60°-segment hast to be evaluated:

$$\lambda_{frms}^2 = \frac{3}{\pi}\int_0^{\pi/3} \lambda_{rms}^2 d\Theta \tag{4.34}$$

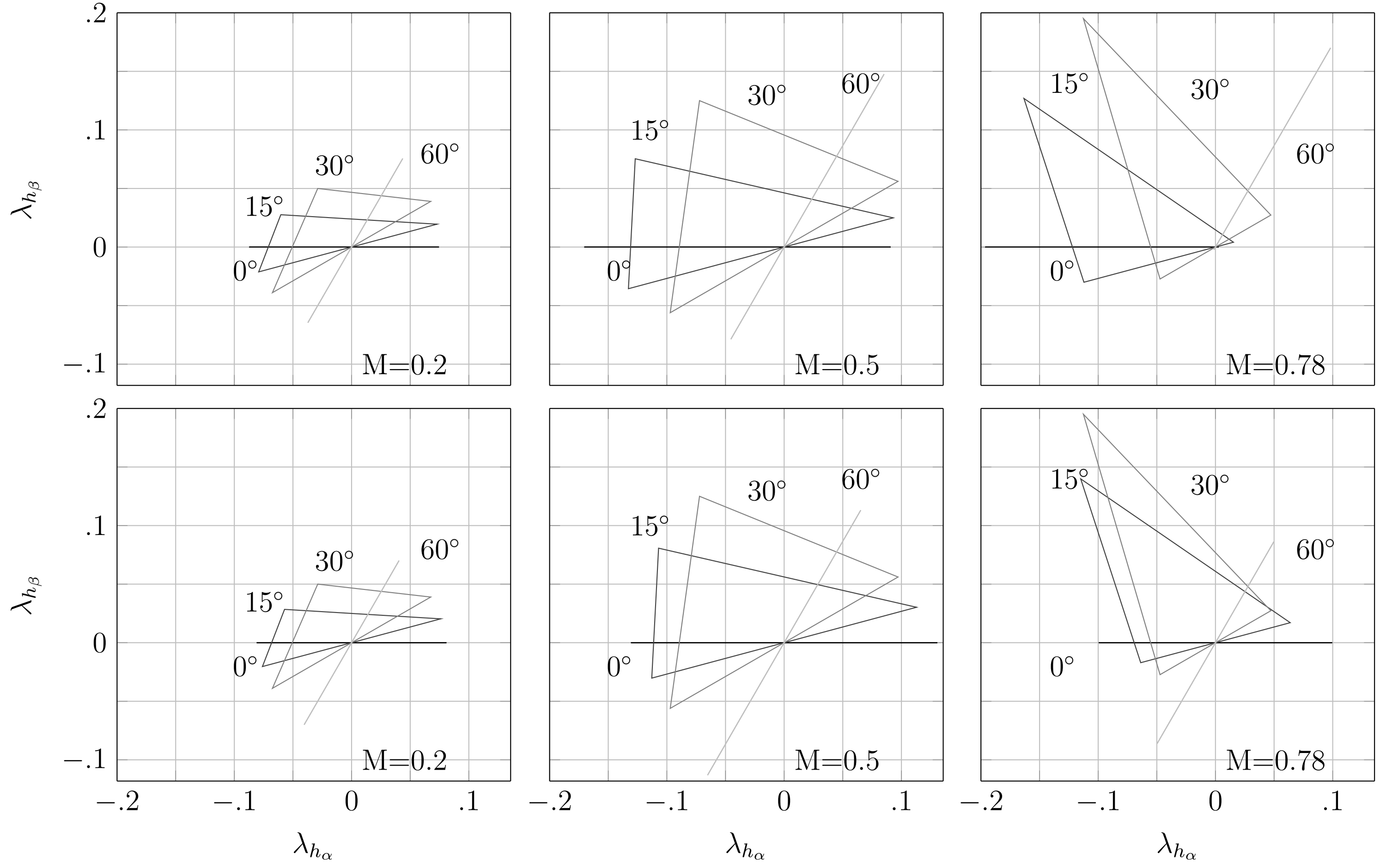

Figure 4.6: Trajectories of $\vec{\lambda}_h(d)$ within the first half-cycle in the $\alpha\beta$-subspace for different modulation indices M and angles Θ. Top row: sinus-triangular modulation. Bottom row: standard SVM.

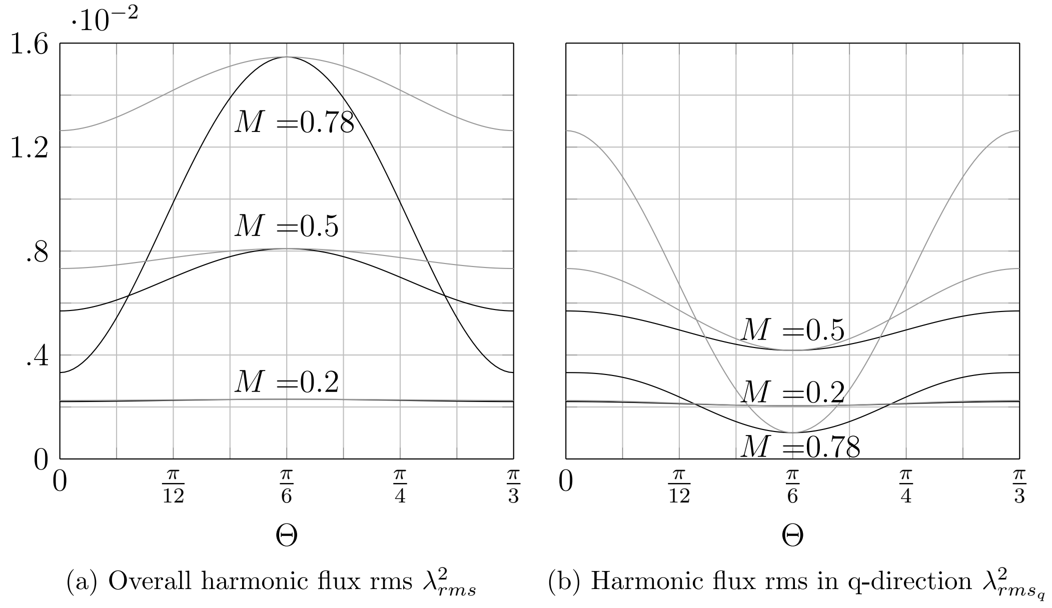

(a) Overall harmonic flux rms λ^2_{rms} (b) Harmonic flux rms in q-direction $\lambda^2_{rms_q}$

Figure 4.7: Harmonic flux rms for several modulation indices. Comparison of the sinus triangle PWM (gray) and the standard SVM (black).

The corresponding harmonic distortion function (HDF) is defined as [56]:

$$\mathrm{HDF} = \frac{288}{\pi^2}\lambda^2_{frms} \tag{4.35}$$

The HDF-curves for the three-phase sinus-triangle PWM and the SVM scheme are depicted in Figure 4.8. In the low modulation range, the two methods show nearly equal behavior. As the modulation index increases, the PWM performance rapidly degrades towards SVM, as expected.

It is shown in the following chapters 5 and 6, that the six-phase drive offers more degrees of freedom for control. This fact leads to various different modulation schemes. A variation of the three-phase PWM scheme is named the "*approximated interleaved modulation PWM*" as explained in section 5.3.3. Its HDF-characteristic is marked in Figure 4.8 as PWM_6. As seen there, the maximum performance gain achievable by this strategy is significant compared to the three-phase scheme. A modification of the common SVM is shown in section 6.4.2, named "*fragmented sector mapping*". The strategy offers even lower distortions and a higher exploitation of the DC-voltage, as seen in Figure 4.8 (SVM_6).

In Section 4.1 the WTHD was introduced as a performance factor. The factor is based on the inverter voltage waveform with an finite number of switches per fundamental cycle, whereas the HDF is derived here from a virtual harmonic flux path assuming the capability of applying very high

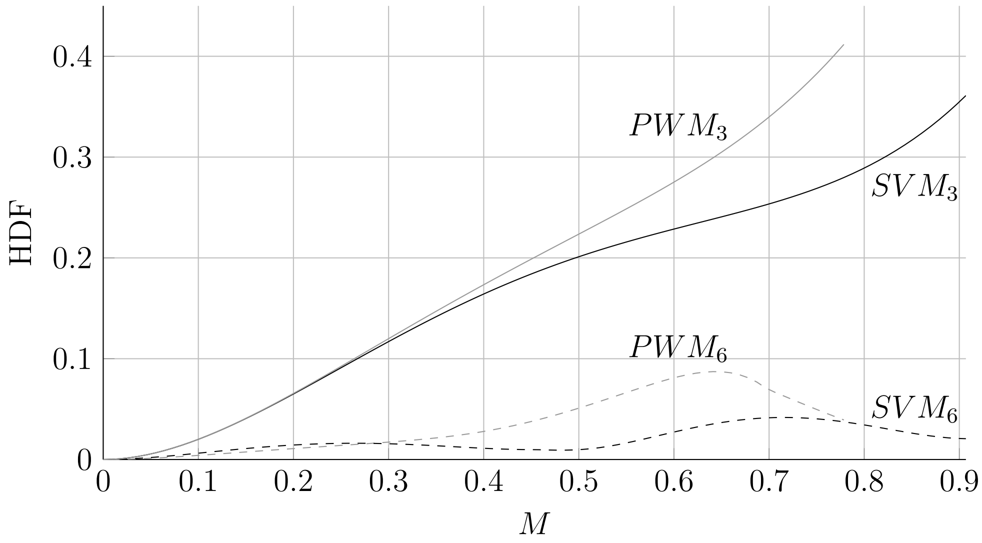

Figure 4.8: HDF characteristics of the three-phase sinus-triangle (PWM_3) and space vector (SVM_3) modulation. The six-phase modulation schemes: approximated interleaved (PWM_6) and fragmented sector mapping (SVM_6).

switching frequencies. Both factors express current distortion independently of the DC-Bus voltage and load inductance.

In [52] the relationship between HDF and WTHD is readily derived, resulting in the formula:

$$\text{WTHD} = \frac{\pi}{p}\sqrt{\frac{\text{HDF}}{18}} \tag{4.36}$$

It has to be noted the the equation above becomes less exact as the pulse ratio p is reduced, since the HDF was derived assuming a constant EMF during a switching cycle.

4.2.4 Harmonic Current

During experimental tests, the phase current is measured directly and its high-frequency rms content is represented through the harmonic current I_h. The factor is used for experimental results as a figure of merit for evaluation. Its value can be expressed as a square sum of current amplitudes $\hat{I}_f$ over a range of frequencies [84]:

$$I_h = \sqrt{\sum_{f=f_l}^{f_u} \hat{I}_f^2} \tag{4.37}$$

The lower frequency f_l is chosen such that any current harmonic caused by the specific machine design does not count towards I_h. The upper frequency is chosen as high as possible, determined by the sampling frequency of the measurement equipment. The current amplitudes $\hat{I}_f$ at a certain frequency are achieved with a Fast-Fourier transformation of the phase current over the predefined time-line [19]. In [52] a relation between the rms phase current distortion I_h^2 and the HDF is given with:

$$I_h^2 = \frac{1}{12}\left(\frac{U_d}{L_\sigma f_c \pi}\right)^2 \cdot \mathrm{HDF} \tag{4.38}$$

Combining equations (4.36) with (4.38) leads to the relationsship between WTHD and I_h^2:

$$I_h^2 = 27\left(\frac{U_d\, p}{L_\sigma f_c \pi^2}\right)^2 \cdot \mathrm{WTHD}^2 \tag{4.39}$$

4.2.5 Torque Ripple

With the definition of a mutual flux-oriented dq-coordinate system as shown in Figure 4.5, the machine torque can be expressed as the multiplication of mutual flux amplitude and q-component of stator current [103]. If the deviation of torque caused by the current distortions is of interest, the dq-representation of the harmonic flux $\lambda_h(d)$ is hence necessary. The components are achieved with the transformation $\mathbf{T}_\Theta$, i.e.:

$$\begin{bmatrix} \lambda_{h_d} \\ \lambda_{h_q} \end{bmatrix} = \underbrace{\begin{bmatrix} \sin(\Theta) & -\cos(\Theta) \\ \cos(\Theta) & \sin(\Theta) \end{bmatrix}}_{\mathbf{T}_\Theta} \cdot \begin{bmatrix} \lambda_{h_\alpha} \\ \lambda_{h_\beta} \end{bmatrix} \tag{4.40}$$

Assuming constant mutual flux, the q-term of the harmonic flux $\lambda_{h_q}(d)$ must therefore be proportional to the torque ripples. In order to achieve equal energy content, the following equation of rms-flux must hold true:

$$\lambda_{rms}^2 = \lambda_{rms_\alpha}^2 + \lambda_{rms_\beta}^2 = \lambda_{rms_d}^2 + \lambda_{rms_q}^2 \tag{4.41}$$

The $\lambda_{rms_q}^2$-values over Θ are presented in Figure 4.7b. Compared with the overall rms in Figure 4.7a, both curves start and end at $\Theta = 0$ and $\Theta = \pi/3$ with the same value for a certain modulation index M. This relationship is explained with the $\lambda_h(d)$-trajectories for those angles in Figure 4.6. They are lying in the q-direction only, leading to $\lambda_{rms_d}^2 = 0$.

Generally it can be stated that $\lambda^2_{rms_q}$ is determined by the extent of $\lambda_h(d)$ in the q-direction, which in turn depends on the modulation index and the relative on-time of zero vectors. Therefore, a minimum of $\lambda^2_{rms_q}$ at $\Theta = \pi/6$ for a certain M exists, since d_0 and d_7 are low compared to the start or end point.

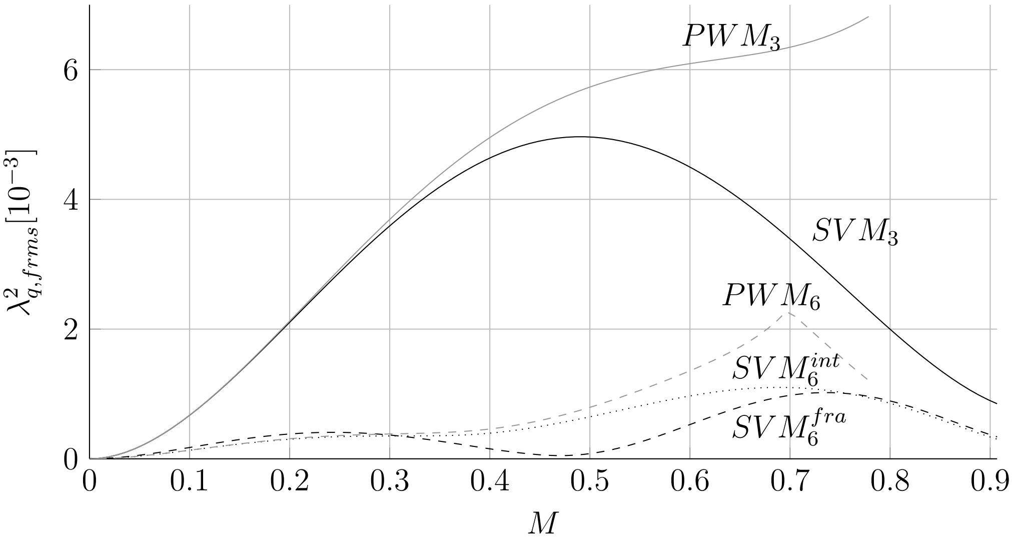

Figure 4.9: Harmonic flux rms in q-direction over a fundamental cycle. Comparison of sinus-triangle carrier and space vector modulation for three-phase drives (PWM_3, SVM_3) as well as interleaved PWM and SVM (PWM_6, SVM_6^{int}) with fragmented sector mapping (SVM_6^{frag}) for six-phase systems.

Similar to equation (4.34) the rms-magnitude of the q-component over one fundamental cycle is calculated. Its characteristic over M is depicted in Figure 4.9 for various modulation strategies. As seen there, the PWM-scheme shows a monotonically increasing trend, whereas the SVM-technique presents a maximum at around $M = 0.5$ and, comparing both curves, a superior performance. The PWM-scheme mainly suffers from the non-centered λ_h-trajectories at the beginning and the end of each segment, even at high modulation indices.

The diagram also includes the trajectories of the interleaved PWM- and SVM-schemes and the fragmented sector mapping modulation for six-phase drives. Those techniques are explained in detail in Sections 5 and 6.

Chapter 5

Carrier Based Pulsewidth Modulation

For the common three-phase inverter topology, the three carrier waveforms of a triangle modulated sinusoidal reference are usually in phase with each other. With the given six-phase drive of Figure 3.7, an additional degree of freedom becomes available: the phase offset angle Θ_c (see Figure 5.1), which is the phase shift between the carrier signals of phases (a, b, c) and (x, y, z).

In the following, the influence of the carrier phase shift angle on the current distortions of a symmetrical six-phase drive is evaluated based on the double Fourier integral analysis of Section 4.1. Therefore, in the subsequent Section 5.1, the voltage waveforms between two phases of the same three-phase set are calculated. Based on the waveform parameters the current distortions expressed through the weighted total harmonic distortion factor (WTHD) are derived in Section 5.2 for different sampling techniques.

It can be shown in Section 5.3 that there exists an angle Θ_c which minimizes the overall distortion factor depending on the modulation index as well as the pulse and inductance ratio. Simulation results are given, demonstrating the aforementioned statements. The theoretical considerations are validated by experiments in Section 5.4.

5.1 Line-to-Line Voltage Waveforms

Due to the symmetry of the three-phase systems, to estimate distortions only one line-to-line voltage of each EC shown in Figure 3.6 must be considered. These linked voltages of the two ECs are defined as U_{ab_1} and U_{ab_2}. According

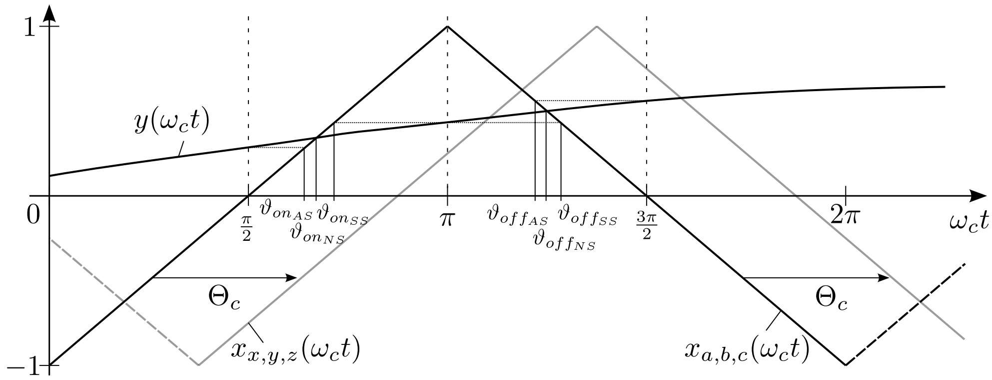

Figure 5.1: The triangle carrier waveforms $x_{a,b,c}$ and $x_{x,y,z}$ of the three-phase sets are shifted by the phase offset angle Θ_c. The output voltage of a leg changes each time the sampled fundamental voltage reference $y(\omega_c t)$ intersects the carrier signal, i.e. from high to low at angle ϑ_{on} and vice versa at ϑ_{off}. Switch pulse on and off angles for the naturally sampled (NS), symmetrically (SS) and asymmetrically regular sampled (AS) fundamental waveform (phase delay compensated) [40].

to equation (3.12) these are:

$$U_{ab_1} = U_{an_1} - U_{bn_1} = \frac{1}{2}\left(U_{an} - U_{xn} - U_{bn} + U_{yn}\right) \tag{5.1}$$

$$U_{ab_2} = U_{an_2} - U_{bn_2} = \frac{1}{2}\left(U_{an} + U_{xn} - U_{bn} - U_{yn}\right) \tag{5.2}$$

Therefore, the inverter leg voltages of phases a, b, x, y over one fundamental cycle have to be evaluated. As known from Section 4.1.1 the voltage waveforms are defined by a carrier and a fundamental phase offset angle (Θ_c and Θ_0).

For the four considered phases, the carrier phase offset angles are chosen as illustrated in Figure 5.1:

$$\Theta_{c_a} = \Theta_{c_b} = 0 \quad \Theta_{c_x} = \Theta_{c_y} = \Theta_c \tag{5.3}$$

The fundamental component of the inverter leg voltage is defined by Θ_0. If the antiparallel mode or operation in the first subspace is considered, the offset angles are:

$$\Theta_{0_a} = 0 \quad \Theta_{0_b} = -2\pi/3 \quad \Theta_{0_x} = -\pi \quad \Theta_{0_y} = -5\pi/3 \tag{5.4}$$

However, in parallel mode or operation in the second subspace the offset angles double:

$$\Theta_{0_a} = 0 \quad \Theta_{0_b} = -4\pi/3 \quad \Theta_{0_x} = 0 \quad \Theta_{0_y} = -4\pi/3 \tag{5.5}$$

For the operation in subspace two, the phase voltages u_{an}, u_{xn}, u_{bn}, and u_{yn} can be expressed in a general form corresponding to equation (4.22), i.e.:

$$\begin{aligned}
u_{an}(t) &= \sum_{n=1}^{\infty} a_{0n}\ \cos\left(n\omega_0 t\right) + \sum_{m=1}^{\infty}\sum_{n=-\infty}^{\infty} a_{mn}\ \cos\left(m\omega_c t + n\omega_0 t\right) \\
u_{xn}(t) &= \sum_{n=1}^{\infty} a_{0n}\ \cos\left(n\omega_0 t\right) + \sum_{m=1}^{\infty}\sum_{n=-\infty}^{\infty} a_{mn}\ \cos\left(m\left[\omega_c t + \Theta_c\right] + n\omega_0 t\right) \\
u_{bn}(t) &= \sum_{n=1}^{\infty} a_{0n}\ \cos\left(n\left[\omega_0 t - \frac{4\pi}{3}\right]\right) \\
&\quad + \sum_{m=1}^{\infty}\sum_{n=-\infty}^{\infty} a_{mn}\ \cos\left(m\omega_c t + n\left[\omega_0 t - \frac{4\pi}{3}\right]\right) \\
u_{yn}(t) &= \sum_{n=1}^{\infty} a_{0n}\ \cos\left(n\left[\omega_0 t - \frac{4\pi}{3}\right]\right) \\
&\quad + \sum_{m=1}^{\infty}\sum_{n=-\infty}^{\infty} a_{mn}\ \cos\left(m\left[\omega_c t + \Theta_c\right] + n\left[\omega_0 t - \frac{4\pi}{3}\right]\right)
\end{aligned}$$

The line to line voltages are then according equations (5.1) and (5.2):

$$\begin{aligned}
u_{ab_1}(t) =& 2\sum_{m=1}^{\infty}\sum_{n=-\infty}^{\infty} a_{mn}\ \sin\left(m\frac{\Theta_c}{2}\right)\sin\left(n\frac{\pi}{3}\right) \\
&\times\cos\left(m\left[\omega_c t + \frac{\Theta_c}{2}\right] + n\left[\omega_0 t + \frac{2\pi}{3}\right]\right)
\end{aligned} \tag{5.6}$$

$$\begin{aligned}
u_{ab_2}(t) =& 2\sum_{n=1}^{\infty} a_{0n}\ \sin\left(n\frac{\pi}{3}\right)\cos\left(n\left[\omega_0 t + \frac{\pi}{6}\right]\right) \\
&+2\sum_{m=1}^{\infty}\sum_{n=-\infty}^{\infty} a_{mn}\ \cos\left(m\frac{\Theta_c}{2}\right)\sin\left(n\frac{\pi}{3}\right) \\
&\times\sin\left(m\left[\omega_c t + \frac{\Theta_c}{2}\right] + n\left[\omega_0 t - \frac{2\pi}{3}\right]\right)
\end{aligned} \tag{5.7}$$

As seen from the equations (5.6) and (5.7), independently from the modulation technique, u_{ab_1} does not present any baseband harmonics, whereas u_{ab_2} does. Carrier and sideband harmonics exist for both voltages, but for $\Theta_c = 0$, there are no harmonics expected in the first subspace due to the $\sin(m\frac{\Theta_c}{2})$-term. In the second subspace, however, these harmonic components are scaled with $\cos(m\frac{\Theta_c}{2}) = 1$ for $\Theta_c = 0$. This relationship is visualized with the harmonic spectra of both subspaces in Figure 5.2.

For values $0 < \Theta_c < \pi$ there exist harmonic components in both subspaces, but with a decreased WTHD-factor in the second (WTHD$_2$) and an increased value counting for the first subspace (WTHD$_1$). For $\Theta_c = \pi/2$, the $\cos(m\ \Theta_c/2)$-term of equation (5.7) is zero and the $\sin(m\ \Theta_c/2)$-term of equation (5.6) is one for even carrier multiples, i.e. m is a multiple of 2. Therefore, these carriers and their corresponding sideband harmonic components are mapped onto the first subspace and cancel out in the second one. For the same mathematical reasons at $\Theta_c = \pi$ the components of the odd carrier multiples are zero in subspace 2 and only appear in the first subspace.

In antiparallel operation mode, similar relationships may be discovered between carrier offset angle and harmonic components. Applying the offset angles of (5.3) and (5.4) to the phase voltage equation (4.22) achieves again the line-to-line voltages with equations (5.1) and (5.2):

$$\begin{aligned}
u_{ab_1}(t) =& 2\sum_{n=1}^{\infty} a_{0n}\ \sin\left(n\frac{\pi}{3}\right)\cos\left(n\left[\omega_0 t - \frac{\pi}{6}\right]\right)\\
&+2\sum_{m=1}^{\infty}\sum_{n=-\infty}^{\infty} a_{mn}\ \sin\left(\frac{m\Theta_c - n\pi}{2}\right)\sin\left(n\frac{\pi}{3}\right)\\
&\times\cos\left(m\left[\omega_c t + \frac{\Theta_c}{2}\right] + n\left[\omega_0 t - \frac{5\pi}{6}\right]\right) \qquad (5.8)\\
u_{ab_2}(t) =& 2\sum_{m=1}^{\infty}\sum_{n=-\infty}^{\infty} a_{mn}\ \cos\left(\frac{m\Theta_c - n\pi}{2}\right)\sin\left(n\frac{\pi}{3}\right)\\
&\times\sin\left(m\left[\omega_c t + \frac{\Theta_c}{2}\right] + n\left[\omega_0 t + \frac{5\pi}{6}\right]\right) \qquad (5.9)
\end{aligned}$$

The differences between equations (5.6) and (5.8) as well as (5.7) and (5.9) are the $\sin\left(\frac{m\Theta_c - n\pi}{2}\right)$- and $\cos\left(\frac{m\Theta_c - n\pi}{2}\right)$-terms instead of $\sin\left(m\frac{\Theta_c}{2}\right)$ and $\cos\left(m\frac{\Theta_c}{2}\right)$, respectively. These expressions lead to harmonic components in the non-operating subspace for any Θ_c and the SS technique applied there (see Figure 5.3). The square-sum of the individual WTHD-values at a certain angle, however, are equal.

Generally speaken, one can conclude that:

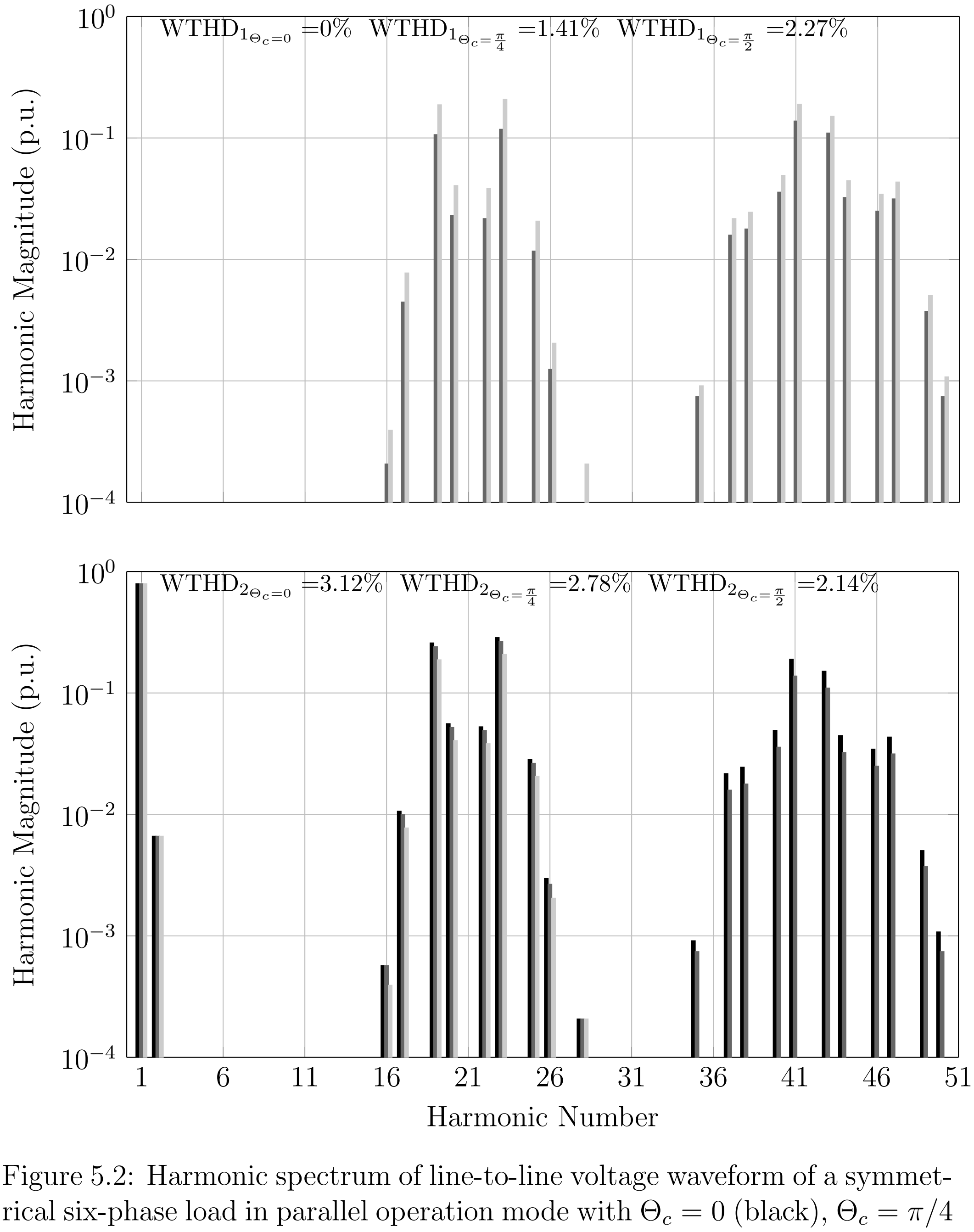

Figure 5.2: Harmonic spectrum of line-to-line voltage waveform of a symmetrical six-phase load in parallel operation mode with $\Theta_c = 0$ (black), $\Theta_c = \pi/4$ (anthracite-gray), and $\Theta_c = \pi/2$ (gray) shifting ($M = 0.78$, $p = 21$). Top: spectrum of first subspace. Bottom: spectrum of second subspace.

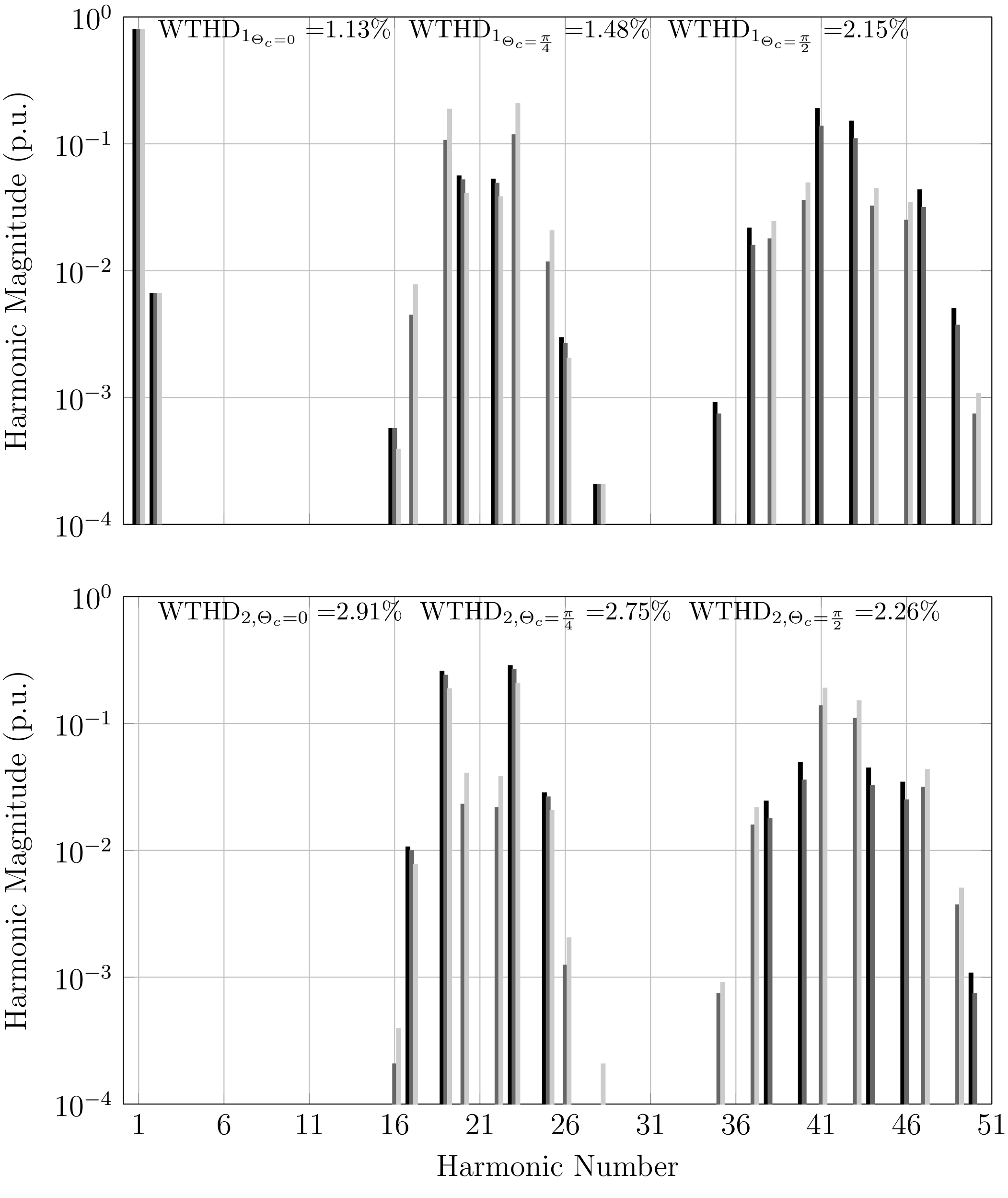

Figure 5.3: Harmonic spectrum of line-to-line voltage waveform of a symmetrical six-phase load in anti-parallel operation mode with $\Theta_c = 0$ (black), $\Theta_c = \pi/4$ (anthracite-gray), and $\Theta_c = \pi/2$ (gray) shifting ($M = 0.78$, $p = 21$). Top: spectrum of first subspace. Bottom: spectrum of second subspace.

- Fundamental component and baseband harmonics exist only in the subspace of operation.
- Carrier harmonics do not exist, since they are the same for all phases.
- Sideband harmonics can exist in both subspaces depending on Θ_c.
- Due to the phase shift of the fundamental wave (Θ_0) between two phases of the same set, there exists a $\sin(n\ \pi/3)$-term in the line-to-line voltages which eliminates all triple harmonics in both subspaces (i.e. n is a multiple of 3).

Operating the machine in parallel mode with a phase shift angle of $\Theta_c = 0$ produces a line-to-line voltage as shown in Figure 5.4a for the natural sampling technique in time-domain. Raising the shift angle to $\Theta_c = \pi/2$ doubles the number of possible voltage levels for U_{ab_2}. Additionally, distortion in subspace 2 is decreased, while distortion in the first subspace is increased, as seen in Figure 5.4b.

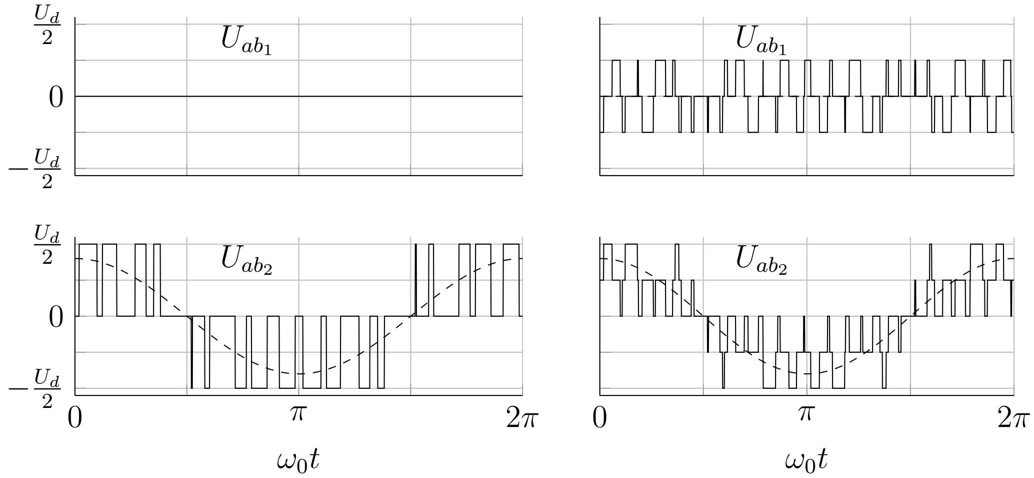

(a) Waveforms for $\Theta_c = 0$ (b) Waveforms for $\Theta_c = \frac{\pi}{2}$

Figure 5.4: Symmetrical sampled line-to-line inverter output waveforms for different carrier phase offset angles. Dashed lines: Reference voltage waveforms (parallel operation mode) [40].

5.2 Distortion Functions

As shown before, the WTHD factor can be considered separately for the two subspaces. The individual values, WTHD_1 and WTHD_2, are properties of the inverter output voltage and do not take into account any load parameters. In order to calculate overall WTHD as a figure of merit, the inductance ratio $\kappa = L_{\sigma_1}/L_{\sigma_2}$ must be included. This parameter represents the limitation of the high frequency current in subspace 1 in relation to subspace 2. The overall equation then becomes:

$$\mathrm{WTHD} = \sqrt{\left(\frac{\mathrm{WTHD}_1}{\kappa}\right)^2 + \left(\mathrm{WTHD}_2\right)^2} \tag{5.10}$$

The inductance ratio κ is a design parameter, and it is usually constant during operation. The value is dependent mainly on drive construction variables such as stator and rotor winding configuration, position of flux barriers, or the presence of auxiliarly components such as transformers.

For this paper, the experimental portion seen in Figure 3.2 was conducted on a test bench with a standard one layer distributed winding per phase. This setup results in $\kappa \approx 1$. In the case that an auxiliary transformer is used between the inverters and the machine, the inductance ratio increases to $\kappa \to \infty$ as described in Section 3.4.

5.2.1 Naturally Sampled Reference

For the following studies, it is useful to introduce a characteristic parameter Φ for each modulation technique. In general, this parameter is defined as the harmonic magnitude a_{mn} weighted with the frequency $mp + n$ and extended with $\sin\left(n\frac{\pi}{3}\right)$, representing the triple harmonics elimination:

$$\Phi = \frac{a_{mn}}{mp+n}\sin\left(n\frac{\pi}{3}\right) \tag{5.11}$$

The modulation parameter Φ_{NS} for the NS method is derived from the harmonic amplitudes of equation (4.12):

$$\Phi_{NS} = \frac{1}{mp+n}\frac{1}{m}J_n\left(2mM\right)\sin\left(\left[m+n\right]\frac{\pi}{2}\right)\sin\left(n\frac{\pi}{3}\right) \tag{5.12}$$

Taking into account equation (4.27), the WTHD values in anti-parallel operation can be estimated as follows:

$$\mathrm{WTHD}_1 \approx 2\sqrt{\frac{1}{3}\sum_{m=1}^{\infty}\sum_{n=-\infty}^{\infty}\Phi_{NS}^2\sin\left(\frac{m\Theta_c - n\pi}{2}\right)^2} \tag{5.13}$$

$$\mathrm{WTHD}_2 \approx 2\sqrt{\frac{1}{3}\sum_{m=1}^{\infty}\sum_{n=-\infty}^{\infty}\Phi_{NS}^2\cos\left(\frac{m\Theta_c - n\pi}{2}\right)^2} \tag{5.14}$$

Figure 5.7 shows the WTHD values as a function of Θ_c and M for the antiparallel mode of operation with $p = 21$ and $\kappa = 1$. The first and second subspace, as well as the overall WTHD are shown. As seen there, an optimal value for Θ_c exists which minimizes the distortions of the first subspace. The trajectory of optimal angles, however, causes maximum distortions in the second subspace. Calculating the overall losses according to equation (5.10) results in a function independent of Θ_c (see Figure 5.7c).

For parallel operation, the equations for WTHD in the two subspaces are:

$$\mathrm{WTHD}_1 \approx 2\sqrt{\frac{1}{3}\sum_{m=1}^{\infty}\sum_{n=-\infty}^{\infty}\Phi_{NS}^2 \sin\left(m\frac{\Theta_c}{2}\right)^2} \tag{5.15}$$

$$\mathrm{WTHD}_2 \approx 2\sqrt{\frac{1}{3}\sum_{m=1}^{\infty}\sum_{n=-\infty}^{\infty}\Phi_{NS}^2 \cos\left(m\frac{\Theta_c}{2}\right)^2} \tag{5.16}$$

The WTHD results for the parallel mode of operation are shown in Figure 5.8 for $p = 21$ and $\kappa = 1$. By comparing Figures 5.7a and 5.8b, the WTHD is seen to be symmetrical about $\Theta_c = \pi/2$. Figures 5.7b and 5.8a show the same relationship. Therefore the overall losses for parallel and antiparallel operation must be independent of Θ_c when $\kappa = 1$.

5.2.2 Symmetrical Regular Sampled Reference

Applying the SS technique changes the characteristic parameter to:

$$\Phi_{SS} = \frac{p}{(mp+n)^2} J_n\left(2M\left[m+\frac{n}{p}\right]\right)\sin\left(\left[m+\frac{n}{p}+n\right]\frac{\pi}{2}\right)\sin\left(n\frac{\pi}{3}\right) \tag{5.17}$$

In this section, only the WTHD values for the subspace of operation will be considered. The WTHD of the non-considered subspace could be calculated by changing Φ_{NS} into Φ_{SS} of equation (5.14) or (5.15) respectively.

Recall that in the SS and AS sampling methods, the value of the fundamental wave is sampled and held in order to compare to the carrier. This approach adds extra distortion to the output waveform. Therefore, a different characteristic parameter and an additional term are seen in the WTHD calculation. For anti-parallel operation it is:

$$\mathrm{WTHD}_1 \approx \sqrt{\underbrace{\sum_{n=2}^{\infty}}_{m=0}\Phi_{SS}^2 + \frac{4}{3}\sum_{m=1}^{\infty}\sum_{n=-\infty}^{\infty}\Phi_{SS}^2 \sin\left(\frac{m\Theta_c - n\pi}{2}\right)^2} \tag{5.18}$$

The losses in the second subspace can be calculated as follows (parallel operation):

$$\mathrm{WTHD}_2 \approx \sqrt{\underbrace{\sum_{n=2}^{\infty}}_{m=0} \Phi_{SS}^2 + \frac{4}{3}\sum_{m=1}^{\infty}\sum_{n=-\infty}^{\infty} \Phi_{SS}^2 \cos\left(m\frac{\Theta_c}{2}\right)^2} \tag{5.19}$$

5.2.3 Asymmetrical Regular Sampled Reference

The characteristic parameter Φ_{AS} of the asymmetric regular sampling technique can be defined as follows:

$$\Phi_{AS} = \frac{p}{(mp+n)^2} J_n\left(2M\left[m+\frac{n}{p}\right]\right)\sin\left([m+n]\frac{\pi}{2}\right)\sin\left(n\frac{\pi}{3}\right) \tag{5.20}$$

The expression for WTHD_1 and WTHD_2 for the parallel and antiparallel operation modes is calculated using equation (5.14) and (5.15), as explained in section 5.2.2.

In antiparallel operation, the WTHD values in the first subspace are found to be:

$$\mathrm{WTHD}_1 \approx \sqrt{\underbrace{\sum_{n=2}^{\infty}}_{m=0} \Phi_{AS}^2 + \frac{4}{3}\sum_{m=1}^{\infty}\sum_{n=-\infty}^{\infty} \Phi_{AS}^2 \sin\left(\frac{m\Theta_c - n\pi}{2}\right)^2} \tag{5.21}$$

And for subspace 2, with parallel operation:

$$\mathrm{WTHD}_2 \approx \sqrt{\underbrace{\sum_{n=2}^{\infty}}_{m=0} \Phi_{AS}^2 + \frac{4}{3}\sum_{m=1}^{\infty}\sum_{n=-\infty}^{\infty} \Phi_{AS}^2 \cos\left(m\frac{\Theta_c}{2}\right)^2} \tag{5.22}$$

5.3 Operation Strategies

Operating the machine while minimizing overall current distortion is highly desirable. An optimal strategy must therefore be developed which takes into account the different values of inductance ratio κ. According to equation (5.10), when $\kappa < 1$ the overall WTHD is dominated by losses in the first subspace, and when $\kappa > 1$ losses in the second subspace are dominant. When $\kappa = 1$, overall losses of the two subspaces are equally weighted.

Therefore, when $\kappa \neq 1$, an optimal trajectory $\Theta_c(M)$ must be found which reduces overall WTHD to a minimum. In this section, the optimal trajectories for parallel operation will be derived. Due to symmetry, the antiparallel trajectories may be obtained with a similar process.

5.3.1 Optimal Trajectory for $\kappa < 1$

For $\kappa < 1$ the losses in the first subspace dominate, leading to an optimal Θ_c trajectory if $\sin\left(m\frac{\Theta_c}{2}\right)$ is equal to zero in equation (5.15). This condition is fulfilled when $\Theta_c(M) = 0$.

$$\Theta_c(M) = 0 \tag{5.23}$$

5.3.2 Optimal Trajectory for $\kappa > 1$

For $\kappa > 1$, the optimal solution can be found by setting $\frac{d\mathrm{WTHD}_2}{d\Theta_c} = 0$, which finally results in:

$$0 = \sum_{m=1}^{\infty} \sum_{n=-\infty}^{\infty} \Phi^2 m \sin\left(m\Theta_c\right) \tag{5.24}$$

where Φ is the characteristic parameter of the applied sampling technique, as defined in equations (5.12), (5.17) and (5.20). The optimal Θ_c-values for the NS, SS and AS techniques are calculated numerically and depicted in Figure 5.5 for two different pulse ratios.

As seen there, for $M < 0.5$ the optimal values of Θ_c are close to $\pi/2$ and increase to $\Theta_c = \pi$ for $M > 0.7$. It can be observed that the optimal computed phase offsets of the three sampling techniques show only small differences for $p = 9$. And for $p = 21$ the three functions converge to match the curve $\Theta_{c_{p\to\infty}}$ for an infinitely high pulse ratio.

5.3.3 Approximated Optimal Trajectory

For ease of implementation, an explicit but approximated solution of equation (5.24) would be useful. For the natural sampling method, a simplified solution for Θ_c may be found by restricting $m \in \{1, 2\}$ and $n \in \{-2, -1, 0, 1, 2\}$, resulting in:

$$\Theta_{c_{APX}} = \arccos\left(-\frac{1}{4}\left(\frac{J_2\left(2M\right)\left(4p^2-1\right)}{J_1\left(4M\right)\left(p^2-4\right)}\right)^2\right) \tag{5.25}$$

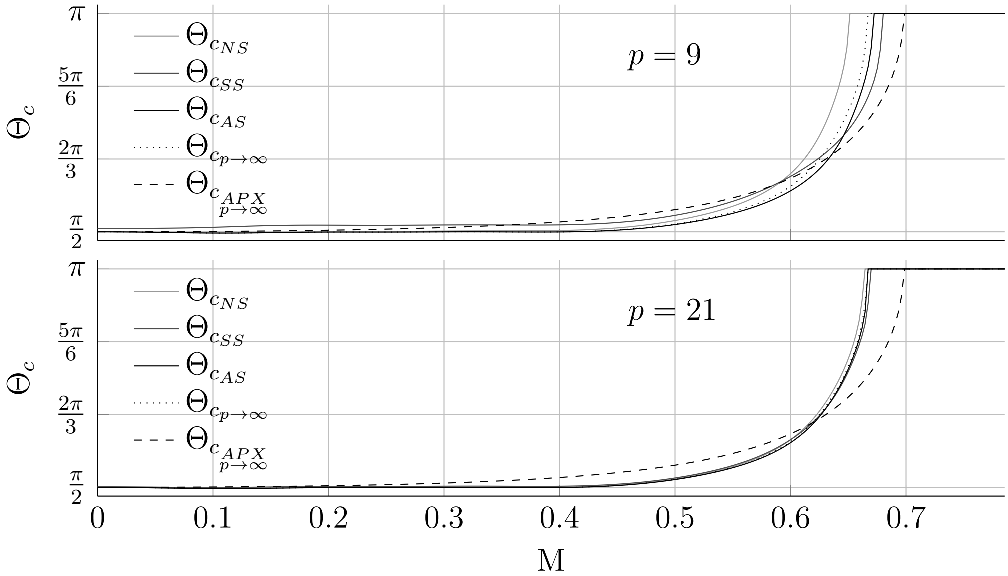

Figure 5.5: Optimal phase offset angle $\Theta_c(M)$ for the naturally sampled (NS), symmetrical regular sampled (SS) and asymmetrical regular sampled (AS) modulation technique for different pulse ratios p. In comparison: The optimal Θ_c-values for $p \to \infty$ and the approximation (APX) for $p \to \infty$ [40].

Assuming high switching frequencies, the pulse rate becomes $p \to \infty$ and the formula further simplifies as follows:

$$\Theta_{c_{\substack{APX\\p\to\infty}}} = \lim_{p\to\infty} \Theta_{c_{APX}} = \arccos\left(-4\frac{J_2\left(2M\right)^2}{J_1\left(4M\right)^2}\right) \tag{5.26}$$

The approximated trajectory of $\Theta_c(M)$ is added in Figure 5.5. Its characteristic is close to the numerically calculated ones but with notable differences. Despite the differences, Figure 5.6 proves the approximation method is accurate. The harmonic distortion function HDF, derived from the overall WTHD according equation (4.36) is depicted there. The approximated HDF trajectory labeled as $\mathrm{HDF}_{\Theta_{c_{APX}}}$ is an excellent match with the optimal HDF trajectory $\mathrm{HDF}_{\Theta_{c_{NS}}}$ achieved from equation (5.24).

In the same figure, the two loss functions $\mathrm{HDF}_{\Theta_{c_{NS}}}$ and $\mathrm{HDF}_{\Theta_c=0}$ correspond to the lower and upper bounds respectively, for $\kappa \to \infty$ and a given modulation technique and pulse ratio. The upper bound, where $\Theta_c = 0$, represents the HDF function of a common three-phase drive. For $1 < \kappa < \infty$ or any other Θ_c, the resultant loss function will lie within the shaded area. The area therefore represents the possible performance gain from using the optimal trajectory.

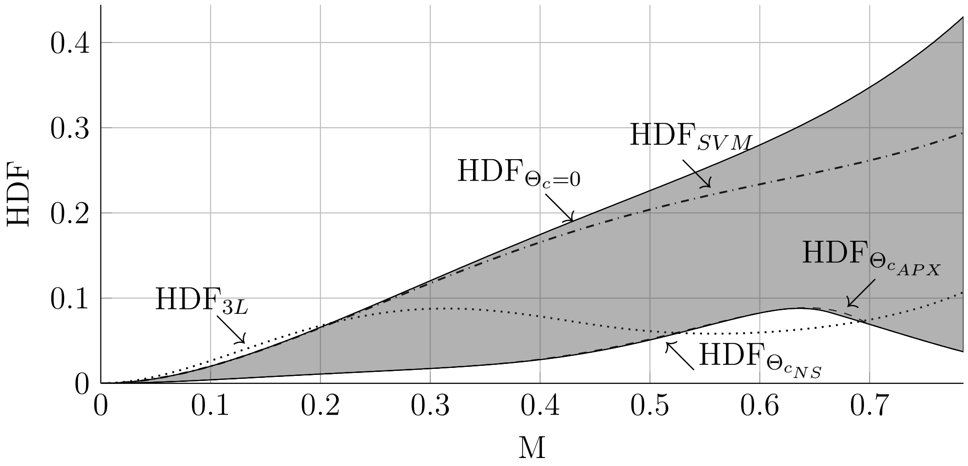

Figure 5.6: HDF characteristics for $\kappa \to \infty$ and parallel operation at $p = 21$ (naturally sampled). Shaded area: Maximal performance gain between the optimal Θ_c-trajectory and results at $\Theta_c = 0$. Dashed line: HDF-values for the approximated optimal Θ_c-trajectory; Dotted line: HDF-values for three-level PD PWM scheme; Dash-dotted line: Distortion characteristic obtained using standard space vector modulation.

The HDF characteristics of a standard three-phase space vector modulation (SVM) and a three-level phase disposition (PD) method are included for comparison. (Both methods are taken from [52]) It can be clearly seen that when $\kappa \to \infty$, the optimized $\text{HDF}_{\Theta_{c_{NS}}}$ is superior to the SVM method for the entire range of M, and even better than the PD method for a large range of M.

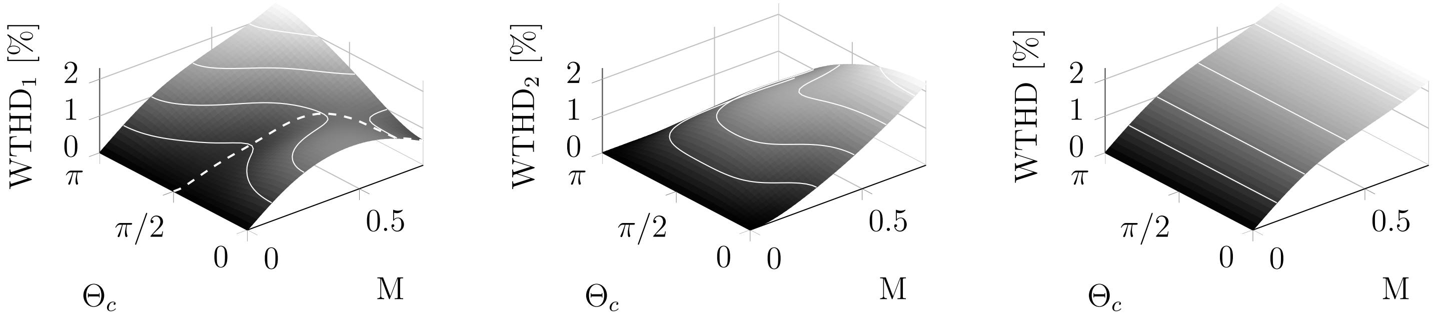

(a) WTHD of first subspace. (b) WTHD of second subspace. (c) Overall WTHD.

Figure 5.7: WTHD characteristics of the naturally sampled PWM technique for symmetrical six-phase drives, depending on the modulation index M and the phase offset angle Θ_c. The inductance ratio is $\kappa = 1$, the pulse ratio is $p = 21$, operation antiparallel mode [40].

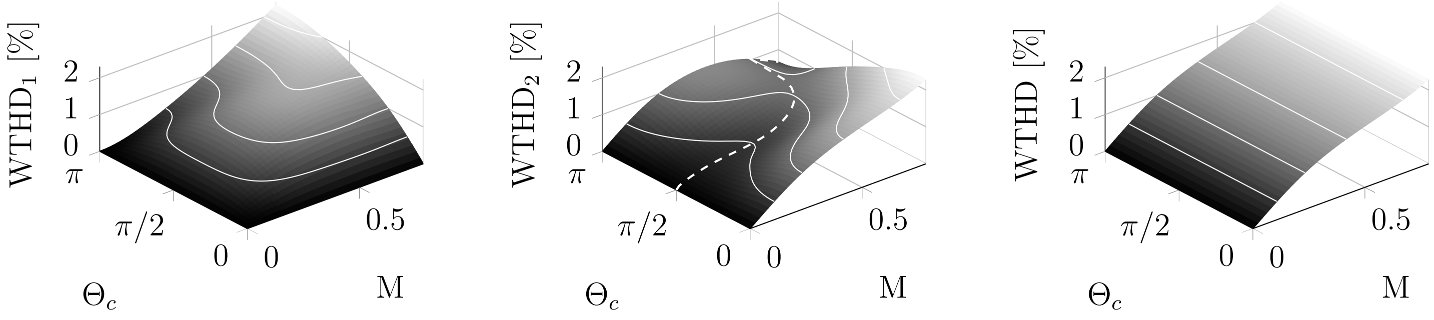

(a) WTHD of first subspace. (b) WTHD of second subspace. (c) Overall WTHD.

Figure 5.8: WTHD characteristics of the naturally sampled PWM technique for symmetrical six-phase drives, depending on the modulation index M and the phase offset angle Θ_c. The inductance ratio is $\kappa = 1$, the pulse ratio is $p = 21$, operation in parallel mode [40].

5.4 Experimental Results

Experimental tests on a 15kW six-phase induction machine drive were carried out to assess the validity of the theoretical considerations discussed previously. In order to estimate a value for the modulation quality, the current was measured and its distortion factor calculated.

The harmonic current, defined with equation (4.37), was used as a figure of merit for evaluation. Due to the symmetric phase structure, it is only necessary to measure the currents over one fundamental period of two phases lying on the same magnetic axes, i.e. a and x (compare equation (3.12) and Figure 2.5). Doing so, the harmonic currents can be decomposed and mapped onto both subspaces.

With the experimental setup explained in Section 3.4, two different cases were examined:

1. The inductances of both equivalent three-phase circuits are nearly equal: $\kappa \approx 1$
2. The inductance of circuit 1 is significantly greater than that of circuit 2: $\kappa >> 1$

Using the optional transformer as shown in Figure 3.10 leads to $\kappa >> 1$. This is because in antiparallel operation ($i_a = -i_x$) the transformer experiences a high mutual flux, resulting in a high L_{σ_1} value. In contrast, in parallel operation ($i_a = i_x$) very low mutual flux is evident. As a result, in this mode L_{σ_2} is nearly unmodified. Therefore the inductance ratio will be much greater than one.

The results for $\kappa \approx 1$ are shown in Figure 5.9. In an overall point of view, the measurements show a very good correlation with the computed predictions seen in Figure 5.8. Note the difference in the optimal Θ_c trajectory between the first and second subspace. In the first subspace, the optimal path leads to maximum I_h values, while in the second subspace it traces the minimum distortion path (see Figures 5.9a and 5.9b respectively). In the overall case the losses are, as predicted, almost independent of Θ_c (see Figure 5.9c).

The aforementioned increase in L_{σ_1} with the transformer causes the current distortion to decrease to a negligible value, as seen in Figure 5.10a. Therefore, the losses of the second subspace are the main influence on the overall distortions (compare Figures 5.10b and 5.10c). As a result, the optimal Θ_c trajectory significantly reduces the overall current distortion.

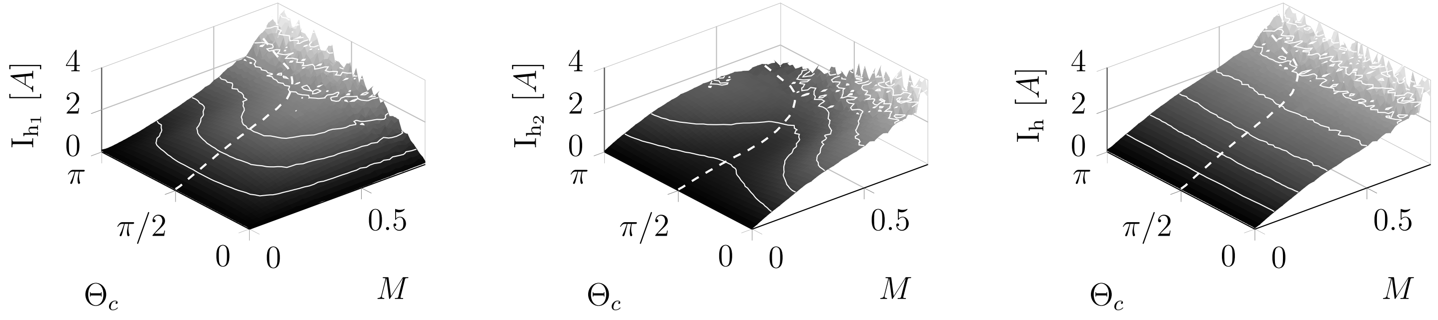

(a) Distortion of first subspace.
(b) Distortion of second subspace.
(c) Overall current distortion.

Figure 5.9: Experimental results: Current distortion dependence on modulation index M and shift angle Θ_c for $L_{\sigma_1}(19mH) \approx L_{\sigma_2}(18mH)$ and $p = 21$ (SS-modulation). Dashed line: THD-values for approximated optimal Θ_c-trajectory [42].

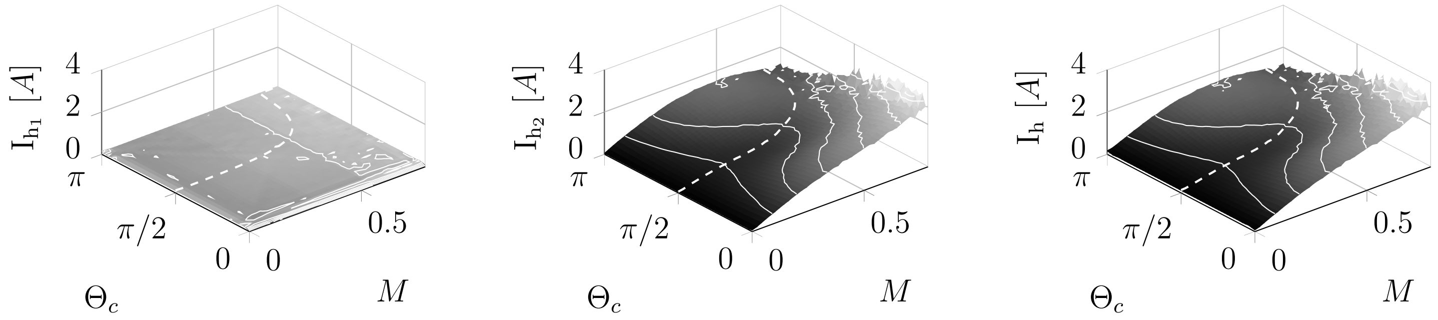

(a) Distortion of first subspace.
(b) Distortion of second subspace.
(c) Overall current distortion.

Figure 5.10: Experimental results: Current distortion dependence on modulation index M and shift angle Θ_c for $L_{\sigma_1}(200mH) >> L_{\sigma_2}(19mH)$ and $p = 21$ (SS-modulation). Dashed line: THD-values for approximated optimal Θ_c-trajectory [42].

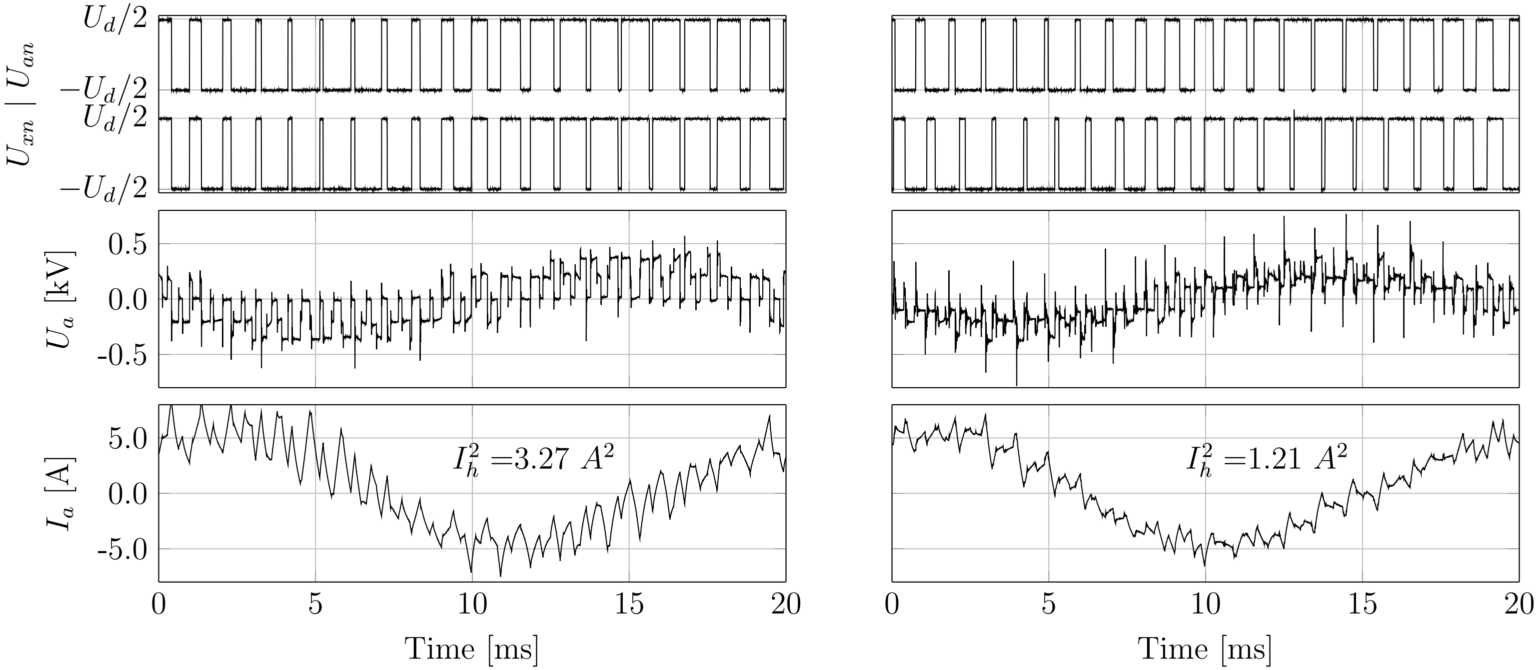

(a) Waveforms for $\Theta_c = 0$, i.e. no time-shifting between the output voltage of inverter leg a and x (top). Thus, the phase voltage (middle) and current characteristics (bottom) correspond to a common three phase machine.

(b) Waveforms obtained with the optimal phase offset angle: The output voltage of inverter leg x is time-shifted towards leg a (top). The resulting voltage of phase a includes additional voltage levels and an increased switching frequency (middle). Thus, the distortion factor of the phase current waveform is lower then for the case $\Theta_c = 0$ (bottom).

Figure 5.11: Experimental waveforms showing inverter-leg voltages U_{an} and U_{xn}, voltage and current waveforms of phase a and resulting harmonic current distortion factor comparing the six-phase drive when applying SS-modulation with different carrier phase offset angles at $M = 0.63$ and $\kappa >> 1$ [40].

Figure 5.11 shows the influence of Θ_c on the current distortion of an arbitrary machine phase. Two cases are examined. In Figure 5.11a it is $\Theta_c = 0$. This setting leads to current and voltage output waveforms which are both similar to the output of a three-phase machine.

In contrast, in Figure 5.11b Θ_c is set to its optimal value depending on M. It can be seen that the current waveform in the second case is less distorted, this observation being confirmed by the lower current distortion factor.

Chapter 6

Space Vector Modulation

In contrast to the carrier based PWM, space vector modulation (SVM) exposes many more degrees of freedom for control. For six-phase drives there are in total $2^6 = 64$ different voltage vectors applicable. Some of them are redundant in one subspace which enables their duty cycle ratio to be optimized. Furthermore, within one carrier cycle there are $6!^2 = 518400$ different sequences of vectors which may be implemented. These facts lead to an optimization problem with numerous variables.

In order to simplify the optimization process, certain voltage vectors are preselected in Section 6.1. On that basis, all possible switching sequences starting and ending with a zero vector are analyzed in Section 6.2. Due to symmetries only 11 sequences have to be chosen to solve the optimization problem in Section 6.3. Several modulation strategies can be derived from the optimization results, which do not need much calculation power on a real-time system (see Section 6.4). Experimental results in Section 6.5 validate those strategies.

6.1 Voltage Space Vectors

In order to develop a modulation strategy, the applied voltage vectors must be decomposed according to Section 3.3 into fundamental and harmonic order components. This separation allows an investigation of how different inverter switching states contribute to current distortion. States of odd harmonic order $(1, 5, 7, ...)$ are mapped to the first subspace, or $(\alpha_1\beta_1)$ plane. States of even harmonic order $(2, 10, 14, ...)$ are mapped in the second subspace, represented by the $(\alpha_2\beta_2)$ plane.

The machine may be operated in either subspace, depending on its winding distribution. Therefore the torque producing current and flux waves can be first or second order. Considering the machine design of Figure 3.2 with a standard, one layer winding, operation is in the design-intended second subspace only, i.e. the second order harmonic content is named here as *fundamental.*

In Figure 6.1b the relative vector magnitudes in the first sector of the (α_2, β_2) plane are seen to be: zero vector $\vec{v}_0$, small-sized vectors $\vec{v}_1$ and $\vec{v}_5$, medium vector $\vec{v}_3$, and large vectors $\vec{v}_2$ and $\vec{v}_4$. By considering only the small-sized and zero vectors in the (α_1, β_1) subspace, the current distortions in that subspace can be reduced.

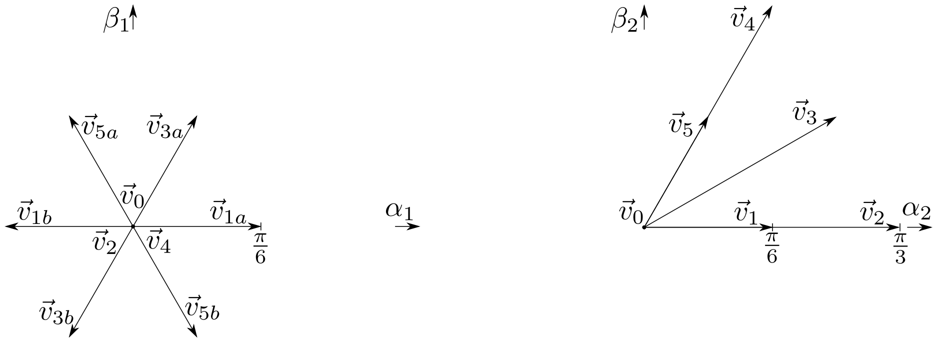

(a) Small sized and zero vectors projected onto the (α_1, β_1) plane.

(b) Vectors of the first sector projected onto the (α_2, β_2) plane.

Figure 6.1: Considered voltage space vectors and its projection onto the first and second plane [41].

By comparing Figures 6.1a and 6.1b, it can be seen that the large-sized and zero vectors of the (α_2, β_2) plane have only zero components in the (α_1, β_1) plane. However, all small- and medium-sized vectors in the (α_2, β_2) subspace become active vectors in the (α_1, β_1) subspace. Additionally, when the vectors $\vec{v}_1$, $\vec{v}_3$, and $\vec{v}_5$ of the (α_2, β_2) subspace are represented within the (α_1, β_1) subspace, two different forms of each vector are possible. This is due to the two possible switching states used to produce each voltage state as seen from figure 6.1. These additional states are included in Table 6.1 under the labels *a* and *b*.

6.2 Space Vector Sequences

The goal of space vector modulation is to approximate the reference voltage $\vec{v}^*$ by applying a sequence of voltage vectors. The integral of the applied voltages over the switching period T_s should offer the same volt-seconds as $\vec{v}^*$. Due to the discrete nature of the voltage vectors, the following equation

Voltage Vector		Switching State
$\vec{v}_0$		000000
		000111
		111000
		111111
$\vec{v}_1$	$\vec{v}_{1a}$	100000
		100111
	$\vec{v}_{1b}$	000100
		111100
$\vec{v}_2$		100100
$\vec{v}_3$	$\vec{v}_{3a}$	100101
	$\vec{v}_{3b}$	101100
$\vec{v}_4$		101101
$\vec{v}_5$	$\vec{v}_{5a}$	000101
		111101
	$\vec{v}_{5b}$	101000
		101111

Table 6.1: Considered voltage space vectors and switching states

is applicable in both subspaces:

$$\sum_k \vec{v}_k t_k = \vec{v}^* T_s, \text{ with } k \in \{0, 1a, 1b, 2, \dots, 5b\} \tag{6.1}$$

where t_k is the active time of the voltage vector $\vec{v}_k$.

This strategy leads to a very high number of possible sequences. Assuming that within T_s, each inverter half bridge of Figure 3.7 may change its state twice, i.e. $+\frac{U_d}{2} \rightarrow -\frac{U_d}{2} \rightarrow +\frac{U_d}{2}$ or $-\frac{U_d}{2} \rightarrow +\frac{U_d}{2} \rightarrow -\frac{U_d}{2}$, there are $6!^2 = 518400$ different space vector sequences applicable for the six-phase drive. For purposes of computation and optimization, this number must be greatly reduced.

Simplification can be achieved by considering only the vectors given in Table 6.1 and Figure 6.1. Additionally, only the sequences symmetrical towards $T_s/2$ will be used. Restricting the scope to a half-cycle, two different types of sequences can be distinguished: the point- and axial-symmetric sequence. Point-symmetric sequences begin with the vector $\vec{v}_0 = |000000|$ and end with $\vec{v}_0 = |111111|$ or vice versa. The axial-symmetric sequences start with $\vec{v}_0 = |000111|$ and end with $\vec{v}_0 = |111000|$ or vice versa. Taking into account the aforementioned limitations, all possible sequences of the point-symmetric type are depicted in Figure 6.2a and the ones of the axial-symmetric type in Figure 6.2b.

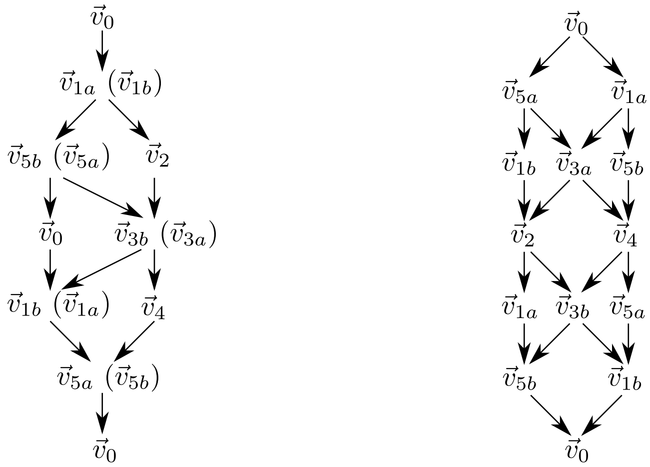

(a) Sequences of the point-symmetric type, starting with $\vec{v}_0 = |000000|$ and ending with $\vec{v}_0 = |111111|$. Alternative vectors in brackets.

(b) Sequences of the axial-symmetric type, starting with $\vec{v}_0 = |000111|$ and ending with $\vec{v}_0 = |111000|$.

Figure 6.2: Flow chart of feasible continuous switching sequences within a half cycle of the switching period [41].

Note that in the point-symmetric sequences seen in Figure 6.1b, two types of paths are possible: one which excludes the vectors in parenthesis (the native path), and one which includes the bracketed vectors (the alternative path). By comparing all possible paths of Figure 6.2a with the vectors seen in Figure 6.1b five different pulse patterns become visible in the (α_2, β_2) subspace.

However, considering the native paths only creates five different pulse patterns in the (α_1, β_1) plane. Following the same route but using the alternative paths where applicable, the same patterns are achieved but rotated by π. Following a native path within the positive half-cycle and the corresponding alternative path in the opposite direction within the negative half-cycle results in an extra degree of freedom, enabling some optimization as will be discussed in Section 6.3. Table 6.2 summarizes the native vector sequences of the point-symmetric type within the positive half-cycle from No. 1 to 5.

The axial-symmetric sequence, in contrast, offers no alternative vectors but a higher number of branches. This increases the number of possible sequences to 14. However, a reference vector $\vec{v}^* = [0, 0]$ is assumed for the (α_1, β_1) plane, reducing the number of relevant sequences to 6, as summarized in Table 6.2 (No. 6 to 11) for the positive half-cycle. The sequence of the negative half-cycle is identical but in the reverse order.

No.	Voltage Vector Sequences						
1	$\vec{v}_0 \rightarrow$	$\vec{v}_{1a} \rightarrow$	$\vec{v}_2 \rightarrow$	$\vec{v}_{3b} \rightarrow$	$\vec{v}_4 \rightarrow$	$\vec{v}_{5a} \rightarrow$	$\vec{v}_0$
2	$\vec{v}_0 \rightarrow$	$\vec{v}_{1a} \rightarrow$	$\vec{v}_2 \rightarrow$	$\vec{v}_{3b} \rightarrow$	$\vec{v}_{1b} \rightarrow$	$\vec{v}_{5a} \rightarrow$	$\vec{v}_0$
3	$\vec{v}_0 \rightarrow$	$\vec{v}_{1a} \rightarrow$	$\vec{v}_{5b} \rightarrow$	$\vec{v}_{3b} \rightarrow$	$\vec{v}_4 \rightarrow$	$\vec{v}_{5a} \rightarrow$	$\vec{v}_0$
4	$\vec{v}_0 \rightarrow$	$\vec{v}_{1a} \rightarrow$	$\vec{v}_{5b} \rightarrow$	$\vec{v}_{3b} \rightarrow$	$\vec{v}_{1b} \rightarrow$	$\vec{v}_{5a} \rightarrow$	$\vec{v}_0$
5	$\vec{v}_0 \rightarrow$	$\vec{v}_{1a} \rightarrow$	$\vec{v}_{5b} \rightarrow$	$\vec{v}_0 \rightarrow$	$\vec{v}_{1b} \rightarrow$	$\vec{v}_{5a} \rightarrow$	$\vec{v}_0$
6	$\vec{v}_0 \rightarrow$	$\vec{v}_{1a} \rightarrow$	$\vec{v}_{5b} \rightarrow$	$\vec{v}_4 \rightarrow$	$\vec{v}_{5a} \rightarrow$	$\vec{v}_{1b} \rightarrow$	$\vec{v}_0$
7	$\vec{v}_0 \rightarrow$	$\vec{v}_{1a} \rightarrow$	$\vec{v}_{3a} \rightarrow$	$\vec{v}_4 \rightarrow$	$\vec{v}_{3b} \rightarrow$	$\vec{v}_{1b} \rightarrow$	$\vec{v}_0$
8	$\vec{v}_0 \rightarrow$	$\vec{v}_{1a} \rightarrow$	$\vec{v}_{3a} \rightarrow$	$\vec{v}_2 \rightarrow$	$\vec{v}_{3b} \rightarrow$	$\vec{v}_{1b} \rightarrow$	$\vec{v}_0$
9	$\vec{v}_0 \rightarrow$	$\vec{v}_{5a} \rightarrow$	$\vec{v}_{3a} \rightarrow$	$\vec{v}_4 \rightarrow$	$\vec{v}_{3b} \rightarrow$	$\vec{v}_{5b} \rightarrow$	$\vec{v}_0$
10	$\vec{v}_0 \rightarrow$	$\vec{v}_{5a} \rightarrow$	$\vec{v}_{3a} \rightarrow$	$\vec{v}_2 \rightarrow$	$\vec{v}_{3b} \rightarrow$	$\vec{v}_{5b} \rightarrow$	$\vec{v}_0$
11	$\vec{v}_0 \rightarrow$	$\vec{v}_{5a} \rightarrow$	$\vec{v}_{1b} \rightarrow$	$\vec{v}_2 \rightarrow$	$\vec{v}_{1a} \rightarrow$	$\vec{v}_{5b} \rightarrow$	$\vec{v}_0$

Table 6.2: Voltage Vector Sequences

6.3 Optimization

The objective of optimization is to find a valid solution for the on-times t_k of the seven vectors $\vec{v}_k$ which minimizes the overall current distortion. To comply with the constraint given by equation (6.1), the on-times of the voltage vectors need to be evaluated for the sequences seen in Table 6.2. Due to the symmetry discussed in Section 6.2, it is only necessary to evaluate the on-times of the seven vectors $\vec{v}_k$ applied within one half-cycle.

Introducing the duty cycle d_k as the relative on-time of vector k over the half-cycle ($d_k = 2t_k/T_s$), the following relation holds:

$$\sum_{k=1}^{7} \vec{v}_k d_k = \vec{v}^* \tag{6.2}$$

In this section, each sequence of Table 6.2 will be optimized for a certain reference vector with equation (6.2) as a constraint as well as additional bound constraints for each duty cycle. A solution for the seven duty cycles will then be found which minimizes overall current distortion.

6.3.1 Constraints

First, the optimization process must take into account the bound condition of the duty cycles. According to equation (6.2) d_k must be in the range of:

$$0 \leq d_k \leq 1 \tag{6.3}$$

From the definition of a duty cycle, the sum of all on-times within a half cycle must be equal to $T_s/2$. Therefore the sum of all duty cycles will be unity:

$$\sum_{k=1}^{7} d_k = 1 \tag{6.4}$$

In addition, the optimization result must satisfy equation (6.2), which can be expressed in the form:

$$\mathbf{A}_{eq} \cdot \vec{d} = \vec{b}_{eq} \tag{6.5}$$

where $\vec{d}$ is the duty cycle vector $\vec{d} = [d_1, \cdots, d_7]^T$, $\mathbf{A}_{eq}$ is the matrix of linear equalities, and the $\vec{b}_{eq}$ vector includes the reference voltage for both subspaces as well as the sum of all duty cycles. The content of $\mathbf{A}_{eq}$ and $\vec{b}_{eq}$ is dependent on the applied vector sequence. Given the voltage vector reference components in both subspaces $v^*_{\alpha_1}, \cdots, v^*_{\beta_2}$, the unity factor seen in equation (6.4), and using the axial-symmetric sequence illustrated in Figure 6.2b, then $\vec{b}_{eq}$ will have form:

$$\vec{b}_{eq} = \left[v^*_{\alpha_1}, v^*_{\beta_1}, v^*_{\alpha_2}, v^*_{\beta_2}, 1\right]^T \tag{6.6}$$

The torque and flux generating currents exist only in the (α_2, β_2) subspace. Therefore the (α_1, β_1) reference elements are equal to zero:

$$v^*_{\alpha_1} = v^*_{\beta_1} = 0 \tag{6.7}$$

The $\mathbf{A}_{eq}$ matrix includes the coordinates of the applied voltage vectors expressed in α, β-coordinates and a unity row to satisfy equation (6.4). For example, applying sequence 6 of Table 6.2 results in:

$$\mathbf{A}_{eq} = \begin{bmatrix} 0 & \frac{\pi}{6} & \frac{\pi}{12} & 0 & -\frac{\pi}{12} & -\frac{\pi}{6} & 0 \\ 0 & 0 & -\frac{\pi}{4\sqrt{3}} & 0 & \frac{\pi}{4\sqrt{3}} & 0 & 0 \\ 0 & \frac{\pi}{6} & \frac{\pi}{12} & \frac{\pi}{6} & \frac{\pi}{12} & \frac{\pi}{6} & 0 \\ 0 & 0 & \frac{\pi}{4\sqrt{3}} & \frac{\pi}{2\sqrt{3}} & \frac{\pi}{4\sqrt{3}} & 0 & 0 \\ 1 & 1 & 1 & 1 & 1 & 1 & 1 \end{bmatrix} \tag{6.8}$$

Comparing equation (6.5) with (6.6) and (6.8), the linear system of equations has seven variables and must fulfill five conditions. Thus two degrees of freedom are available for optimization if the axial-symmetric sequences are applied. Using the point-symmetric type, however, increases the possibilities. As explained in Section 6.2, taking a native path for one half-cycle and the corresponding alternative path for the next half-cycle leads to zero volt-seconds in the first subspace, independent of the duty cycles. For example, taking sequence 1 of table 6.2 results in a four degrees of freedom optimization problem with the following parameters:

$$\mathbf{A}_{eq} = \begin{bmatrix} 0 & \frac{\pi}{6} & \frac{\pi}{3} & \frac{\pi}{4} & \frac{\pi}{6} & \frac{\pi}{12} & 0 \\ 0 & 0 & 0 & \frac{\pi}{4\sqrt{3}} & \frac{\pi}{2\sqrt{3}} & \frac{\pi}{4\sqrt{3}} & 0 \\ 1 & 1 & 1 & 1 & 1 & 1 & 1 \end{bmatrix} \tag{6.9}$$

$$\vec{b}_{eq} = \left[v^*_{\alpha_2}, v^*_{\beta_2}, 1\right]^T \tag{6.10}$$

6.3.2 Optimization Function

An optimal modulation strategy should be capable of dealing with the aforementioned conditions as well as reducing the current harmonics of the load to a minimum. An expression for the overall distortion factor must be determined. First the leakage factor explained in Section 3.2.4 must be taken into account with the following method of estimation. Since the inductance of the (α_1, β_1) circuit, L_{σ_1} is not necessarily equal to the inductance of the (α_2, β_2) circuit, L_{σ_2}, it is proposed to relate the harmonic flux of the first and second subspaces with the inverse inductance ratio vector $\vec{\kappa}$:

$$\vec{\kappa} = \left[\frac{1}{\kappa^2}\ \frac{1}{\kappa^2}\ 1\ 1\right]^T \tag{6.11}$$

where $\kappa = \frac{L_{\sigma_1}}{L_{\sigma_2}}$.

Next, the harmonic flux vector $\vec{\lambda}_h = \left[\lambda_{h_{\alpha_1}}, \lambda_{h_{\beta_1}}, \lambda_{h_{\alpha_2}}, \lambda_{h_{\beta_2}}\right]^T$ has to be derived. Assuming high switching frequencies, i.e. a switching to fundamental frequency ratio of $f_s/f_0 > 20$, and a mainly inductive load with very small resistance, one can apply the harmonic flux calculation in order to estimate the current distortion, as explained in Section 4.2.

Therefore, $\vec{\lambda}_h$ is calculated by integrating the applied voltage vectors $\vec{v}_k$ with respect to the time d:

$$\vec{\lambda}_h\left(M, \Theta\right) = \int_0^1 \vec{v}_k - \vec{v}^* dd \tag{6.12}$$

where the reference voltage vector $\vec{v}^*$ is assumed constant during a switching cycle.

The harmonic flux rms value is expressed as:

$$\vec{\lambda}_{rms}\left(M, \Theta\right) = \int_0^1 \left[\vec{\lambda}_h - \vec{\lambda}_{avg}\right] \circ \left[\vec{\lambda}_h - \vec{\lambda}_{avg}\right] dd \tag{6.13}$$

where $\vec{\lambda}_{avg}$ is the average flux vector for one switching cycle. Due to system symmetry, the average flux values in the (α_2, β_2) directions must be zero. This rule also applies to the average flux in the (α_1, β_1) subspace if sequences of the second type (No. 6-11 of Table 6.2) are under consideration. For sequences No. 1-5, however, the (α_1, β_1) components of average flux are nonzero and the vector can be written: $\vec{\lambda}_{avg} = \left[\lambda_{avg_{\alpha_1}}, \lambda_{avg_{\beta_1}}, 0, 0\right]^T$.

Using the harmonic flux $\vec{\lambda}_{rms}$ and inverse inductance ratio $\vec{\kappa}$, an expression for the overall distortion can be found:

$$\lambda_{rms}^2 (M, \Theta) = \vec{\lambda}_{rms}^T \cdot \vec{\kappa} \tag{6.14}$$

6.3.3 Optimization Results

Within the constraints of Section 6.3.1, minimizing the distortion explained in Section 6.3.2 creates harmonic flux trajectories according to equation (6.12) in both of the subspaces. The trajectories vary with respect to the voltage vector sequence and the reference vector described by M and Θ.

Figure 6.3 depicts the harmonic flux trajectories of vector sequences No. 2 and 10 from Table 6.2. For comparison, a trajectory is also illustrated based on the standard three-phase SVM technique as explained in Section 6.4.1. Comparing Figures 6.3a and 6.3b, it can be seen that the standard technique creates a harmonic flux in the (α_2, β_2) plane only. The trajectory forms two triangles of identical size, rotated by a factor of π, each circumscribed within one half cycle. The trajectories of sequences 2 and 10 in this subspace each form two smaller-sized triangles. In sequence 2, the triangles are circumscribed once within a cycle and in sequence 10 they are circumscribed twice. Both sequences therefore have smaller harmonic flux values compared to the standard SVM technique in the (α_2, β_2) subspace.

However, in subspace (α_1, β_1) seen in Figure 6.3a, sequences 2 and 10 lead to extra distortion due to the active vectors applied. Within one cycle, the trajectories of sequences 2 and 10 start and end at zero and they are circumscribed once per cycle. Because sequence 10 is of the second type, the average values $\lambda_{avg_{\alpha_1}}$ and $\lambda_{avg_{\beta_1}}$ are zero as discussed in section 6.3.2. Sequence 2, however, is of first type and its average value is not necessarily equal to zero.

The optimization produces an overall distortion factor λ_{rms}^2 corresponding to any sequence of Table 6.2 and any combination of M and Θ which fulfills the constraints. For any combination there exist a sequence which offers the minimum λ_{rms}^2 values, as shown in Figure 6.8 (bottom) for different inductance ratios. For $\kappa = 1$, six of the sequences from Table 6.1 are visible:

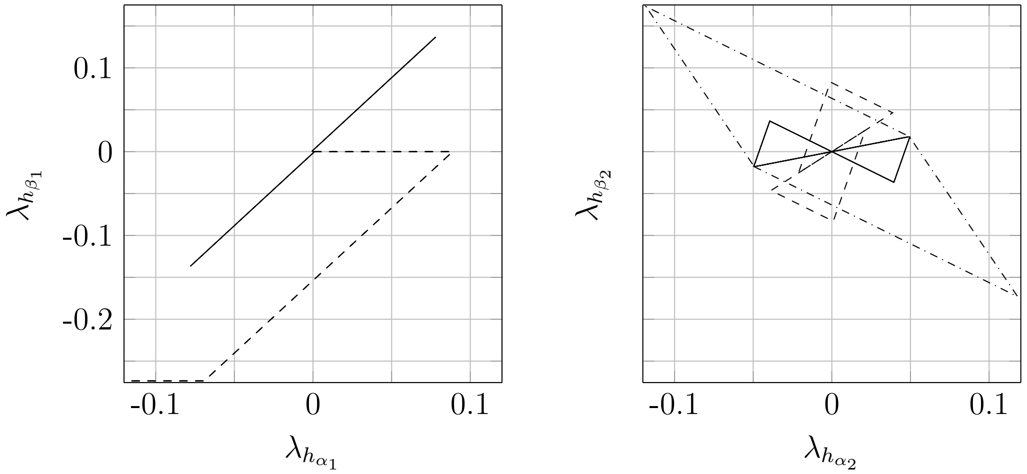

(a) λ_h-trajectories in first subspace. (b) λ_h-trajectories in second subspace.

Figure 6.3: Harmonic flux trajectories for $M = 0.8$ and $\Theta = \frac{\pi}{9}$. Optimized trajectories for $\kappa = \frac{3}{2}$ with vector sequence numbers 2 (dashed line) and 10 (solid line). Standard space vector modulation trajectory as a reference (dashed dotted line).

Nos. 2, 3, 4, 5, 7, and 10. For $\kappa = \frac{3}{2}$, sequences 8 and 9 are added for high modulation index. And for very high induction ratios, $\kappa \to \infty$, sequences No. 7 and 10 do not appear, and the areas of sequences 2 and 3 are very small. As seen in Figure 6.8c, sequences 4, 5, 8, and 9 are dominant in the first sector.

Figure 6.5c depicts the minimum overall distortion values over Θ for $\kappa = \frac{3}{2}$ (optimal six-phase modulation). As seen in the figure, the minimum λ^2_{rms}-values are found at $\Theta = n \cdot \frac{\pi}{3}$ and the maximum values at $\Theta = n \cdot \frac{\pi}{6}$ with $n \in \mathbb{N}$. The standard three-phase SVM shows the same characteristic but in contrast, the overall distortion is increased over the whole range of Θ. Comparing Figures 6.5a and 6.5b, one can conclude that only distortions appearing in the (α_2, β_2) subspace contribute to the overall distortion factor of the standard SVM scheme.

As predicted by Figure 6.3, the optimized six-phase SVM produces very low distortions in the second subspace but an increased value in the first one (compare Figures 6.5b with 6.5a). However, presuming $\kappa > 1$ leads to an improved overall λ^2_{rms}-factor compared with the standard SVM.

The overall performance of a modulator is usually represented by the squared harmonic flux per-fundamental cycle rms value, λ^2_{frms} or in a proportional HDF-value. Both performance criterion are introduced in Section

4.2.3.

The HDF of the optimized modulation strategy and standard SVM can be compared in Figure 6.8. The results with the inductance ratios $\kappa = 1$, $\kappa = \frac{3}{2}$, and $\kappa \to \infty$ are shown in Figures 6.8a, 6.8b, and 6.8c respectively. With $\kappa = 1$ the difference between the two strategies is negligible. Increasing the ratio slightly to $\kappa = \frac{3}{2}$ results in a significant performance improvement as seen in in Figure 6.8b. And the final case of $\kappa \to \infty$ represents the maximum performance gain achievable by the proposed modulation scheme.

6.4 Operation Strategies

The optimization technique of Section 6.3 successfully reduces overall harmonic distortions to a minimal level, but requires a high computational effort. Therefore this strategy can not be implemented on low cost digital signal processors.

The literature [30, 35] presents several modulation techniques which require a lower computational effort. These methods all involve dividing the second subspace (as seen in Figure 6.1b) into smaller triangles (fragments). Each fragment can be represented by one of the voltage sequences from Table 6.1. However, as seen in Figure 6.5, this approach offers lower performance compared to the optimal modulation. An alternative strategy is to interleave the switching signals, which will be discussed in Subsections 6.4.3 and 6.4.4.

The following subsections compare the performance of the standard three-phase SVM with the fragmented and interleaved approach, considering different values of κ and Θ. A good solution must offer a lower calculation effort as well as reasonable performance within a given inductance ratio.

6.4.1 Standard Three-Phase SVM

Because of the machine symmetry, any modulation technique used in three-phase applications may also be used in a six-phase drive. The standard three-phase SVM found in [25, 52] is examined here. This method consists of a sequence including the zero vector $\vec{v}_0$ and the active vectors $\vec{v}_2$ and $\vec{v}_4$ of Figure 6.1. According to Table 6.1, only sequence 1 can be applied, excluding the small and medium vectors. The three remaining duty cycles can be calculated as follows:

$$\begin{bmatrix} d_2 \\ d_4 \\ 2d_0 \end{bmatrix} = \begin{bmatrix} \frac{\pi}{3} & \frac{\pi}{6} & 0 \\ 0 & \frac{\pi}{2\sqrt{3}} & 0 \\ 1 & 1 & 1 \end{bmatrix}^{-1} \begin{bmatrix} v^*_{\alpha_2} \\ v^*_{\beta_2} \\ 1 \end{bmatrix} \tag{6.15}$$

Recall that $\vec{v}_2$ and $\vec{v}_4$ are active in the (α_2, β_2) subspace only, as seen in Figure 6.1. Therefore the overall distortion of this sequence is dependent only on the second subspace and is independent of κ, as seen in Figures 6.5 and 6.8 respectively. This strategy then produces the same HDF characteristics as the SVM for three-phase drives.

6.4.2 Fragmented Sector Mapping

Another way to reduce the complexity is to divide the first sector of the second subspace into four equilateral triangles, or fragments, with a side length of $\frac{\pi}{6}$ as shown in Figure 6.4. Each fragment is assigned to a voltage vector sequence. The chosen sequence must be able to modulate a reference vector which has an endpoint within the fragment area. This approach is similar to the modulation strategy for three-level inverters [52], first used with six-phase drives in [30].

In Figure 6.4 sequences 4, 5, 8 and 9 of Table 6.1 are chosen to fit the optimization for high inductance ratios. By comparing with the bottom row of Figure 6.8c, it is obvious that this fragment mapping closely approximates the optimal sequences for $\kappa \to \infty$. This similarity would predict an HDF function very close to the optimum.

The seven duty cycles are now calculated according to equations (6.2) and (6.3) with the following restrictions:

- Any duty cycle belonging to a vector which is not pointing to a fragment's corner is set to zero.
  For example, in Figure 6.4 the reference vector $\vec{v}_2^*$ will be replicated using sequence 4. In Table 6.1, it can be seen that sequence 4 begins and ends with the zero vector $\vec{v}_0$, which does not contribute to the modulation. Therefore the first and the last elements of the duty cycle vector $\vec{d} = [d_1 \cdots d_7]$ are set to zero.

- Duty cycles which belong to identical vectors in the second subspace (the (a, b) pairs from Figure 6.1) are equal.
  Recalling the example, the second and fifth vectors of sequence 4 are an (a, b) pair, as well as the third and sixth vectors of that sequence. Hence $d_2 = d_5$ and $d_3 = d_6$.

By applying these restrictions, the remaining duty cycles may be estimated by a 3x3 system of linear equations, similar to (6.5). For the example illustrated in Figure 6.4, the result is:

$$\underbrace{\begin{bmatrix} \frac{\pi}{6} & \frac{\pi}{12} & \frac{\pi}{4} \\ 0 & \frac{\pi}{4\sqrt{3}} & \frac{\pi}{4\sqrt{3}} \\ 1 & 1 & 1 \end{bmatrix}}_{\mathbf{A}_{eq}} \cdot \begin{bmatrix} 2d_2 \\ 2d_3 \\ d_4 \end{bmatrix} = \underbrace{\begin{bmatrix} v^*_{2_\alpha} \\ v^*_{2_\beta} \\ 1 \end{bmatrix}}_{\vec{b}_{eq}} \tag{6.16}$$

where the first two lines of matrix $\mathbf{A}_{eq}$ corresponds to the α and β values of the applied sequence in the second subspace, whereas the last line reflects equation (6.4).

If the approach of Section 6.2 for the point- and axial-symmetric sequences is considered, the total volt-seconds over one carrier cycle in the first subspace is zero.

For fragmented sector mapping, the harmonic flux rms is independent of κ in both subspaces, as illustrated in Figures 6.5a and 6.5b. In the second subspace, distortions are close to the minimum and the overall distortion mainly depends on the rms flux of the first subspace and its contribution is expressed by the square of κ.

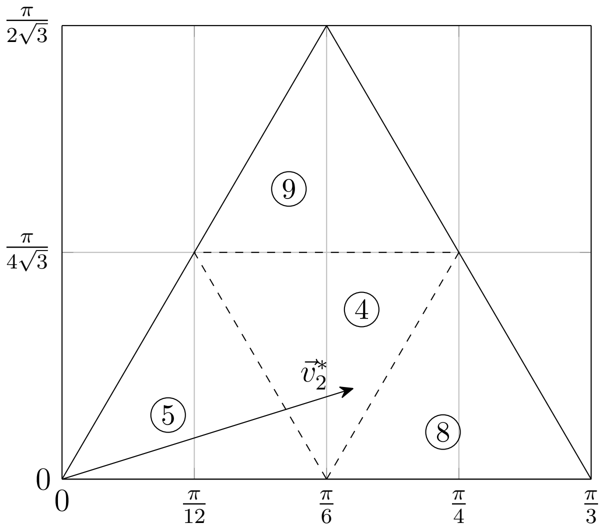

Figure 6.4: Fragmented sector mapping in the first sector of the second subspace. The sector is divided into four fragments, where each is referred to a voltage vector sequence, i.e. reference vector $\vec{v}_2^*$ points to a fragment related to sequence 4.

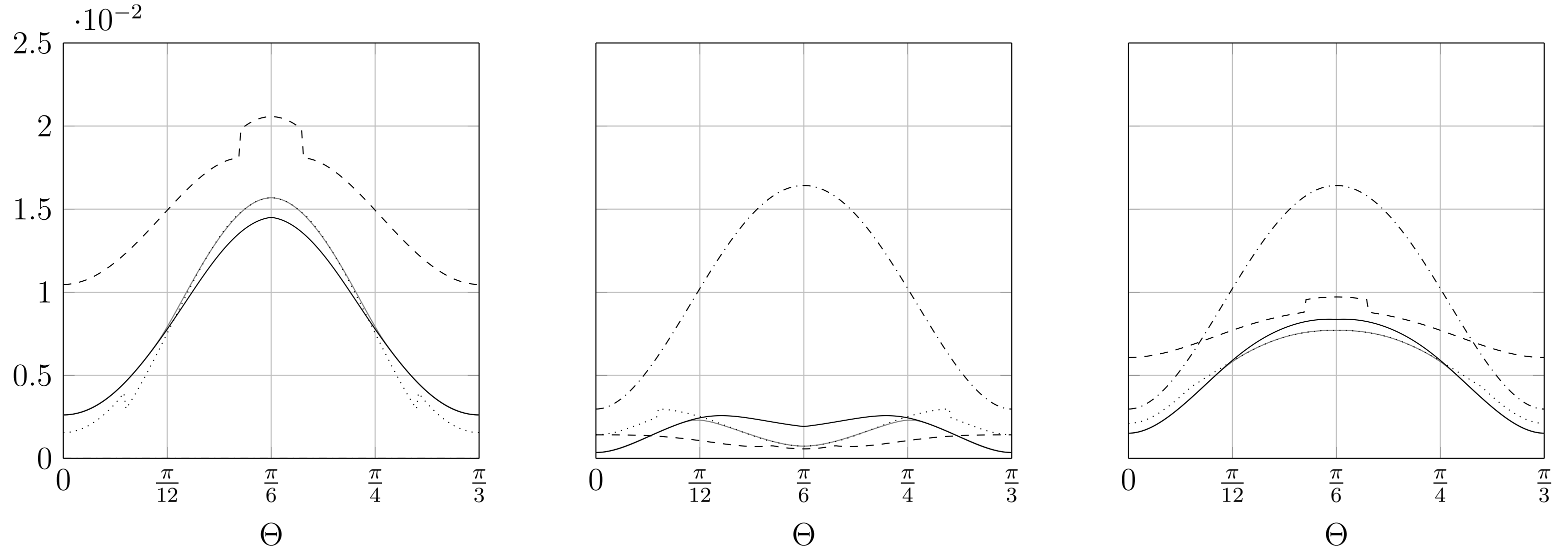

(a) Distortion in (α_1, β_1) subspace: $\lambda^2_{rms_1} = \lambda^2_{rms_{\alpha_1}} + \lambda^2_{rms_{\beta_1}}$

(b) Distortion in (α_2, β_2) subspace: $\lambda^2_{rms_2} = \lambda^2_{rms_{\alpha_2}} + \lambda^2_{rms_{\beta_2}}$

(c) Overall distortion: $\lambda^2_{rms} = \lambda^2_{rms_2} + \frac{\lambda^2_{rms_1}}{\kappa^2}$

Figure 6.5: Overall and decomposed distortion characteristics for several modulation techniques: the standard three-phase SVM (dashed-dotted line), the optimal six-phase modulation (dotted line), the fragmented sector mapping (dashed line), the optimal interleaved (gray solid line) and the approximated interleaved approach (black solid line) [41].

As predicted, the HDF function for $\kappa \to \infty$ is very close to the optimum (see Figure 6.8c). Performance is reduced when $\kappa = \frac{3}{2}$. The overall distortions are increased compared with the optimum, especially for $M > 0.5$. Fragmented sector mapping nevertheless produces fewer distortions than conventional three-phase SVM over the whole modulation range (see Figure 6.8b). Further reducing the inductance ratio to $\kappa = 1$ leads to increased distortion with values equal to the standard SVM for $M < 0.5$, and even higher distortion for any other modulation index, as depicted in Figure 6.8a.

6.4.3 Optimal Interleaved Space Vector Modulation

Another way to control the output is by interleaving the switching signals similar to the optimized carrier-based PWM scheme in Section 5. In this section, however, the shifting between the switching signals must not necessarily be constant over a fundamental period. This extra degree of freedom can result in additional performance gain.

The interleaved approach requires separating the six-phase system into two three-phase systems. Phases a, b, and c are grouped into Set I, while phases x, y, and z are Set II. Both sets are operated as a three-phase system and their output is modulated by a standard continuous SVM scheme, as seen in Section 6.4.1. First, the phase variables $X_a \cdots X_z$ must be transformed according to the double Clarke transformation shown in Section 3.1.1:

$$\left[X_{\alpha_I}\ X_{\beta_I}\ X_{\alpha_{II}}\ X_{\beta_{II}}\right]^T = \mathbf{T_{C2}}\left[X_a\ X_b\ X_c\ X_x\ X_y\ X_z\right]^T \tag{6.17}$$

One advantage of the interleaved approach is that it needs the same computational effort as a common SVM to estimate the duty cycles from the reference vector $\vec{v}^*$, i.e.:

$$\begin{bmatrix} d_2 \\ d_4 \\ 2d_0 \end{bmatrix} = \begin{bmatrix} \frac{\pi}{3} & \frac{\pi}{6} & 0 \\ 0 & \frac{\pi}{2\sqrt{3}} & 0 \\ 1 & 1 & 1 \end{bmatrix}^{-1} \begin{bmatrix} v^*_{\alpha_{I,II}} \\ -v^*_{\beta_{I,II}} \\ 1 \end{bmatrix} \tag{6.18}$$

Additionally, there is an extra degree of freedom for control: the time shift Δd between the pulse patterns of Sets I and II. As explained in Figure 6.6 (top), Δd leads to a time lag of the switching states S_x, S_y, S_z of Set II compared to S_a, S_b, S_c of Set I. This behavior creates an interleaved harmonic flux in both three-phase sets, as shown in Figure 6.6 (bottom).

In order to calculate overall distortion, a relationship between the transformed three-phase sets and the decomposed subspaces must be established. According equation (3.12) the normalized voltages of the first and second subspaces are found with:

$$\begin{bmatrix} v_{\alpha_1} \\ v_{\beta_1} \\ v_{\alpha_2} \\ v_{\beta_2} \end{bmatrix} = \frac{1}{2} \begin{bmatrix} 1 & 0 & -1 & 0 \\ 0 & 1 & 0 & -1 \\ 1 & 0 & 1 & 0 \\ 0 & -1 & 0 & -1 \end{bmatrix} \begin{bmatrix} v_{\alpha_I} \\ v_{\beta_I} \\ v_{\alpha_{II}} \\ v_{\beta_{II}} \end{bmatrix} \tag{6.19}$$

As seen above, the α_1, β_1-entries are achieved by subtracting the α_{II} and β_{II} components from α_I and β_I respectively. In contrast, the α_2, β_2-entries are calculated by the sum of the α_I and α_{II} components, and the negative sum of the β_I and β_{II} components respectively. As a result, if the same pulse pattern is applied for Sets I and II during one switching cycle, the desired result will be achieved: zero volt-seconds in the first subspace.

The overall distortion over a whole switching period is calculated according equations (6.14) and (6.19):

$$\begin{aligned} \lambda_{rms}^2 =& \frac{1}{2} \int_0^2 \left(\lambda_{h_{\alpha_1}}^2 + \lambda_{h_{\beta_1}}^2\right) \frac{1}{\kappa^2} + \lambda_{h_{\alpha_2}}^2 + \lambda_{h_{\beta_2}}^2 dd \\ =& \frac{1}{8} \int_0^2 \left[\left(\lambda_{h_{\alpha_I}} - \lambda_{h_{\alpha_{II}}}\right)^2 + \left(\lambda_{h_{\beta_I}} - \lambda_{h_{\beta_{II}}}\right)^2\right] \frac{1}{\kappa^2} \\ &+ \left(\lambda_{h_{\alpha_I}} + \lambda_{h_{\alpha_{II}}}\right)^2 + \left(\lambda_{h_{\beta_I}} + \lambda_{h_{\beta_{II}}}\right)^2 dd \end{aligned} \tag{6.20}$$

Using $\frac{1}{2} \int_0^2 \lambda_{h_{\alpha,\beta_{II}}}^2 dd = \int_0^1 \lambda_{h_{\alpha,\beta_I}}^2 dd$, the distortion of (6.20) can be rearranged as the sum of Δd-dependent and -independent terms:

$$\begin{aligned} \lambda_{rms}^2 =& \frac{1}{2} \left(1 + \frac{1}{\kappa^2}\right) \underbrace{\int_0^1 \lambda_{h_{\alpha_I}}^2 + \lambda_{h_{\beta_I}}^2}_{\neq f(\Delta d)} dd + \\ & \frac{1}{4} \left(1 - \frac{1}{\kappa^2}\right) \underbrace{\int_0^2 \lambda_{h_{\alpha_I}} \lambda_{h_{\alpha_{II}}} + \lambda_{h_{\beta_I}} \lambda_{h_{\beta_{II}}}}_{= f(\Delta d)} dd \end{aligned} \tag{6.21}$$

On the basis of equation (6.21), three different strategies can be derived in order to minimize overall distortion. Selection of an optimal strategy depends on the inductance ratio κ.

1. $\kappa < 1$ If the first subspace has a lower inductance than the second one, the Δd-dependent term of (6.21) is to be maximized, resulting in:

$$\begin{aligned} \lambda_{h_{\alpha_I}}(d) = \lambda_{h_{\alpha_{II}}}(d) \quad & \text{and} \\ \lambda_{h_{\beta_I}}(d) = \lambda_{h_{\beta_{II}}}(d) \quad & \text{for any } d. \end{aligned}$$

   This is achieved with:

$$\Delta d = 0 \tag{6.22}$$

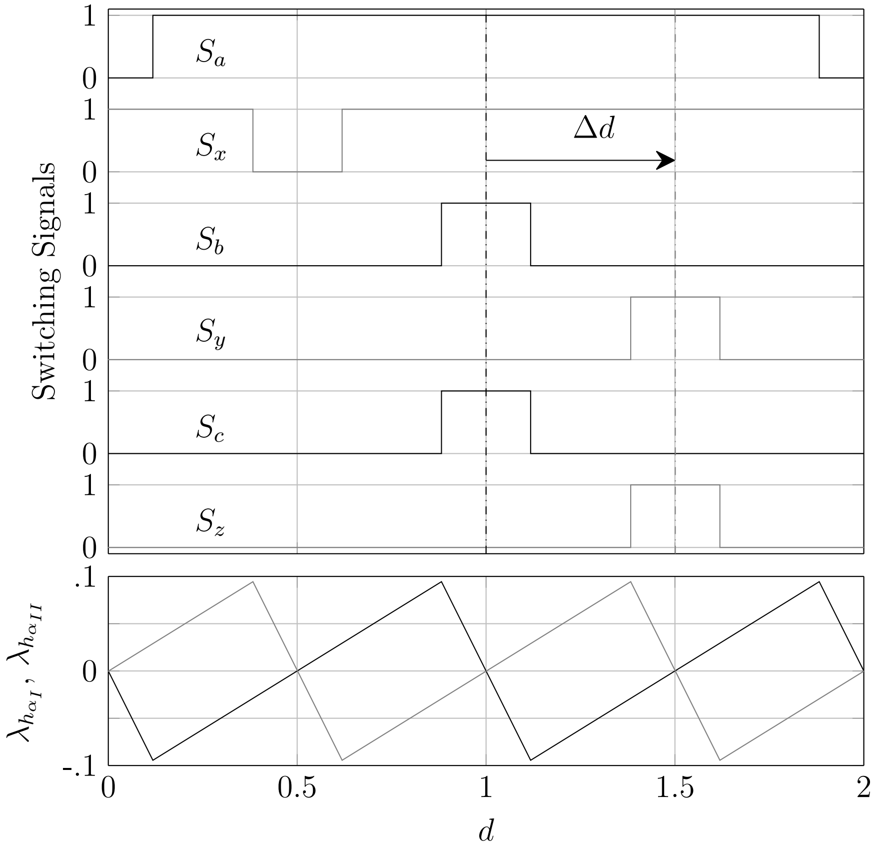

Figure 6.6: Interleaved SVM approach. Top: switching signals $S_a \cdots S_z$ resulting in the voltage vector sequence: $\vec{v}_{1b} \rightarrow \vec{v}_2 \rightarrow \vec{v}_{1a} \rightarrow \vec{v}_2 \rightarrow \vec{v}_{1b} \rightarrow \vec{v}_2 \rightarrow \vec{v}_{1a} \rightarrow \vec{v}_2 \rightarrow \vec{v}_{1b}$. Bottom: harmonic flux of set I (black) and II (gray) in α-direction for $M = 0.8$ and $\Theta = 0$ [41].

Applying (6.22) to (6.21) simplifies the overall distortion equation to be:

$$\lambda_{rms}^2 = \int_0^1 \lambda_{h_{\alpha_I}}^2 + \lambda_{h_{\beta_I}}^2 dd \tag{6.23}$$

As seen in (6.23), λ_{rms}^2 does not depend on κ. Therefore the equation reflects distortions of the second subspace only whereas the first subspace flux harmonics are zero. $\Delta d = 0$ results in the same pulse pattern as the SVM scheme and equal distortion characteristics.

2. $\kappa = 1$: If the inductances are equal, equation (6.21) simplifies to the same value as equation (6.23), but in contrast, the distortions of the first subspace do not have to be zero. Adding the rms harmonic flux of the two subspaces together results in an overall distortion factor which is independent of Δd. The HDF of this approach is presented in Figure 6.8a. As expected, there are no differences as compared to the standard three-phase SVM.

3. $\kappa > 1$: If the inductance of the first subspace is greater than the second one, the Δd-depended term of (6.21) is minimized in order to find an optimal Δd-value:

$$\int_0^2 \lambda_{h_{\alpha_I}} \lambda_{h_{\alpha_{II}}} + \lambda_{h_{\beta_I}} \lambda_{h_{\beta_{II}}} dd \rightarrow \text{Min.} \tag{6.24}$$

The optimal time shift is calculated and depicted in Figure 6.7 with respect to Θ for a range of modulation indices. As seen in the figure, the curves are symmetric about $\Theta = \frac{\pi}{6}$ and the optimal range for the shifting is $0.5 \leq \Delta d \leq 1$. For $\Theta = 0$, the optimal value is $\Delta d = 0.5$ for any modulation index. The same counts for low modulation indices ($M < 0.5$) and arbitrary Θ-angles.

A six-phase system with this control produces an HDF shown in Figure 6.8 for several inductance ratios. For $\kappa \geq 3$, the HDF-characteristic shows slightly worse performance compared to the optimal SVM, especially in a higher modulation range (see Figure 6.8c). For lower ratios ($1 < \kappa < 3$), however, the distortion function shows similar or superior performance compared with the optimal modulation scheme (see Figure 6.8b). This improvement is caused by lower λ_{rms}^2-values around $\Theta = j \cdot \frac{\pi}{3}$ which can be seen in Figure 6.5. Further analysis of the voltage vector applied in this range as done in Figure 6.6 reveals a symmetrical and continuous vector sequence in the (α_1, β_1) and (α_2, β_2) planes. However, a zero vector is not present in the sequence. Thus it is not considered for optimization as explained in Section 6.2.

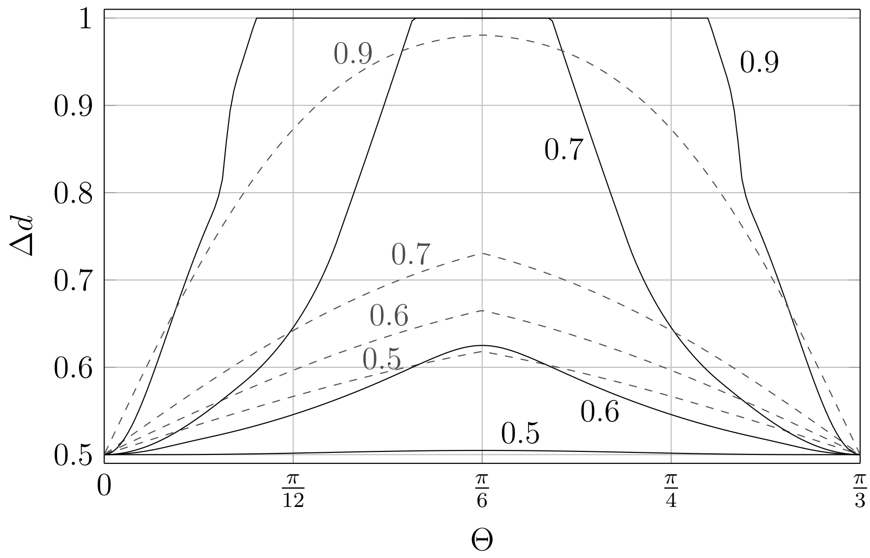

Figure 6.7: Optimal (solid lines) and approximated (dashed line) Δd characteristics for different modulation indexes [41].

In order to reach an optimal solution for Δd using the interleaved approach, equation (6.24) must be solved numerically. Compared with the optimization approach of Section 6.3, an adequate result is possible with fewer calculation steps for two reasons:

1. Only one sequence is evaluated.

2. The optimization problem is scalar, rather than multidimensional.

For ease of implementation, the optimal values of Δd might be calculated offline and stored in a look-up table.

6.4.4 Approximated Interleaved Space Vector Modulation

Another way of estimating the proper time shift can be achieved by approximation of the optimization function. This approach results in less-precise but online calculable Δd-values. Its equation is derived here in closed-form.

Because the $\Delta d\,(\Theta)$ curves are symmetrical towards $\frac{\pi}{6}$, only the range $\Theta \in \left[0, \frac{\pi}{6}\right]$ must be evaluated to find the optimal value (see Figure 6.7). In this range, comparing the harmonic flux in the α and β-directions, one can assume that for any d the α distortions are greater than the β-distortions.

Therefore it is considered:

$$\lambda_{h_{\beta_I}} = \lambda_{h_{\beta_{II}}} \approx 0 \tag{6.25}$$

The optimization problem for equation (6.24) can then be simplified to:

$$\int_0^2 \lambda_{h_{\alpha_I}} \lambda_{h_{\alpha_{II}}} dd \rightarrow \text{Min.} \tag{6.26}$$

For example, the trajectories of the optimal time-shifted $\lambda_{h_{\alpha_I}}(d)$ and $\lambda_{h_{\alpha_{II}}}(d)$ are given in Figure 6.6 for $\Theta = 0$. It can be seen that the shift of $\lambda_{h_{\alpha_{II}}}$ means that the product $\lambda_{h_{\alpha_I}} \lambda_{h_{\alpha_{II}}}$ becomes negative for any d. Thus the optimal time shift will be a quarter wave or $\Delta d = 0.5$

Generally, the optimal value of Δd is located where the negative quarter wave of $\lambda_{h_{\alpha_I}}$ for $d > 1$ overlaps the positive quarter wave of $\lambda_{h_{\alpha_{II}}}$. Therefore, the following approximation can be made for Set I:

$$\lambda_{h_{\alpha_I}} (1 + \Delta d) = \int_1^{1+\Delta d} v_{k_{\alpha_I}} - M \cos{(\Theta)} \, dd = 0 \tag{6.27}$$

where $v_{k_{\alpha_I}}$ is the α-element of the k-th voltage vector as used in equation (6.18) with $k \in \{0, 2, 4\}$. Equation (6.27) can then be written as follows:

$$\int_{d_0}^{d_0+d_4} \frac{\pi}{6} dd + \int_{d_0+d_4}^{\Delta d} \frac{\pi}{3} dd - \Delta d \cdot M \cos{(\Theta)} = 0 \tag{6.28}$$

which yields an explicit solution for the time shift:

$$\begin{aligned} \Delta d &= \frac{\pi \left(2d_0 + d_4\right)}{2\pi - 6M \cos{(\Theta)}} \\ &= \frac{1}{2} + \frac{\sqrt{3}}{2} \frac{M \sin{(\Theta)}}{\pi - 3M \cos{(\Theta)}} \end{aligned} \tag{6.29}$$

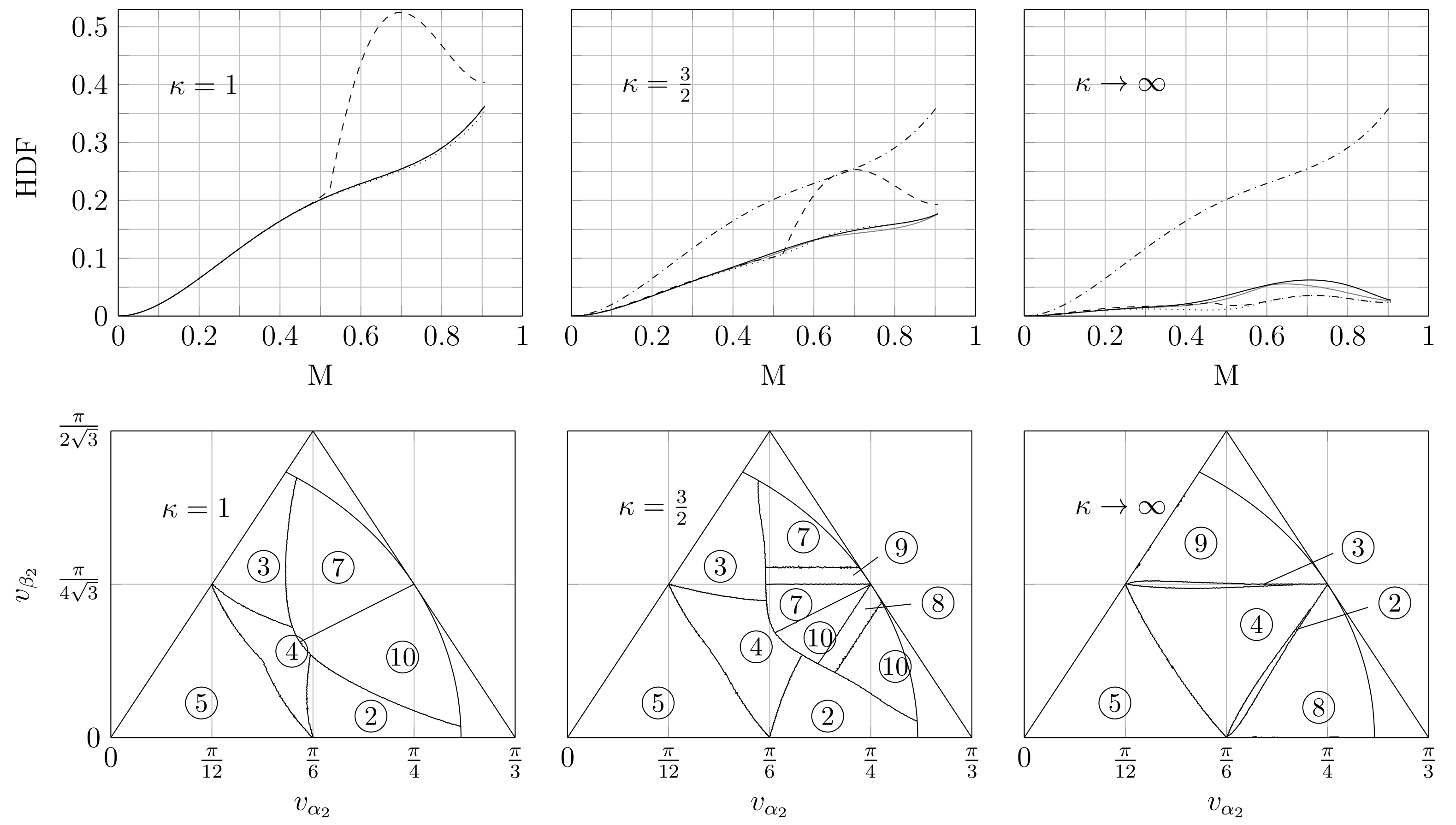

Figure 6.8: Top: HDF for different inductance ratios and modulation techniques: standard SVM (dashed-dotted line), optimal six-phase modulation (dotted line), fragmented sector mapping (dashed line), optimal interleaved (gray solid line), and approximated interleaved approach (black solid line). Bottom: Optimal sequences [41].

Figure 6.7 depicts the approximate $\Delta d(\Theta)$ characteristic for several values of M. Small but acceptable performance losses occur if the HDF curve is under scope, due to the differences between the approximate and optimized values of Δd (see Figure 6.8). As a result of the approximation, lower λ^2_{rms} values appear near $\Theta = \frac{\pi}{6}$ in the first subspace, and higher values appear in the second subspace (compare Figures 6.5a and 6.5b respectively). The result produces slightly poorer overall performance in Figure 6.5c.

6.5 Experimental Results

A fundamental frequency of $f_0 = 66Hz$ was chosen and fixed during operation, so that current distortion could be estimated with respect to changes in modulation index M only. Over several fundamental cycles the harmonic current I_h based on equation (4.37) was estimated. The lower frequency f_l was chosen to be 8 times the fundamental frequency, in this case $f_l = 528Hz$. The upper frequency was set as $f_u = 125kHz$. Finally, switching frequency was set to $f_s = 3kHz$.

Figure 6.9 shows the experimental results for the inductance ratios $\kappa \approx 1$ and $\kappa >> 1$. First compare the theoretical plot of Figure 6.8a with the experimental result in Figure 6.9a. As predicted, fragmented sector mapping achieves poor results for $M > 0.5$. Meanwhile, the optimal and approximated interleaved approaches produce almost identical results. The standard SVM in reality is not exactly equal to the two interleaved strategies, however the difference is very small.

Next, compare Figures 6.8c and 6.9b. The experiment shows that for high inductance ratios, fragmented sector mapping achieves superior performance over the whole modulation range. This result is expected because at high κ, the chosen fragments closely match the optimal sequence map. In contrast, the interleaved modulation strategies show comparable but slightly poorer performance, as predicted for $\kappa \to \infty$. Finally, the standard SVM approach produces high distortion and shows the worst performance of all the strategies.

Figure 6.10 shows the current waveforms for three modulation strategies with a given modulation index. By comparing Figures 6.10a and 6.10b, one can observe that the interleaved and fragmented sector mapping approaches achieve a significant reduction in distortion when κ is increased. But the standard SVM shows the same performance for both cases.

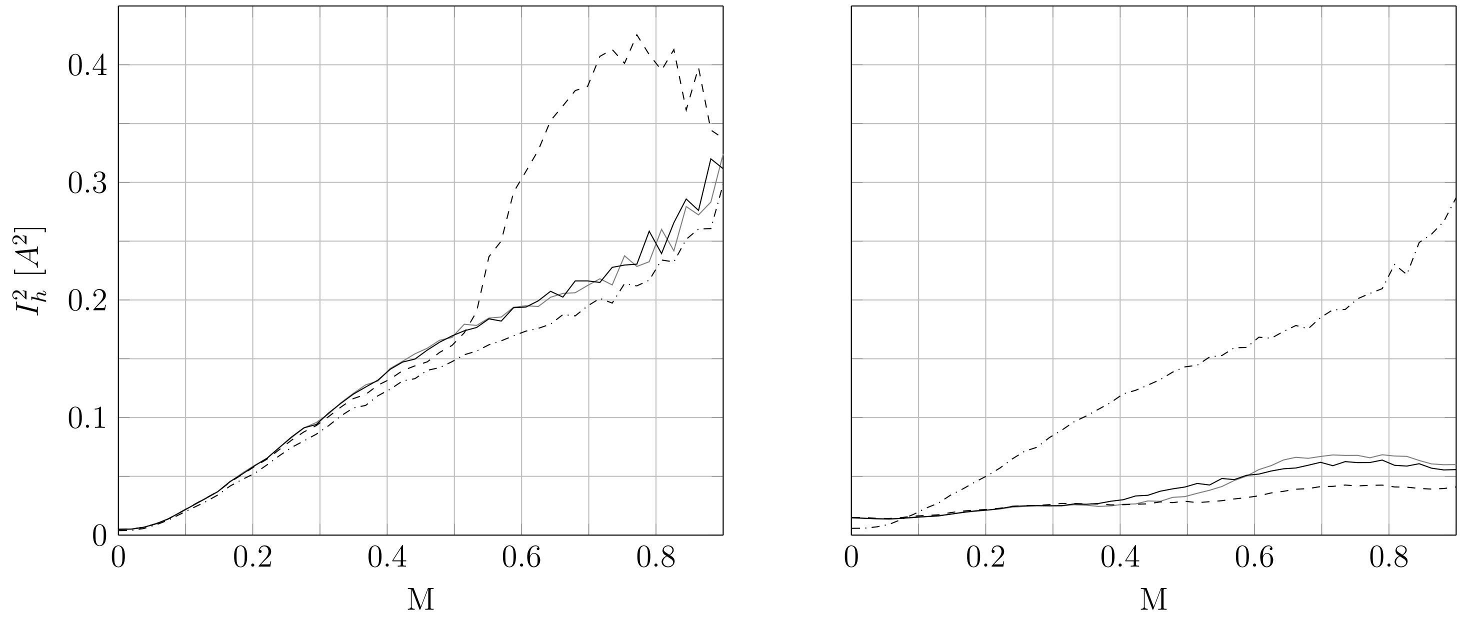

(a) With $\kappa = \frac{18}{19} \approx 1$

(b) With $\kappa = \frac{180}{19} >> 1$

Figure 6.9: Harmonic current for different operation strategies: the standard three-phase SVM (dashed-dotted line), the fragmented sector mapping (dashed line), the optimal interleaved (gray solid line) and the approximated interleaved approach (black solid line) [41].

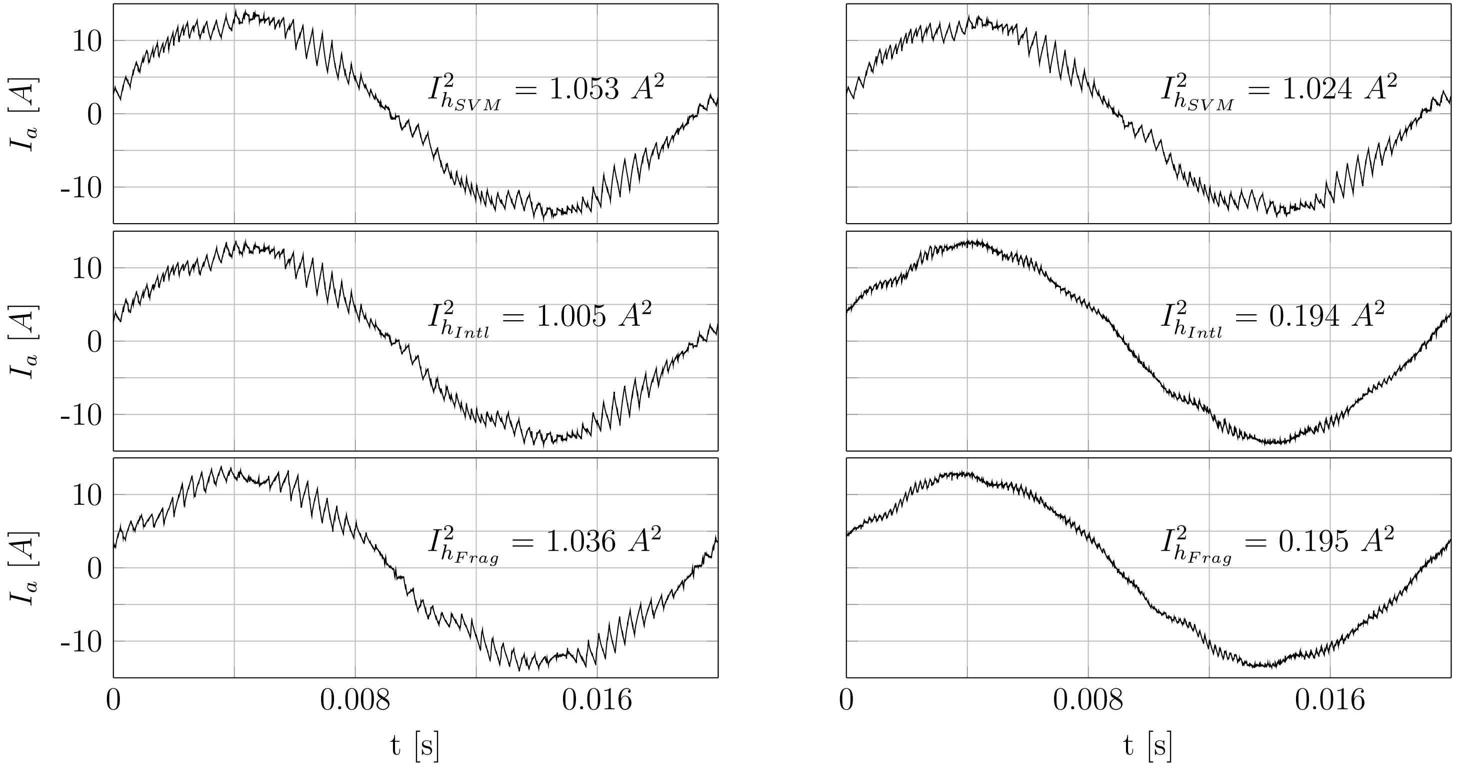

(a) With $\kappa \approx 1$

(b) With $\kappa >> 1$

Figure 6.10: Current waveforms over one fundamental cycle with $M = 0.8$ for different operation strategies and under nominal conditions: the standard three-phase SVM (top), the approximated interleaved approach (middle) and the fragmented sector mapping (bottom) [41].

Chapter 7

Torque Ripple and Efficiency Observations

In the previous sections, several modulation strategies were proposed which are capable of reducing the current distortions of a symmetrical six-phase drive. The distortions are a inevitable negative side-effect of VSI-driven electrical drives which causes vibrations, noise and power losses.

For a deeper investigation of those negative effects, this section analyzes the influence of the discussed modulation strategies on machine torque ripples and overall drive efficiency. To do so, the test rig shown in Figure 3.10 was prepared with corresponding sensors to measure the desired magnitudes. The so achieved values depend on several parameters such as machine and inverter design and thus, the experimental results may vary with different equipment.

Section 7.1 describes the method for measuring the torque ripples of the machine, which is achieved by sensing the acceleration of the casing. The experimental data is compared with rms current in the q-direction, where similarities are found.

The efficiency of the drive setup over the whole range of operation is examined in Section 7.2. There, it is shown that a significant improvement is achievable for high inductance ratios.

7.1 Torque Ripple

Torque ripples describe a periodic increase and decrease of the machine's output torque compared to its average value. Those pulsating ripples can be caused by several effects such as [91]:

- Mechanical imbalances, e.g. eccentricity of the rotor shaft

- Slight asymmetries in the magnetic field and/or windings
- Variation in reluctance over the circumference (cogging torque), i.e. a non-constant air gap
- Interaction between MMF and air gap flux harmonics
- Distortions in stator and/or rotor current

Assuming an idealized i.e. symmetrical machine design with a constant air gap and zero MMF harmonics, the ripples are mainly determined by the high-frequency distortions of the stator current. As shown in Section 4.2.3 the distortions can be decomposed into a d-component which is parallel to the mutual flux, and a perpendicular q-component. Because the q-axis represents the torque generating component of current, the rms of torque harmonics must be proportional to the mutual flux magnitude and λ_{rms_q}. As shown in Figure 4.7b the current harmonics are not constant over Θ and do not depend proportionally on the overall harmonic flux (compare with Figure 4.7a).

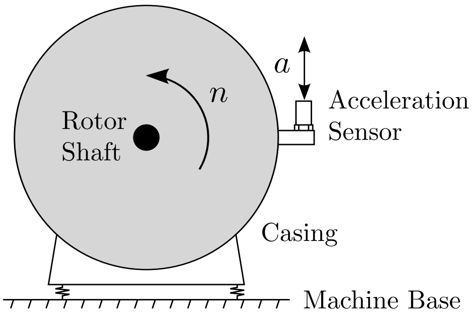

Figure 7.1: Experimental setup for measuring torque ripples of the machine through tangential accelerations of the casing.

Setting the mutual flux magnitude constant during operation must lead to an rms value of torque ripples proportional to the fundamental rms harmonic flux λ_{frms_q} as depicted in Figure 4.9. The experimental results shown here are achieved with a constant rotational speed n and a variation of the modulation index M. Constant speed offers the advantage of a constant n-dependent parasitic torque effect, e.g. through periodically varying bearing friction.

Doing so, the EMF can be assumed as proportional to the mutual flux or proportional to M. For the ease of comparison with the experimental data in Figure 7.2 the theoretical rms-ripple $M \cdot \lambda_{frms_q}$ is therefore added.

As shown in the figure, the SVM is expected to offer the poorest performance of all modulation techniques applied. The interleaved PWM performs better than the SVM but shows poorer results than the approximated interleaved SVM and the fragmented sector mapping technique.

The torque ripples were experimentally gathered with the test setup of Figure 7.1. A piezo-electric sensor mounted on the machine casing measures the tangential acceleration of the machine. Since the attachment of the casing towards machine basement is not infinitely stiff, a rotational movement and acceleration around the rotor shaft is made possible and the torque ripples can be gathered indirectly.

The rms value of acceleration was measured analogously to the harmonic current in equation (4.37). To avoid any low-frequency side-effects, e.g. due to slotting or unequal air gap, the lower frequency f_l was set to 1kHz and the upper one to $10kHz$.

The bottom of Figure 7.2 summarizes the results for the prediscussed modulation techniques. As expected, the SVM offers the poorest performance and the interleaved PWM performs better than the SVM over the whole modulation range. Interleaved SVM and fragmented sector mapping are the preferable choices. They show nearly the same and superior performance over all modulation strategies with a slight advantage for the interleaved approach.

From an overall point of view the calculations match well with the experimental results. For high modulation index there are certain differences detectable and in spite of the simulations, the interleaved SVM offers superior performance in that range.

The previously discussed simulations and experimental results are achieved by setting the average load torque to zero. In this case, the modulation index applied is equal to the magnitude of mutual flux times the rotational speed and the machine model simplifies to a strictly inductive load.

Further measurements extending the scope of view to the whole operation range, i.e. from zero to nearly nominal torque and speed at constant mutual flux results in three-dimensional diagrams as shown in Figure 7.3. The improvements in torque ripples comparing the standard SVM and the approximated interleaved SVM are depicted there by the means of the relative torque ripple difference factor a_{rel}:

$$a_{rel} = \left(\frac{a_{ISVM}}{a_{SVM}} - 1 \right) \times 100\% \tag{7.1}$$

where a_{SVM} and a_{ISVM} represents the rms-values of acceleration for the standard SVM and interleaved SVM respectively.

As seen in Figure 7.3a for a nearly unity inductance ratio there are fewer ripples and therefore negative a_{rel}-values achievable over a wide operation range. There are up to -40% rms-accelerations detectable compared to the

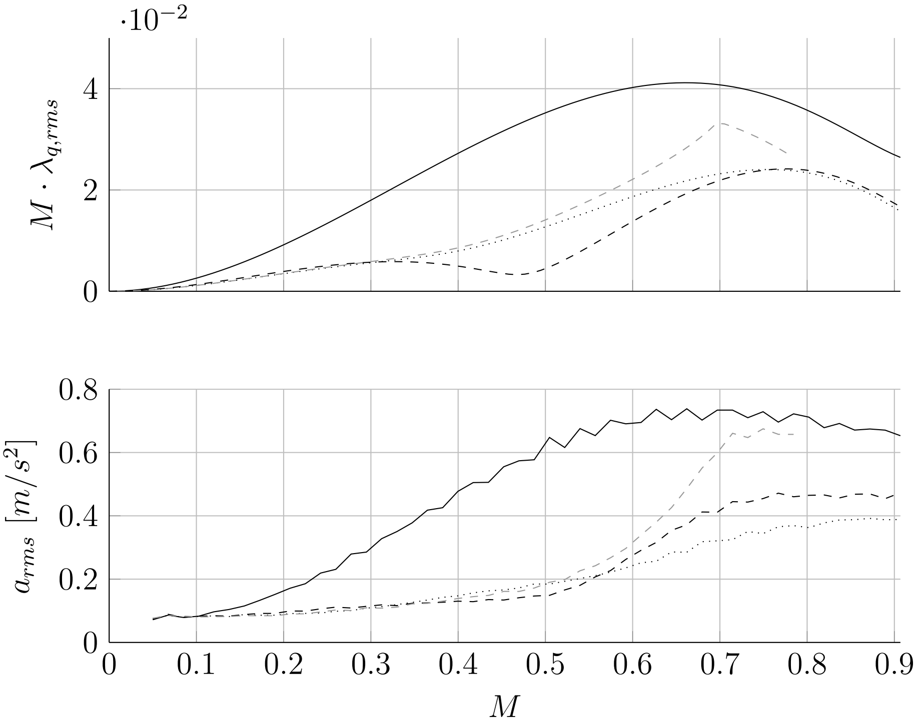

Figure 7.2: Torque ripple analysis for $\kappa >> 1$ applying the SVM (solid line), interleaved PWM (gray dashed line), fragmented sector mapping (black dashed line) and approximated interleaved SVM (dotted line). Top: theoretical results gained from the q-component of the frms harmonic flux. Bottom: experimental rms-data from the acceleration sensor between 1-10 khz.

standard SVM for high torques and low speeds. For high speeds and low torque values, however the interleaved SVM produces more rms-ripples of up to +40%.

For high inductance ratios $\kappa >> 1$ the reductions in acceleration are notable over the whole range of operation (see Figure 7.3b). The improvements achieved here lie between -20% for nominal speed and torque conditions and -70% for the mid-speed range.

7.2 Efficiency Analysis

The efficiency of a system η in general is defined as the ratio of output to input power. Input and output are usually specified from the energy flow point of view. In the case of a motor drive system the input power is defined as the electric DC-power and the output power as the mechanical energy flow at the rotor shaft. For a drive system working in generating mode, the energy flow reverses and the denotations of input and output are interchanged.

In steady state operation, $|P_{out}|$ is less than or equal to $|P_{in}|$, such that η ranges between 0 and 1. The difference between the input and output power, the power loss, thus plays an important role for the efficiency calculation. The total loss is defined as $P_{loss} = P_{in} - P_{out}$ and η becomes:

$$\eta = \frac{P_{out}}{P_{in}} = 1 - \frac{P_{loss}}{P_{in}} \tag{7.2}$$

The power losses of a drive system come from the inverter and machine side, i.e. $P_{loss} = P_{loss,inv} + P_{loss,mac}$. The precise estimation of $P_{loss,inv}$ is complex and not elaborated here. But the main influence factors are [104]:

- on and off switching behavior of semiconductor devices
- conduction characteristics
- supplementary equipment

The switching losses are based on the finite turn-on and turn-off duration of the switching devices due to the constant DC-voltage and a non-zero current flow. This type of losses can be seen as proportional to the switching frequency f_s and the current flow through the devices. Conduction losses occur during on-duration of the switching devices and at the free-wheeling diodes of the power circuit. These losses are equal to the current flow through the device times the nearly constant forward voltage drop. Additional inverter equipment such as micro-controller, gate driver, and sensor circuits cause supplementary losses, which can seen as constant during operation.

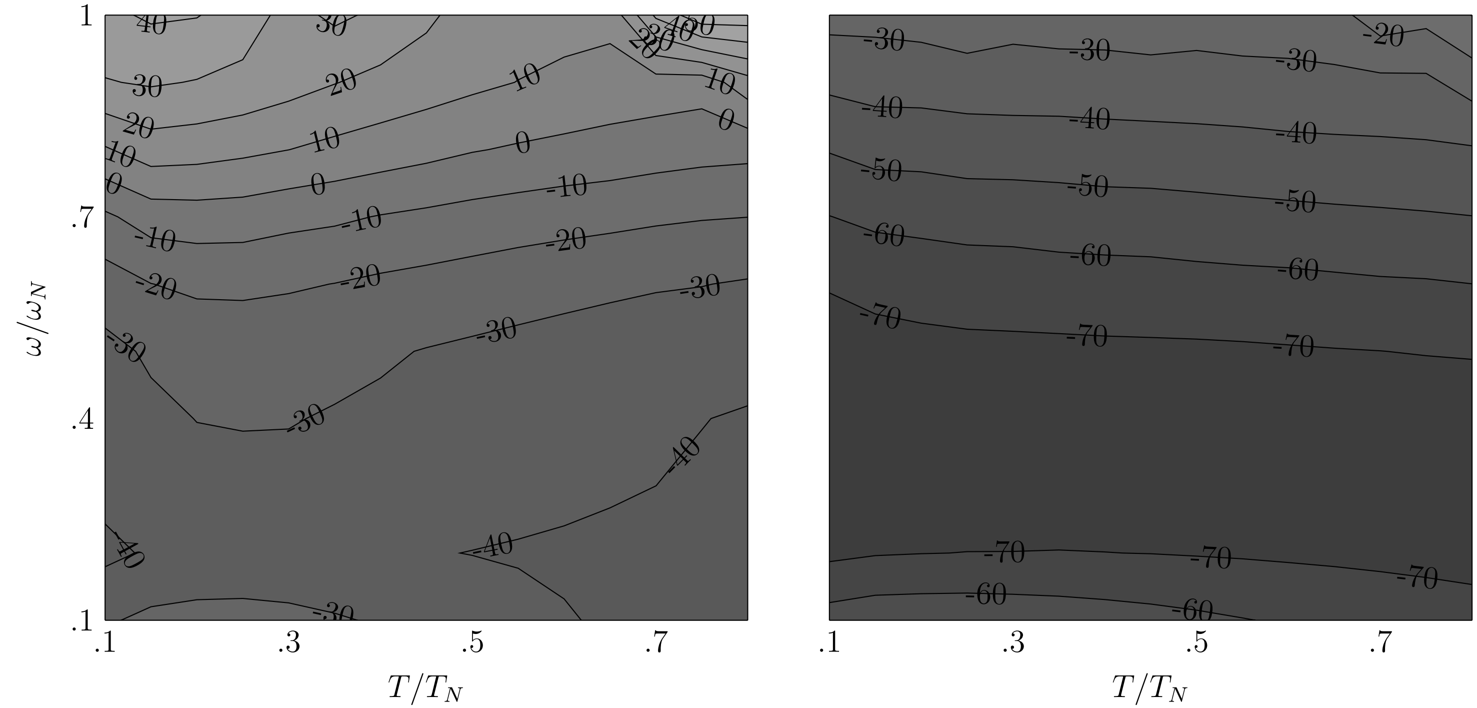

(a) Without transformer ($\kappa \approx 1$).

(b) With transformer ($\kappa >> 1$).

Figure 7.3: Experimental results: relative torque ripple difference a_{rel} dependence over normalized load T/T_N and speed ω/ω_N applying the approximated interleaved SVM.

The machine based power losses $P_{loss,mac}$ are caused by [91]:

- ohmic behavior of windings
- reversal of magnetism (hysteresis and eddy current effects)
- mechanical friction
- additional effects

The ohmic losses of the stator and rotor windings are usually the core part of $P_{loss,mac}$. Its value is equal to the resistance of the windings times the squared rms-current flowing through the wires.

The hysteresis curve of the ferromagnetic material (magnetization against magnetic field) and the design dependent eddy currents determine the losses caused by the alternating magnetic field. The first factor is linear and the second one squared proportional to the current.

Mechanical friction sums up every resistive behavior depending on the rotational speed of the machine, i.e. bearing and air friction. Losses which are measurable but can not be classified according to the aforementioned categories may be grouped in the additional effects category. These effects are usually small compared to the other listed ones and can be neglected for a rough estimation.

The optimized modulation strategies derived in sections 5 and 6 lead to a reduced current distortion in the six phases of the drive setup for $\kappa > 1$. Consequently, a positive effect on the drive efficiency might be detectable via the reduced inverter and machine power losses.

On the inverter side lower conduction losses are expected, whereas on the machine side a smaller ohmic voltage drop and a lower hysteresis as well as eddy current loss effect may occur.

With the test equipment of Figure 3.10, three different experiments were carried out measuring the overall efficiency. First, the standard SVM for three drives was applied according section 6.4.1. Second, the optional transformer was connected between machine and inverters and the aforementioned test was repeated with the same modulation technique. Third, the approximated interleaved SVM of Section 6.4.4 was implemented and tested with the modified test rig.

According to equation (7.2) the efficiency is calculated with the DC-Link voltage and current: $P_{in} = U_d \cdot I_d$. The output power is estimated with the load torque and mechanical speed: $P_{out} = T \cdot \omega$.

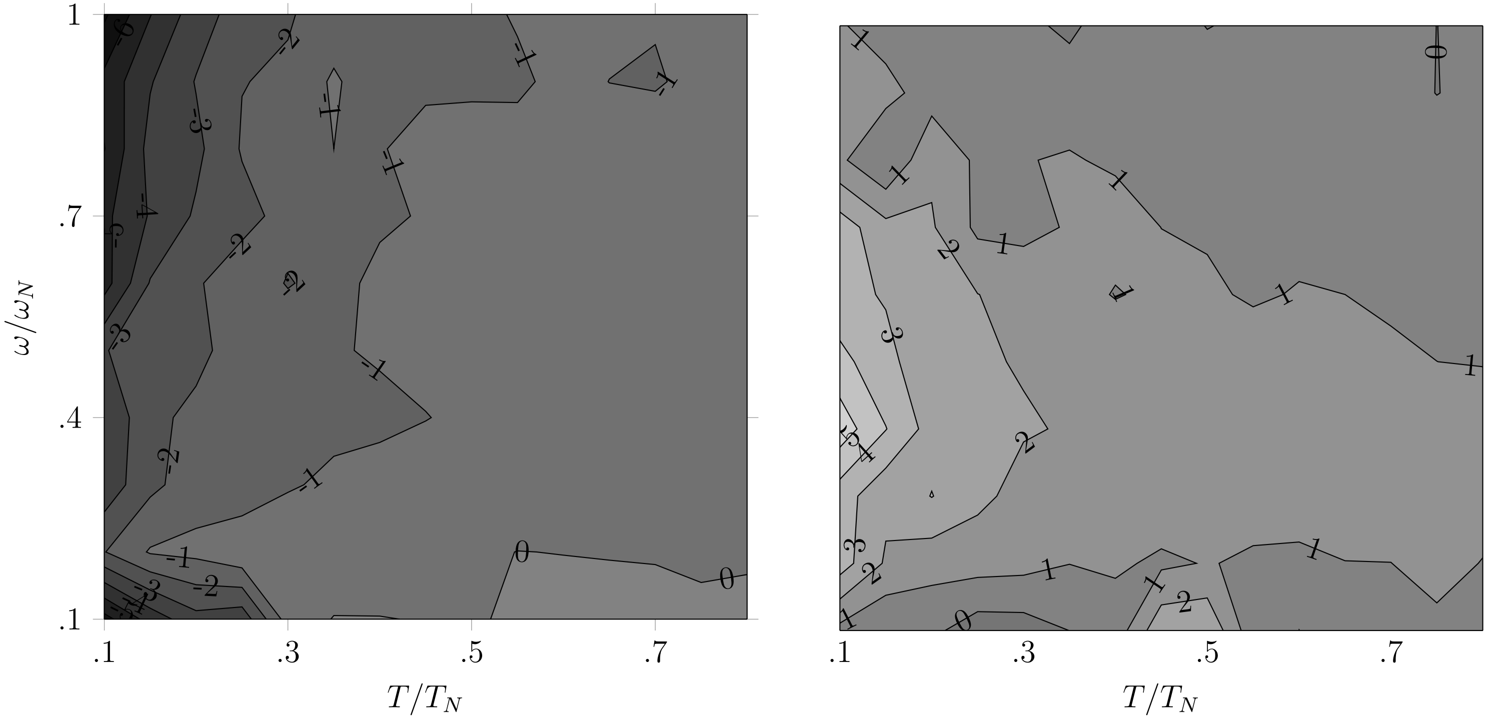

(a) Standard three-phase SVM ($\eta_{rel_{SVM}}$).

(b) Approximated interleaved SVM ($\eta_{rel_{ISVM}}$).

Figure 7.4: Experimental results: relative efficiency difference dependence over normalized load T/T_N and speed ω/ω_N with transformer ($\kappa >> 1$).

For ease of comparison, the efficiencies of the test applying standard SVM or interleaved SVM with transformer ($\eta_{SVM_{\kappa>>1}}$ and η_{ISVM}) are related to the results without transformer ($\eta_{SVM_{\kappa\approx 1}}$), i.e.:

$$\begin{aligned}\eta_{rel_{SVM}} &= \left(\frac{\eta_{SVM_{\kappa>>1}}}{\eta_{SVM_{\kappa\approx 1}}} - 1\right) \times 100\% \\ \eta_{rel_{ISVM}} &= \left(\frac{\eta_{ISVM}}{\eta_{SVM_{\kappa\approx 1}}} - 1\right) \times 100\% \qquad (7.3)\end{aligned}$$

As seen in Figure 7.4a, the additional transformer reduces the efficiency over the whole operation range as far as the same unoptimized modulation technique is applied. This behavior is expected, since slightly increased ohmic, hysteresis and eddy current losses are caused by the optional equipment.

If the optimized approximated interleaved SVM is employed, the efficiency increases as shown in Figure 7.4b. The extra losses caused by the transformer are overcompensated by the reduced current distortions and their dependent loss effects. As seen there, over the whole operation range $\eta_{rel_{ISVM}}$ is greater than or equal to zero.

Chapter 8

Conclusion and Outlook

Multiphase drives are a competitive alternative for high power medium voltage applications. Compared to any other common topology, such as multilevel, parallel inverter or open end winding drives, the multiphase structure combines a relatively low cost to power ratio with a fault tolerant inverter and machine design. Furthermore, there are current or voltage sharing capabilities between several inverters. This thesis focused on symmetrical six-phase drives, a subset of multiphase drives, which incorporates a favourable winding design and phase layout for reduced current distortions.

The basis of an optimal operation strategy for the drive is the understanding and proper modeling of the machine and inverter behaviour. In the text, two different transformation techniques were introduced, which facilitates the understanding of the setup. First, the common Clarke-transformation was applied two times on the six phases. As a result, the system complexity is reduced from order six to four. The system states are mapped onto two planes I and II, which do not represent any physical meaning but are important for several of the inverter modulation strategies.

Second, a decomposition technique was introduced, which maps the machine and inverter states onto two independent planes, 1 and 2. The transformation technique decomposes the time and space dependent variables according to their harmonic order content. Uneven harmonics, i.e. 1st, 5th, 7th, ... are mapped onto the first plane, whereas even harmonics, i.e. 2nd, 10th, 14th, ... are mapped onto the second plane. Depending on the winding design, the machine is able to be operated in either one of the two planes.

According to the decomposition theory, the six-phase machine was modeled as a conjunction of two independent subsystems, each represented by mathematical equations known from common three-phase drives. The determinative parameter for the high frequency behaviour of a machine is the leakage inductance corresponding to the subsystems of each plane (1,2) and the ratio of the parameters, represented by κ. Without any additional equipment the machine described in the text exhibits a ratio of one. With an optional transformer between inverter and machine, κ increases significantly, which causes a higher damping of phase current in the first subsystem. Corresponding high frequency equivalent circuits of the machine were given.

The inverter switching states were described with 64 different voltage vectors, mapped onto both decomposed planes. The outer vectors describe a hexagon as seen in three-phase inverters. Applying an active voltage vector onto the machine produces either a zero or an active voltage vector on the opposite plane. A proper voltage vector sequence is therefore necessary in order to produce a desired waveform in one plane and to avoid distortions caused by the switching in both planes.

Two different analyzing methods were given in the text, both capable of estimating the phase current distortions of the machine. The first one, double Fourier integral analysis, was derived for a single phase load and certain sampling techniques, i.e. the natural, symmetrical, and asymmetrical regular sampling. The method is applicable even for low switching frequencies but is restricted to carrier based sampling. The second method, harmonic flux analysis, was derived for a three-phase inductive load. This method allows arbitrary switching sequences to be analyzed but with a restricted pulse ratio. The technique also enables the determination of torque ripples, which are caused by distortions.

Applying the common synchronized pulse width modulation techniques with a sinusoidal reference and a triangle carrier signal on the two three-phase sets offers an additional degree of freedom for control: the phase offset angle Θ_c between the carrier waveforms. It was shown that this interleaved approach can have a significant influence on the phase current distortions. For values $\kappa > 1$, there exists an optimal Θ_c, which minimizes the distortions for a certain amplitude of the reference waveform M. The optimal values $\Theta_c(M)$ were derived numerically for the aforementioned sampling techniques and an analytical approximation for real-time applications was given. The approximation shows very good performance in simulations as well as experiments. For $\kappa < 1$, the optimal offset is $\Theta_c(M) = 0$ and for $\kappa = 1$ the distortions are independent of Θ_c, as derived mathematically.

The space vector modulation for the six-phase drive offers the huge amount of $6!^2 = 518400$ different continuous sequences during a switching cycle. It was shown how to classify the voltage space vectors for a certain sector, which reduces the number of relevant switching states to 16 and corresponding sequences to 11. For a certain reference voltage and inductance ratio, an optimization was carried out in order to find the sequence and duty cycles which reduce the harmonic flux distortions to a minimum. The definitions of the offline optimization were given, including constraints and cost function. The results show that notable improvements can be achieved if $\kappa > 1$. On the basis of the optimization, different operation strategies were derived: the standard three-phase SVM, the fragmented sector mapping, and the interleaved SVM. The standard SVM shows the same performance as for three phase drives and for any value of κ. The fragmented sector mapping shows very good performance for $\kappa >> 1$ but poor results for $\kappa \approx 1$.

The basis of the interleaved approach is again a standard three-phase modulation (here: SVM) and a time shifting of the switching signals towards the other three-phase set. An optimal shift value was derived through numerical calculations. On the basis of these equations, an analytical approximation was achieved. The performances of both interleaved approaches are comparable, as shown in simulations and experiments. In the range of $1 < \kappa < 2$, this strategy offers superior results with low implementation effort.

Current distortions cause audible vibration and increase the machine power losses. Both unwanted effects can be reduced by applying the operation strategies proposed before. As shown with simulations and experiments, vibrations can be reduced significantly in the low and mid modulation or speed range. Improvement is achievable for any value of κ, but higher values increase the positive effect.

Compared to the standard modulation method, the efficiency of the experimental test drive could be improved over the whole speed and torque range. Even with the additional transformer, which increases the phase resistances, the additional losses were overcompensated by the performance gain. Efficiency improvements of up to 5% were measured.

The results of this thesis demonstrated the potential of symmetrical six-phase drives. Further studies, however, might be necessary in order to gain more knowledge about a proper drive setup and derive further strategies for control. The following suggestions might be useful for the interested researcher and hopefully create new ideas.

First, a different way of increasing the inductance ratio has to be found. Rather than adding the transformer between inverter and machine a different layout of the windings might be a solution. For an asymmetrical machine, different designs are deeply studied in [47] and their contribution to the leakage inductances are illustrated there. The procedure should be applicable on symmetrical machines in order to find an optimal design and eliminate additional equipment.

Second, different modulation strategies might be analyzed for further improvements. In particular, discontinuous modulation schemes and optimal pulse pattern for arbitrary inductance ratios could be in the scope. The achievable performance, however, is always expected to be better than the corresponding three-phase two level scheme and worse than or equal to the corresponding three-level NPC approach.

Third, although the literature is rich in modulation strategies for asymmetrical six-phase drives, a direct comparison with the symmetrical counterpart is still missing. Due to the unfavorable ratio of leakage inductances, the stator phase distortions of the asymmetrical machine are expected to be worse than the ones of the symmetrical type. It might be interesting to see if these differences are compensated through the ability to avoid certain spacial flux harmonics and corresponding rotor current distortions.

Appendix A

Test Bench

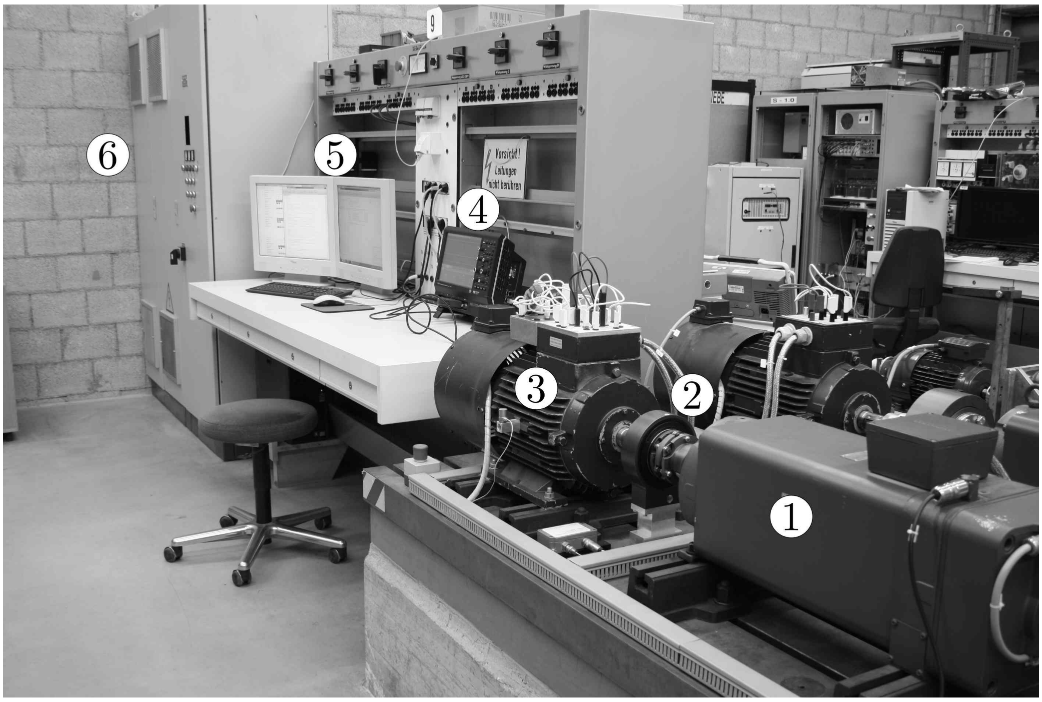

Figure A.1: Overview of the test bench with load machine ①, torque transducer ②, six-phase machine ③ with acceleration sensor, oscilloscope ④ for high frequency and high resolution measurements, PC-system ⑤ for programming and visualization, and control cabinet ⑥.

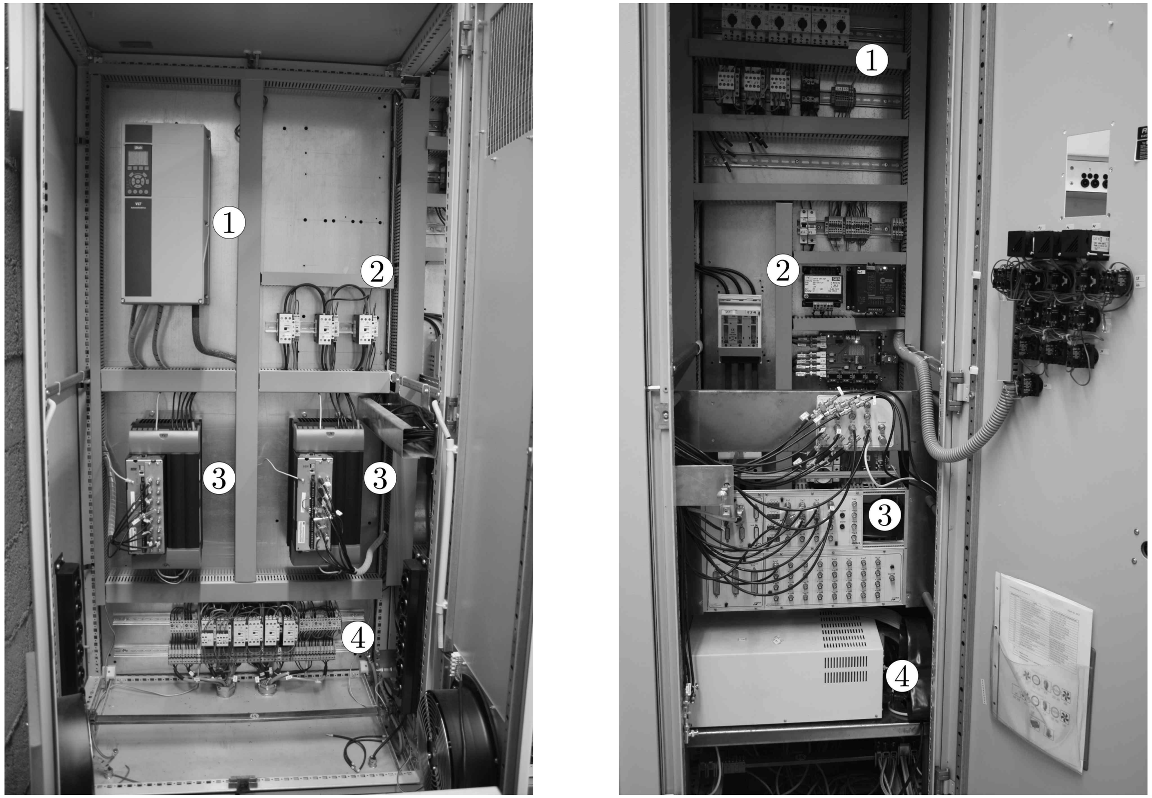

(a) Interconnection between the load inverter ① and the two three leg inverters ③ through a DC-link ②. The converters are connectable to the machines with switches ④.

(b) Fuses for over-current protection ①, auxiliary voltage sources ②, and BNC connector panel ③ of the real-time system ④.

Figure A.2: Control cabinet for Inverter and real-time systems.

List of Publications

[32] Paulo S. Dainez, Daniel Glose, and Edson Bim. “A Decomposition Technique for Asymmetrical Double-star Machines Applying the Three Orthogonal Base System Approach”. In: *Proceedings of the PCIM South America Conference* (2014), pp. 92–98.

[40] D. Glose and R. Kennel. “Carrier-Based Pulse Width Modulation for Symmetrical Six-Phase Drives”. In: *IEEE Transactions on Power Electronics* 30.12 (Dec. 2015), pp. 6873–6882.

[41] D. Glose and R. Kennel. “Continuous Space Vector Modulation for Symmetrical Six-Phase Drives”. In: *IEEE Transactions on Power Electronics* 31.5 (May 2016), pp. 3837–3848. ISSN: 0885-8993.

[42] Daniel Glose, Lukas Leitner, and Ralph Kennel. “Interleaved Switching of Symmetrical Six-Phase Drives”. In: *Proceedings of the PCIM Europe Conference* (May 2014), pp. 1–9.

Bibliography

[1] UBA - Umweltbundesamt. *Energieverbrauch nach Energieträgern und Sektoren in 2013*. `http://www.umweltbundesamt.de/daten/energiebereitstellung-verbrauch/energieverbrauch-nach-energietraegern-sektoren` [last accessed on 09.10.2015].

[2] L. Abraham and R. Blümel. "Optimization of three phase pulse pattern by variable zero sequence component". In: *EPE Conference Proceedings* (1991), pp. 272–277.

[3] H. Abu-Rub et al. "Medium-Voltage Multilevel Converters - State of the Art, Challenges, and Requirements in Industrial Applications". In: *IEEE Transactions on Industrial Electronics* 57.8 (Aug. 2010), pp. 2581–2596.

[4] Philip L. Alger, E. H. Freiburghouse, and D. D. Chase. "Double Windings for Turbine Alternators". In: *American Institute of Electrical Engineers, Transactions of the* 49.1 (Jan. 1930), pp. 226–244.

[5] AGEE-Stat Arbeitsgruppe Erneuerbare Energien-Statistik. *Zeitreihen zur Entwicklung der erneuerbaren Energien in Deutschland*. `http://www.erneuerbare-energien.de/EE/Navigation/DE/Service/Erneuerbare\_Energien\_in\_Zahlen/Zeitreihen/zeitreihen.html` [Last accessed on 09.10.2015].

[6] Robert W. Bacon et al. "Growth and CO2 Emissions: How do Different Countries Fare?" In: *The World Bank* (2007).

[7] Federico Barrero et al. "One-Step Modulation Predictive Current Control Method for the Asymmetrical Dual Three-Phase Induction Machine". In: *IEEE Transactions on Industrial Electronics* 56 (June 2009), pp. 1974–1983.

[8] J.P.A. Bastos and N. Sadowski. *Electromagnetic Modeling by Finite Element Methods*. Electrical and Computer Engineering. CRC Press, 2003.

[9] Thomas Bauernhansl. *Energieeffizienz in Deutschland - eine Metastudie.* Springer Vieweg, 2014.

[10] W. R. Bennett. “New Results in the Calculation of Modulation Products”. In: *Bell System Technical Journal* 12 (1933), pp. 228–243.

[11] N. Bianchi, S. Bolognani, and M. Zigliotto. “Analysis of PM synchronous motor drive failures during flux weakening operation”. In: *27th Annual IEEE Power Electronics Specialists Conference. PESC ’96 Record.* Vol. 2. June 1996, pp. 1542–1548.

[12] H.W. Bode. *Network Analysis and Feedback Amplifier Design.* The Bell Telephone Laboratory series 14. Van Nostrand Reinhold, 1964.

[13] A. Boglietti and E. Carpaneto. “Induction motor high frequency model”. In: *Industry Applications Conference. Thirty-Fourth IAS Annual Meeting.* Vol. 3. 1999, pp. 1551–1558.

[14] R. Bojoi et al. “Complete analysis and comparative study of digital modulation techniques for dual three-phase AC motor drives”. In: *IEEE 33rd Annual Power Electronics Specialists Conference.* Vol. 2. 2002, pp. 851–857.

[15] T. Boller and R.M. Kennel. “Virtual machine - A hardware in the loop test for drive inverters”. In: *13th European Conference on Power Electronics and Applications, 2009. EPE ’09.* Sept. 2009, pp. 1–5.

[16] T. Boller, R.M. Kennel, and J. Holtz. “Increased power capability of standard drive inverters by sequential switching”. In: *IEEE International Conference on Industrial Technology (ICIT).* Mar. 2010, pp. 769–774.

[17] S. Bowes and B.M. Bird. “Novel Approach to the Analysis and Synthesis of Modulation Processes in Power Converters”. In: *IEE Proceedings* 122.5 (May 1975), pp. 507–513.

[18] S.R. Bowes. “Regular-sampled harmonic elimination/minimisation PWM techniques”. In: *Fifth Annual Applied Power Electronics Conference and Exposition. APEC ’90.* Mar. 1990, pp. 532–540.

[19] E. Oran Brigham. *The fast fourier transform: An introduction to Its theory and application.* Prentice Hall, 1973.

[20] T. Bruckner and D.G. Holmes. “Optimal pulse-width modulation for three-level inverters”. In: *IEEE Transactions on Power Electronics* 20.1 (Jan. 2005), pp. 82–89.

[21] Brundtland. *Our Common Future.* World Comission on Environment and Development, 1987.

[22] Giuseppe S. Buja and Giovanni B Indri. "Optimal Pulsewidth Modulation for Feeding AC Motors". In: *IEEE Transactions on Industry Applications* IA-13.1 (Jan. 1977), pp. 38–44.

[23] BMWi Bundesministerium für Wirtschaft und Energie. *Energy Efficiency - Made in Germany.* Brochure. Mar. 2010.

[24] BMWi Bundesministerium für Wirtschaft und Energie. *Zahlen und Fakten - Energiedaten.* `http://www.bmwi.de/DE/Themen/Energie/Energiedaten-und-analysen/energiedaten.html` [Last accessed on 09.10.2015].

[25] A. Busse and J.Holtz. "A digital space vector modulator for the control of a three-phase power converter". In: *VDE-Konferenz Mikroelektronik in der Stromrichtertechnik und bei elektrischen Antrieben, Darmstadt* (1982), pp. 189–195.

[26] K.T. Chau, S.Z. Jiang, and C.C. Chan. "Reduction of current ripple and acoustic noise in dual-inverter pole-changing induction motor drives". In: *IEEE Annual Power Electronics Specialists Conference.* 2000.

[27] Tsung-Po Chen. "Common-Mode Ripple Current Estimator for Parallel Three-Phase Inverters". In: *IEEE Transactions on Power Electronics* 24.5 (May 2009), pp. 1330–1339.

[28] E. Clarke. *Circuit Analysis of A-C Power Systems.* General Electric series. Wiley, 1950.

[29] C. Concordia. "Relations among transformations used in electrical engineering problems". In: *General Electric Rev.* 41 (1938), pp. 323–325.

[30] M.B.R. Correa et al. "Vector and scalar modulation for six-phase voltage source inverters". In: *Power Electronics Specialist Conference, PESC.* Vol. 2. 2003, pp. 562–567.

[31] R.M. Cuzner et al. "Mitigating Circulating Common-Mode Currents Between Parallel Soft-Switched Drive Systems". In: *IEEE Transactions on Industry Applications* 43.5 (Sept. 2007), pp. 1284–1294.

[32] Paulo S. Dainez, Daniel Glose, and Edson Bim. "A Decomposition Technique for Asymmetrical Double-star Machines Applying the Three Orthogonal Base System Approach". In: *Proceedings of the PCIM South America Conference* (2014), pp. 92–98.

[33] Ibrahim Dincer and Marc A. Rosen. *EXERGY: Energy, Environment and Sustainable Development.* Elsevier Science, 2007.

[34] W.C. Duesterhoeft, Max W. Schulz, and Edith Clarke. “Determination of Instantaneous Currents and Voltages by Means of Alpha, Beta, and Zero Components”. In: *Transactions of the American Institute of Electrical Engineers* 70.2 (July 1951), pp. 1248–1255.

[35] D. Dujic, A. Iqbal, and E. Levi. “A Space Vector PWM Technique for Symmetrical Six-Phase Voltage Source Inverters”. In: *EPE Journal* 17.1 (Mar. 2007).

[36] A.C. Ferreira and R.M. Kennel. “Interleaved or sequential switching - for increasing the switching frequency”. In: *7th Internatonal Conference on Power Electronics. ICPE ’07.* Oct. 2007, pp. 738–741.

[37] Tobias Fleiter. “Wirtschaftlicher Vergleich der langfristigen Strom- und Einsparpotenziale von Elektromotorsystemen und Beleuchtungsanlagen in der Industrie”. In: *EnInnov 08, 10. Symposium Energieinnovation. Energiewende: Kurzfassungsband.* 2008.

[38] R. Fotouhi et al. “An efficient method to calculate optimal pulse patterns for medium voltage converters”. In: *Industrial Electronics Society, IECON 2014 - 40th Annual Conference of the IEEE.* Oct. 2014, pp. 1221–1226.

[39] E.F. Fuchs and L.T. Rosenberg. “Analysis of an Alternator with Two Displaced Stator Windings”. In: *IEEE Transactions on Power Apparatus and Systems* PAS-93.6 (Nov. 1974), pp. 1776–1786.

[40] D. Glose and R. Kennel. “Carrier-Based Pulse Width Modulation for Symmetrical Six-Phase Drives”. In: *IEEE Transactions on Power Electronics* 30.12 (Dec. 2015), pp. 6873–6882.

[41] D. Glose and R. Kennel. “Continuous Space Vector Modulation for Symmetrical Six-Phase Drives”. In: *IEEE Transactions on Power Electronics* 31.5 (May 2016), pp. 3837–3848. ISSN: 0885-8993.

[42] Daniel Glose, Lukas Leitner, and Ralph Kennel. “Interleaved Switching of Symmetrical Six-Phase Drives”. In: *Proceedings of the PCIM Europe Conference* (May 2014), pp. 1–9.

[43] I. Gonzalez et al. “Fault-tolerant Operation of Six-phase Energy Conversion Systems with Parallel Machine-side Converters”. In: *IEEE Transactions on Power Electronics* 99 (2015).

[44] K. Gopakumar, V.T. Ranganathan, and S. R. Bhat. “Split phase induction motor operation from PWM voltage source inverter”. In: vol. 1. Sept. 1991, pp. 437–442.

[45] Robert M. Gray. *Toeplitz and Circulant Matrices: A review.* Vol. 2. now Publishers, 2006.

[46] R.M. Green and J.T. Boys. “PWM Sequence Selection and Optimization: A Novel Approach”. In: *IEEE Transactions on Industry Applications* IA-18.2 (Mar. 1982), pp. 146–151.

[47] D. Hadiouche, H. Razik, and A. Rezzoug. “On the design of dual-stator windings for safe VSI fed AC machine drives”. In: *Conference Record of the IEEE Industry Applications Conference.* Vol. 2. 2001, pp. 1123–1130.

[48] Djafar Hadiouche, Lotfi Baghli, and Abderrezak Rezzoug. “Space-vector PWM techniques for dual three-phase AC machine: analysis, performance evaluation, and DSP implementation”. In: *IEEE Industry Applications Society* 42.4 (July 2006), pp. 1112–1122.

[49] P.W. Hammond. “A new approach to enhance power quality for medium voltage AC drives”. In: *IEEE Transactions on Industry Applications* 33.1 (Jan. 1997), pp. 202–208.

[50] T.J. Hammons and D.J. Winning. “Comparisons of synchronous-machine models in the study of the transient behaviour of electrical power systems”. In: *Proceedings of the Institution of Electrical Engineers* 118.10 (Oct. 1971), pp. 1442–1458.

[51] A.M. Hava, R.J. Kerkman, and T.A. Lipo. “Simple analytical and graphical methods for carrier-based PWM-VSI drives”. In: *IEEE Transactions on Power Electronics* 14.1 (1999), pp. 49–61.

[52] D.G. Holmes and T.A. Lipo. *Pulse Width Modulation for Power Converters: Principles and Practice.* IEEE Press Series on Power Engineering. John Wiley & Sons, 2003.

[53] J. Holtz. “Pulsewidth modulation for electronic power conversion”. In: *Proceedings of the IEEE* 82.8 (Aug. 1994), pp. 1194–1214.

[54] J. Holtz and B. Beyer. “Optimal pulsewidth modulation for AC servos and low-cost industrial drives”. In: *IEEE Transactions on Industry Applications* 30.4 (July 1994), pp. 1039–1047.

[55] J. Holtz and N. Oikonomou. “Synchronous Optimal Pulsewidth Modulation and Stator Flux Trajectory Control for Medium-Voltage Drives”. In: *IEEE Transactions on Industry Applications* 43.2 (Mar. 2007), pp. 600–608.

[56] J. Holtz and Xin Qi. “Optimal Control of Medium-Voltage Drives: An Overview”. In: *IEEE Transactions on Industrial Electronics* 60.12 (Dec. 2013), pp. 5472–5481.

[57] J. Holtz and S.Stadtfeld. “A Predictive Controller for the Stator Current Vector of AC Machines Fed from a Switched Voltage Source”. In: *International Power Electronics Conference IPEC* (1983), pp. 1665–1675.

[58] H.S.Black. “Modulation Theory”. In: *Van Nostrand, New York* (1953).

[59] T. Hsiao. “Fault Analysis by Modified Alpha, Beta, and Zero Components-Part I”. In: *Power Apparatus and Systems, Part III. Transactions of the American Institute of Electrical Engineers* 81.3 (Apr. 1962), pp. 136–142.

[60] T. Hsiao. “Fault Analysis by Modified Alpha, Beta, and Zero Components-Part II”. In: *Power Apparatus and Systems, Part III. Transactions of the American Institute of Electrical Engineers* 81.3 (Apr. 1962), pp. 142–146.

[61] Jin Huang et al. “Multiphase machine theory and its applications”. In: *International Conference on Electrical Machines and Systems. ICEMS*. Oct. 2008, pp. 1–7.

[62] G. Hupe and R. Kennel. “Increase of Power and Reduction of Noise and Current Ripple of Inverter Fed Induction Machines”. In: *European Conference on Power Electronics and Applications, EPE* (1989).

[63] G. Hupe et al. “More Power by Multiwinding of Converter Fed Induction Machines”. In: *ICEM’88: International Conference on Electrical Machines*. Sept. 1988.

[64] D.K. Kastha and B.K. Bose. “Investigation of fault modes of voltage-fed inverter system for induction motor drive”. In: *IEEE Transactions on Industry Applications* 30.4 (July 1994), pp. 1028–1038.

[65] Takao Kawabata et al. “New open-winding configurations for high-power inverters”. In: *Proceedings of the IEEE International Symposium on Industrial Electronics, ISIE*. Vol. 2. July 1997, pp. 457–462.

[66] R.M. Kennel et al. “Predictive control in power electronics and drives”. In: *IEEE International Symposium on Industrial Electronics, ISIE*. June 2008, pp. 1–90.

[67] Edward Wilson Kimbark. “Two-Phase Coordinates of a Three-Phase Circuit”. In: *AIEE Technical Paper* 58 (1939), pp. 894–904.

[68] E.A. Klingshirn. “High Phase Order Induction Motors - Part I-Description and Theoretical Considerations”. In: *IEEE Transactions on Power Apparatus and Systems* PAS-102.1 (Jan. 1983), pp. 47–53.

[69] E.A. Klingshirn. “High Phase Order Induction Motors - Part II-Experimental Results”. In: *IEEE Transactions on Power Apparatus and Systems* PAS-102.1 (Jan. 1983), pp. 54–59.

[70] J. W. Kolar, H. Ertl, and F. Zach. “Calculation of the Passive and Active Component Stress of Three-Phase PWM Converter Systems with High Pulse Rate”. In: *Proceedings of the 3rd European Conference on Power Electronics and Applications* 3 (1989), pp. 1303–1311.

[71] J.W. Kolar, H. Ertl, and Franz C. Zach. “Minimizing the current harmonics RMS value of three-phase PWM converter systems by optimal and suboptimal transition between continuous and discontinuous modulation”. In: *Power Electronics Specialists Conference, PESC.* June 1991, pp. 372–381.

[72] T. W. Körner. *Fourier Analysis.* Cambridge University Press, 1989.

[73] D. Krug et al. “Comparison of 2.3-kV Medium-Voltage Multilevel Converters for Industrial Medium-Voltage Drives”. In: *IEEE Transactions on Industrial Electronics* 54.6 (Dec. 2007), pp. 2979–2992.

[74] H. Kubo et al. “Current ripple analysis of PWM methods for open-end winding induction motor”. In: *Energy Conversion Congress and Exposition (ECCE), 2014 IEEE.* Sept. 2014, pp. 3858–3864.

[75] K.S. Kunz and R.J. Luebbers. *The Finite Difference Time Domain Method for Electromagnetics.* Taylor & Francis, 1993.

[76] Jih-Sheng Lai and Fang Zheng Peng. “Multilevel converters-A new breed of power converters”. In: *IEEE Transactions on Industry Applications* 32.3 (May 1996), pp. 509–517.

[77] Lukas Leitner, Daniel Glose, and Ralph Kennel. “Space Vetcor Modulation for Symmetrical Six-Phase Induction Machines”. MA thesis. TU-München, 2013.

[78] E. Levi. “Multiphase Electric Machines for Variable-Speed Applications”. In: *IEEE Transactions on Industrial Electronics* 55.5 (May 2008), pp. 1893–1909.

[79] E. Levi et al. “Multiphase induction motor drives - a technology status review”. In: *Electric Power Applications, IET* 1.4 (July 2007), pp. 489–516.

[80] P. Lezana et al. “Survey on Fault Operation on Multilevel Inverters”. In: *IEEE Transactions on Industrial Electronics* 57.7 (July 2010), pp. 2207–2218.

[81] Shengming Li and L. Xu. “Strategies of fault tolerant operation for three-level PWM inverters”. In: *IEEE Transactions on Power Electronics* 21.4 (July 2006), pp. 933–940.

[82] Shengming Li and Longya Xu. “Fault-tolerant operation of a 150 kW 3-level neutral-point clamped PWM inverter in a flywheel energy storage system”. In: *Conference Record of the 2001 IEEE Industry Applications Conference. Thirty-Sixth IAS Annual Meeting.* Vol. 1. Sept. 2001, pp. 585–588.

[83] T.A. Lipo. “A d-q Model For Six Phase Model Induction Machines”. In: *International Conference on Electrical Machines* (Sept. 1980), pp. 860–867.

[84] T.A. Lipo. “An Improved Weighted Total Harmonic Distortion Index for Induction Motor Drives”. In: *OPTIM, Brasov, Romania,* 2 (2000), pp. 311–322.

[85] T.A. Lipo. “Keynote Speach: Open Winding Variable Speed Electrical Machines - Recent Developments”. In: *ICEMS - Peking* (2011).

[86] P.C. Loh et al. “Reduced common mode carrier-based modulation strategies for cascaded multilevel inverters”. In: *Conference Record of the Industry Applications Conference. 37th IAS Annual Meeting.* Vol. 3. Oct. 2002, pp. 2002–2009.

[87] R. Maheshwari et al. “Analysis and modelling of circulating current in two parallel-connected inverters”. In: *Power Electronics, IET* 8.7 (2015), pp. 1273–1283.

[88] K. Marouani et al. “Study and harmonic analysis of SVPWM techniques for VSI-Fed double-star induction motor drive”. In: *Mediterranean Conference on Control Automation.* June 2007, pp. 1–6.

[89] G. Michler and H.J. Kowalsky. *Lineare Algebra.* De Gruyter Lehrbuch. De Gruyter, 2003.

[90] Takayuki Mizuno et al. “Basic principle and maximum torque characteristics of a six-phase pole change induction motor for electric vehicles”. In: *Electrical Engineering in Japan* 118 (1997), pp. 78–91.

[91] G. Müller and B. Ponick. *Grundlagen elektrischer Maschinen.* Wiley, 2015.

[92] R.H. Nelson and P.C. Krause. “Induction Machine Analysis for Arbitrary Displacement Between Multiple Winding Sets”. In: *IEEE Transactions on Power Apparatus and Systems* PAS-93.3 (May 1974), pp. 841–848.

[93] Hoa Nguyen-Xuan et al. “Efficient Reluctance Network Formulation for Electrical Machine Design Using Optimization”. In: *IEEE Transactions on Magnetics* 50.2 (Feb. 2014), pp. 869–872.

[94] Gun-Tae Park et al. “Control method of NPC inverter for continuous operation under one phase fault condition”. In: *Conference Record of the IEEE Industry Applications Conference. 39th IAS Annual Meeting.* Vol. 4. Oct. 2004, pp. 2188–2193.

[95] L. Parsa. “On advantages of multi-phase machines”. In: *31st Annual Conference of IEEE Industrial Electronics Society.* 2005.

[96] Dr. Martin Pehnt et al. “Potenziale und volkswirtschaftliche Effekte einer ambitionierten Energieeffizienzstrategie für Deutschland”. In: *Wissenschaftliche Begleitforschung zu übergreifenden technischen, ökologischen, ökonomischen und strategischen Aspekten des nationalen Teils der Klimaschutzinitiative* (2009), pp. 1–39.

[97] Stuart D.T. Robertson and Kattingeri M. Hebbar. “A Digital Model for Three-Phase Induction Machines”. In: *IEEE Transactions on Power Apparatus and Systems* PAS-88.11 (Nov. 1969), pp. 1624–1634.

[98] J. Rodriguez, Jih-Sheng Lai, and Fang Zheng Peng. “Multilevel inverters: a survey of topologies, controls, and applications”. In: *IEEE Transactions on Industrial Electronics* 49.4 (2002), pp. 724–738.

[99] M.A. Rosen. “Improving the Efficiency of Electrical Systems via Exergy Methods”. In: *Electrical Power Conference, EPC. IEEE Canada.* Oct. 2007, pp. 467–472.

[100] J. Salmon, J. Ewanchuk, and A. Knight. “PWM Inverters Using Split-Wound Coupled Inductors”. In: *Industry Applications Society Annual Meeting, IAS ’08.* Oct. 2008, pp. 1–8.

[101] G. Satheesh, T.B. Reddy, and C. Sai Babu. “DTC of Open End Winding Induction Motor fed by two space-vector-modulated inverters”. In: *Annual IEEE India Conference (INDICON).* Dec. 2011, pp. 1–6.

[102] D. Schröder. *Elektrische Antriebe - Regelung von Antriebssystemen.* 10. Springer, 2009.

[103] Dierk Schröder. *Elektrische Antriebe - Regelung von Antriebssystemen.* 2nd ed. Springer, 2001.

[104] Dierk Schröder. *Leistungselektronische Schaltungen: Funktion, Auslegung und Anwendung (Springer-Lehrbuch)*. Springer, 2012.

[105] M. Schröter, U. Weißfloch, and D. Buschak. "Energieeffizienz in der Produktion - Wunsch oder Wirklichkeit?" In: *Modernisierung der Produktion* (2009).

[106] Ralf Sesing. "Asynchronmaschinenantrieb mit zwei magnetisch gekoppelten Pulswechselrichtern". PhD thesis. Ruhr-Universität Bochum, 1987.

[107] G.R. Slemon. "Analytical Models for Saturated Synchronous Machines". In: *IEEE Transactions on Power Apparatus and Systems* PAS-90.2 (Mar. 1971), pp. 409–417.

[108] DESTATIS Statistisches Bundesamt. *Bruttoinlandsprodukt ab 1970*. `https://www.destatis.de/DE/ZahlenFakten/GesamtwirtschaftUmwelt/VGR/Inlandsprodukt/Inlandsprodukt.html` [Last accessed on 09.10.2015].

[109] J.K. Steinke, G.J. Dudler, and B.P. Huber. "Field oriented control of a high power GTO-VSI fed AC drive with high dynamic performance using a programmable high speed controller (PHSC)". In: *Conference Record of the Industry Applications Society Annual Meeting*. Vol. 1. Oct. 1992, pp. 393–399.

[110] Gilbert Strang. *Computational Science and Engineering*. Wellesley-Cambridge Press, 2008.

[111] T. Sukegawa et al. "A multiple PWM GTO line-side converter for unity power factor and reduced harmonics". In: *Conference Record of the Industry Applications Society Annual Meeting*. Vol. 1. Sept. 1991, pp. 279–284.

[112] Jian Sun and H. Grotstollen. "Optimized space vector modulation and regular-sampled PWM: a reexamination". In: *Conference Record of the Industry Applications Conference. Thirty-First IAS Annual Meeting, IAS '96*. Vol. 2. Oct. 1996, pp. 956–963.

[113] J. Sykulski. *Computational Magnetics*. Springer Netherlands, 2012.

[114] L.M. Tolbert and T.G. Habetler. "Novel multilevel inverter carrier-based PWM method". In: *IEEE Transactions on Industry Applications* 35.5 (Sept. 1999), pp. 1098–1107.

[115] L.M. Tolbert, Fang Zheng Peng, and T.G. Habetler. "Multilevel converters for large electric drives". In: *IEEE Transactions on Industry Applications* 35.1 (Jan. 1999), pp. 36–44.

[116] B.A. Welchko et al. “Fault tolerant three-phase AC motor drive topologies: a comparison of features, cost, and limitations”. In: *IEEE Transactions on Power Electronics* 19.4 (July 2004), pp. 1108–1116.

[117] D.C. White and H.H. Woodson. *Electromechanical Energy Conversion*. Wiley, 1959.

[118] J. Worotynski. *Calculations of Electromagnetic Field Using the Reluctance Network Method*. University of Sydney, 1996.

[119] Bin Wu. *High-Power Converters and AC Drives*. Wiley-IEEE Press, 2006.

[120] Yifan Zhao and T.A. Lipo. “Space vector PWM control of dual three-phase induction machine using vector space decomposition”. In: *IEEE Industry Applications Society* 31.5 (1995), pp. 110–1109.

[121] B. Zhu et al. “Comparative study of PWM strategies for three-phase open-end winding induction motor drives”. In: *Power Electronics Conference (IPEC-Hiroshima 2014 - ECCE-ASIA), 2014 International*. May 2014, pp. 395–402.